REINDEER

D4.3

Assessment of signalling schemes, protocols, and algorithms for energy-neutral devices

Project number:	101013425
Project acronym:	**REINDEER**
Project title:	REsilient INteractive applications through hyper Diversity in Energy Efficient RadioWeaves technology
Project Start Date:	1st January, 2021
Duration:	48 months
Programme:	H2020-ICT-52-2020
Deliverable Type:	Report
Reference Number:	ICT-52-2020 / D4.3 / 1.00
Workpackage:	WP 4
Due Date:	31st March, 2024
Actual Submission Date:	2nd April, 2024
Responsible Organisation:	LiU, TU GRAZ
Editor:	Ahmet Kaplan
Dissemination Level:	PU
Revision:	1.00
Abstract:	Assessment of signalling schemes, protocols, and algorithms for energy-neutral devices. Quantitative assessment of wireless power transfer, high-rate communications, and accurate positioning with energy neutral devices, based on the designs described in D4.2.
Keywords:	RF, WPT, array near field, energy neutral devices, algorithms

The REINDEER project has received funding from the European Union's Horizon 2020 research and innovation programme under grant agreement No 101013425.

Editor

Ahmet Kaplan (LiU)

Contributors (ordered according to beneficiary numbers)

Ahmet Kaplan, Erik G. Larsson (LIU)

Benjamin J. B. Deutschmann, Maximilian Graber, Lukas D'Angelo, Thomas Wilding, Klaus Witrisal (TU GRAZ)

Ulrich Mühlmann (NXP)

Internal reviewers

Lieven De Strycker (KU Leuven), William Tärneberg (Lund)

Disclaimer

Executive Summary

This deliverable advances the RadioWeaves infrastructure for enabling ultra-reliable communication, positioning, and efficient wireless power transfer (WPT). Combined with energy neutral (EN) devices, this technology enables massive yet sustainable deployments of connected passive devices for the Internet of Things (IoT). Our main contributions to improve the WPT efficiency and the communication quality of EN devices are as follows: the fusion of reciprocity-based and geometry-based beamforming for WPT, the amplitude modeling of specular multipath components (SMCs), the estimation of the EN device position and the use of geometric channel information, the direct link interference (DLI) cancelation algorithm, the detection algorithm for energy neutral device (END) information bits and the hardware design for energy harvesting. The details of the contributions are given below.

For WPT applications, we address challenges related to continuous and reliable channel state information (CSI) updates by focusing on signal processing techniques for beamforming and exploring the relation between a massive multiple-input multiple-output (MIMO) array and its environment. To enhance energy efficiency in WPT, we propose a novel approach leveraging both reciprocity-based and geometry-based beamforming. We employ a sparse Bayesian learning (SBL) algorithm to estimate the EN device position and the geometric channel information based on noisy uplink pilots. A state-space filter is used to improve the position estimates and geometry-based channel predictions. We show that reliability and efficiency in WPT are enhanced, which is crucial for operating EN devices.

By analyzing the measurements obtained from a MIMO testbed inside a laboratory room, we build an abstract model of the channel components and their relationship to the geometry of the indoor surroundings. For this, we develop a compression technique to reduce the amount of data needed to be stored in the environment model. In the context of WPT, we analyze the effectiveness of the model.

In addition, we propose a beamforming technique and a detection algorithm for interference mitigation in backscatter communication (BC) in MIMO setup. Due to the strong DLI, the BC performance degrades, and there is a need for high-resolution analog-to-digital converters (ADCs) in the receiver circuitry, which increases the cost. We propose a transmission scheme that employs the transmit beamforming to cancel the DLI and reduce receiver dynamic range requirements. Additionally, a detection algorithm based on generalized log-likelihood ratio test (GLRT) is introduced to enhance the symbol detection performance at the receiver. Moreover, in a single-input single-output (SISO) setup, for BC in wideband bistatic orthogonal frequency-division multiplexing (OFDM) systems, we propose an algorithm for simultaneous DLI mitigation and CSI estimation. The derived algorithm is also capable of estimating the EN device information bits.

We propose a hardware design for energy harvesting systems, focusing on energy conversion efficiency, the harvesting performance evaluation of the NXP sSUF Test-integrated circuit (IC), the estimation of maximum achievable harvesting distances, and the regulatory compliance in the 2.4 GHz WIFI ISM-band. We show that the power harvesting efficiency of the front end diminishes at higher input powers, creating a challenge for simultaneous operation at both device sensitivity and maximum power budget. To address this challenge, we propose a front-end design with two branches. The first operates at low sensitivities with high conversion efficiency to provide initial access energy. In contrast, the second operates at high voltages to deliver power levels suitable for efficiently driving microcontroller units (MCUs).

In summary, we achieve robustness in WPT by introducing the fusion of reciprocity-based and geometry-based beamforming. We demonstrate that environment-awareness can increase the beamforming efficiency. In the context of WPT, we use the predicted amplitudes of SMCs for maximum ratio transmission (MRT) and show the usefulness of an environment model. We also demonstrate that the DLI in the MIMO BC setup is canceled by the introduction of the transmit beamforming, which in turn enables the use of low-resolution ADCs that are low-cost and energy-efficient. Moreover, we demonstrate that the proposed algorithm for the SISO BC setup estimates the unknown parameters of the backscatter modulation signal, which includes inherent DLI cancellation. In addition, we show that our proposed front-end design with two branches presents a promising solution for better power harvesting efficiency at higher input powers.

Contents

List of Acronyms

3D three-dimensional. 13

ADC analog-to-digital converter. II, 2

AmBC ambient BC. 36

ARFH auxiliary RF harvester. 64

AWGN additive white Gaussian noise. 12

BC backscatter communication. II, 35

BiBC bistatic BC. X, 2

BLUE best linear unbiased estimator. 21

CE carrier emitter. 35

CIR channel impulse response. X, 1

CSI channel state information. II, IX, 1

CSP contact service point. IV, 3

CT cosine transform. 28

CW continuous wave. 61

DA data association. 5

DC direct current. 52

DFT discrete Fourier transform. 28

DL downlink. 53

DMC diffuse multipath component. 21

D-MIMO distributed multiple-input multiple-output (MIMO). 5

DLI direct link interference. II, 2

DTFT discrete-time Fourier transform. 21

DUT device under test. 60

EIRP equivalent isotropically radiated power. 59

EN energy neutral. II, IX, 1

END energy neutral device. II, X, 2

EPC electronic product code. 52

ESD electrostatic discharge. 64

FIR finite impulse response. 2

FT Fourier transform. 21

GLRT generalized log-likelihood ratio test. II, 2

i.i.d. independent and identically distributed. 38

IC integrated circuit. 59

IoT Internet of Things. II, 1

ISM industrial, scientific and medical. 59

kNN k-Nearest-Neighbors. 27

LoS line-of-sight. VII, IX, 1

LS least-squares. 40

MCU microcontroller unit. II, 2

MIMO multiple-input multiple-output. II, VI, 1

ML maximum likelihood. 2

MMSE minimum mean square error. 13

MoBC monostatic BC. 36

MPC multipath component. 2

MPPT maximum power point tracker. 60

MRFH main RF harvester. 64

MRT maximum ratio transmission. III, IX, 3

NLoS non LoS. IX, 1

OFDM orthogonal frequency-division multiplexing. II, 2

OOK on–off keying. 2

P1 Phase 1. 37

P2 Phase 2. 37

PAPR peak-to-average power ratio. 52

PCE power conversion efficiency. 60

PDF probability density function. 5

PF particle filter. 6

PG path gain. IX, 14

PWM pulse-width modulation. 53

RF radio frequency. 35

RFID radio frequency identification. 52

RW RadioWeave. IX, 4

SBL sparse Bayesian learning. II, 5

SI self interference. 36

SIMO single-input multiple-output. 58

SINR signal-to-interference-plus-noise ratio. 35

SIR signal-to-interference ratio. 57

SISO single-input single-output. II, X, 2

SMC specular multipath component. II, 1

SNR signal-to-noise ratio. 1

SVD singular value decomposition. 40

TDD time division multiplexing. 36

UL uplink. 53

URA uniform rectangular array. 7

UV unmanned vehicle. 5

UWB ultra-wideband. 29

VA virtual agent. 29

VNA vector network analyzer. 7

w.r.t. with respect to. 43

WPT wireless power transfer. II, 1

List of Figures

List of Tables

Chapter 1

Introduction

The RadioWeaves infrastructure offers various services, including reliable communication, accurate positioning, and wireless power transfer (WPT). When combined with energy neutral (EN) devices, this infrastructure can enable large-scale and sustainable deployments of connected devices for the Internet of Things (IoT). By directing radio waves coherently from multiple RadioWeave panels to the location of an EN device, exceptional efficiencies can be achieved. We leverage the RadioWeaves infrastructure to make extensive, sustainable, and cost-effective IoT deployments a reality by addressing critical technological challenges, such as robust beamforming techniques, efficient channel modeling, implementing interference mitigation strategies, and designing hardware for energy harvesting systems.

Improving the efficiency of WPT is crucial for supporting the operation of a vast number of passive devices. We investigate novel techniques for beamforming to improve the WPT efficiency. Chapter 2 explains how a RadioWeaves infrastructure enables functional features such as efficiency, mobility support, robustness, and reliability in downlink beamforming through methods such as positioning, environment mapping, and environment learning. The chapter is divided into two sections, each of which evaluates the proposed methods on an individual synthetic aperture measurement dataset. In Section 2.1, we conceptualize an algorithm that localizes an EN device based on noisy uplink pilots and performs environment learning by decomposing the channel impulse response (CIR) into a line-of-sight (LoS) component and several specular multipath components (SMCs). Our first dataset reflects a scenario where the device moves from LoS conditions into non LoS (NLoS) conditions where beamforming via SMCs lets still establish efficient WPT even when the LoS is blocked. Proactive tracking of the device and its SMCs allows to *predict* channel state information (CSI) using a geometry-based channel model. We propose *channel fusion* as a method to combine measured CSI and predicted CSI by incorporating the uncertainty of the individual CSI available. We demonstrate that channel fusion can achieve *efficiency* in low-signal-to-noise ratio (SNR) scenarios where a geometry-based beamformer may outperform a reciprocity-based beamformer, and we show how *robustness* is achieved by relying on measured CSI if the geometry-based channel model breaks down.

Environmental awareness, e.g., amplitude modeling of SMCs, can improve the efficiency of beamforming and WPT. In Section 2.2, we analyze another dataset of channel measurements obtained from a synthetic massive multiple-input multiple-output (MIMO) array interacting with its surroundings. Within this context, an amplitude model is constructed based on the assumed known geometric layout of the indoor environment. We conduct both static and trajectory measurements to capture the dynamic interaction between the synthetic massive MIMO system and

its surrounding environment. Utilizing ray tracing techniques, we extract wall intersection amplitudes from the channel measurements. This process provides insights into the behavior of obstructions and how different building materials affect multipath components (MPCs). To model the environment effectively, we develop compression techniques specifically tailored for wall segments and their associated amplitudes. After compression, we showcase the reconstruction process and demonstrate its applicability to WPT scenarios. This not only underscores the effectiveness of our compression techniques but also highlights the practical implications for WPT applications. To gauge the applicability of the developed methods, we evaluate their prediction capabilities in different ways. Section 2 thus deals with understanding how the radio channel is affected for different surroundings and how it can be modeled efficiently for use in other algorithms.

Distributed RadioWeaves setup is a promising solution for bistatic BC (BiBC). In BiBC, the direct link interference (DLI) between two RadioWeaves (caused by the received carrier signal) is too strong compared to the received backscattered signal due to the double path-loss effect on the backscattered link. This increases the required dynamic range in the receiver circuitry, and consequently, there is a need for high-resolution analog-to-digital converters (ADCs) in the receiver. This represents a great limitation because ADCs are major power consumers. In Chapter 3, we propose a transmission scheme that uses transmit beamforming to cancel the DLI and thereby decreases the necessary dynamic range (and power consumption of the infrastructure). We also propose a generalized log-likelihood ratio test (GLRT) to detect the EN device symbol in the receiver and show that joint use of the proposed beamforming technique and GLRT increases the detection performance of the EN device symbols.

In Chapter 4, we focus on simultaneous DLI mitigation and CSI estimation in single-path single-input single-output (SISO) orthogonal frequency-division multiplexing (OFDM) systems. We establish a time-domain signal model to derive an algorithm to separate the weak backscatter signal from the strong DLI by exploiting the masking property of the binary on–off keying (OOK) modulation of the energy neutral device (END). First, we derive an estimator for the unknown parameters of the OOK modulation signal, which incorporates inherent cancellation of the direct link signal. With the obtained estimate of the modulation parameters, the finite impulse responses (FIRs) of the system are estimated using a masked maximum likelihood (ML) approach. The algorithms are evaluated using a scenario specific bistatic SISO setup based on a standardized OFDM framework and a standardized backscatter scheme.

High input powers can degrade power harvesting efficiency, limiting the simultaneous operation of initial access and efficient energy harvesting at high input powers. To mitigate this challenge, in Chapter 5, we study hardware design aspects of energy harvesting systems, focusing on energy conversion efficiency, maximum reachable harvesting distance, and regulatory considerations within the 2.4 GHz WIFI ISM-band for different use cases. We propose a novel front-end design with dual branches: one optimized for low sensitivities with high conversion efficiency to provide initial access energy, and another operating at high voltages to deliver power levels up to 100 mW for driving microcontroller unit (MCU) efficiently.

Chapter 2

Signal processing for beamforming, channel estimation and positioning

We investigate techniques for beamforming in the application context of WPT. Particularly, we introduce beamforming concepts on the downlink by means of precoding weights for phased arrays. We do this while keeping in mind that the radio channels are reciprocal[1] and the precoding techniques also apply to the uplink. This Chapter is intended for readers with a background in wireless communications.

Notation. For the remainder of this deliverable, lowercase bold letters $\boldsymbol{x}$ will be used to denote vectors, while uppercase bold letters $\boldsymbol{X}$ denote matrices. Further, $[\boldsymbol{x}]_i$ denotes the i^{th} element of vector $\boldsymbol{x}$, and $[\boldsymbol{X}]_{i,j}$ denotes the element of row i and column j in matrix $\boldsymbol{X}$. We use $\boldsymbol{x}^{\mathsf{T}}$ and $\boldsymbol{x}^{\mathsf{H}}$ to denote the transpose and Hermitian transpose of $\boldsymbol{x}$, respectively. The p-norm of vector $\boldsymbol{x}$ is denoted as $\|\boldsymbol{x}\|_p$, while we omit the subscript notation for the Euclidean norm, i.e., $\|\boldsymbol{x}\|$ given $p = 2$. The amplitude of a complex number z is denoted by $|z|$, z^* is the complex conjugate of z, and $\angle z$ is its phase. The Hadamarad product is denoted by $\odot$ and the Kronecker product is denoted by $\otimes$. The identity matrix is denoted by $\boldsymbol{I}$, while $\mathbf{1}_{i\times j}$ denotes a $(i \times j)$-matrix of all ones. With $\boldsymbol{X}$ being an $(M \times N)$ matrix, $\boldsymbol{X}^+$ denotes its $(N \times M)$ Moore-Penrose pseudoinverse.

2.1 Fusion of reciprocity and geometry-based beamforming

We leverage the synergies of both i) *reciprocity-based* and ii) *geometry-based* beamforming by fusing both types of CSI. We have found that the former beamformer inherently exploits spherical wavefront propagation and multipath propagation to increase its efficiency [1] and converges to the power-optimal[2] solution, if *noise-free*, perfect CSI is available. The latter beamformer uses a geometry-based channel model that *predicts* CSI based on a known geometry which is generally not impaired by noise of *measured* CSI in contrast to the former. An EN device position will practically be estimated based on inherently noisy measured CSI, which again introduces uncertainty about the position estimate. So the question arises whether there is much to gain by employing a geometry-based beamformer and if the gains are worth the additional investment of computational resources and power to infer the device position and predict CSI.

[1] In our analysis we consider radio channels between the antennas of a contact service point (CSP) and an EN device. Possibly non-reciprocal parts of their frontends are not considered in this analysis.

[2] This is inherent to performing maximum ratio transmission (MRT) with perfect CSI. Please refer to [1] for more details.

We formulate our central **hypotheses** with respect to functional features:

1. **Efficiency**:
   Fusing noisy[3] *measured* CSI with geometry-based *predicted* CSI will improve the beamforming efficiency. This is because a geometry-based beamformer is likely to reject physically implausible solutions. This results in high energy efficiency in a WPT context and high data-rates in a communication context.

2. **Mobility Support**:
   Leveraging the outstanding positioning capabilities of a distributed radio infrastructure with a state-space filter allows robust and accurate tracking of a device. Paired with a physics-based geometric channel model this allows to *continuously* predict CSI of a fast-moving device even if its pilot rate is insufficient to provide CSI updates for a reciprocity-based beamformer.

3. **Robustness**:
   Predicting sudden changes of CSI (like NLoS conditions) in a known environment, or bypassing impairments can enable ultra-high robustness, i.e., avoiding outage with high probability. This can be achieved either with a single RadioWeave establishing a simultaneous multibeam transmission (via SMCs), or with distributed RadioWeaves jointly beamforming to a single device.

4. **Reliability**:
   Pro-actively tracking and distributing motion information (e.g., position, velocity) supports orchestrating successful handovers of devices from some RadioWeaves with successively unfavorable propagation characteristics (e.g., path loss, blockage, multipath impairements) to others with increasingly favorable chararacteristics. High reliability will be achieved in terms of both low packet loss and low service outage.

Significance for operating **passive EN devices**:
RadioWeaves are a distributed radio infrastructure that natively supports EN devices. Some[4] EN devices are *passive*, i.e., they rely entirely on being powered through WPT and can only communicate through *backscatter* communication. Their operation demands that the *initial-access*, i.e., the first power-up and backscatter communication, has been established successfully such that CSI could be estimated on a backscattered signal. Both their communication ability, as well as their power supply depend heavily on continuous and reliable CSI updates. Rapid changes in channel characteristics may result in an outage, the EN device receiving insufficient power and eventually becoming inoperable. Since a retransmission is impossible[5] for such a passive device, the connectivity is lost and the initial access has to be established again. This highly unfavorable event may be caused by either a mobile EN device, possibly moving out of a focal point or behind a blocking object, or a changing environment, such as a person walking through the LoS path. Especially for mobile EN devices, a geometry-based beamformer can provide the necessary *robustness* when paired with wireless positioning and tracking, possibly at the expense of some efficiency[6].

[3] If and how large the practical efficiency gains are, depends on the SNR, since, in the high-SNR case, a reciprocity-based beamformer is likely to outperform a geometry-based beamformer already.

[4] According to the definition in [2] the device classes 1-2 are entirely passive devices that rely on being powered through WPT and communicating via backscatter communication.

[5] Once in an outage condition, insufficient power is transmitted to the EN device, such that the backscattered signal level is too low to be detected at the receiving RadioWeaves (RWs).

[6] Our results in Fig. 2.3 on page 15 show that a geometry-based beamformer can only outperform a reciprocity-

Our **method** can be outlined as follows:
Inverse Problem. As indicated in the formulation of our hypotheses above, we aim to leverage the positioning capabilities of RadioWeaves, thereby using them as a cognitive radio infrastructure. Per RW, we employ a sparse Bayesian learning (SBL) algorithm from [3] to decompose a measured sum-channel into a LoS and several SMCs using a geometry-based channel model. Hence, we estimate the parameters of the model which explicitly include the position of the EN device and implicitly[7] the positions and orientations of specular surfaces (such as walls and the floor). Although the SBL algorithm is a point estimator, we assign probability density functions (PDFs) to its parameters, which allows us to fuse *local* measurements from multiple RWs on a *global* infrastructure-level. This can be considered an instance of multisensor data fusion, a key enabler for leveraging the full positioning potential with distributed MIMO (D-MIMO) systems. Estimating parameters per RW, we benefit from the following:

i) Working with batches of lower-dimensional data leaves the SBL algorithm *tractable* since it is not well suited for working with high-dimensional data due to the high computational burden involved.

ii) We inherently incorporate estimating the *visibility* of components, which addresses the spatial non-stationarity aspect of D-MIMO infrastructures, but demands to solve the data association (DA) between the individual components detected by individual RWs. That is, some components are detected only at some RWs where they are visible but the detections have to be associated to the same component for jointly processing the information they contain.

iii) SBL is an algorithm that inherently estimates the *model order*, i.e., the number of components the channel measurement is composed of.

Generating estimates with individual RWs instead of jointly estimating parameters with the complete RWs infrastructure would generally sacrifice aperture and hence positioning accuracy. This would be considered the major drawback of this approach. However, we estimate and preserve the phases of the individual RWs which lets us *coherently* fuse estimates on an infrastructure level and, hence, retain the positioning accuracy of using the complete infrastructure aperture. Despite making DA necessary, our method inherently addresses the problem of *spatial nonstationarity*, i.e., components being visible only at a subset of the RWs. While we employ a plane wave (far field) approximation per RW (where the aperture of the RWs is small compared to the curvature of the wavefront), we use a spherical wave (near field) model for the infrastructure. This is how we solve the inverse problem of estimating model parameters from measured CSI.

Forward Problem. We employ a state-space filter i) to get more accurate position estimates at time step n by fusing it with estimates from all preceding time steps $1 : n - 1$, and ii) to predict future positions (e.g., at time steps $n + 1$ or even any non-integer time step). Predicting the position, we can in turn use it as a parameter in our geometry-based channel model and predict CSI for a future position of the EN device along its trajectory, hence we solve the forward problem of generating data using known (in our case *predicted*) parameters.

The presented method is relevant for several **use cases**:
Relating to the use cases defined in [2, Sec. 2.2.2] our method is of particular relevance for use cases **10** *positioning and tracking of robots and unmanned vehicles (UVs)* and **5** *tracking of goods*

based beamformer given noisy CSI. The fusion of both types of CSI provides robustness at the cost of some efficiency.

[7] The parameters that define specular surfaces are described in Section 2.1.2.1 and depend directly on the positions of "mirror images" of the transmitting device.

and real-time inventory both of which demand high positioning accuracy and high reliability while accommodating high mobility speeds. The latter is of particular interest as it needs to support low-energy positioning possibly enabled through passive EN devices that communicate through backscatter communication and depend on robust, continuous WPT. Both use case **8** *wander detection and patient finding* and **11** *location-based information transfer* do also rely on low-energy positioning where the former demands robust positioning in possibly complex environments.

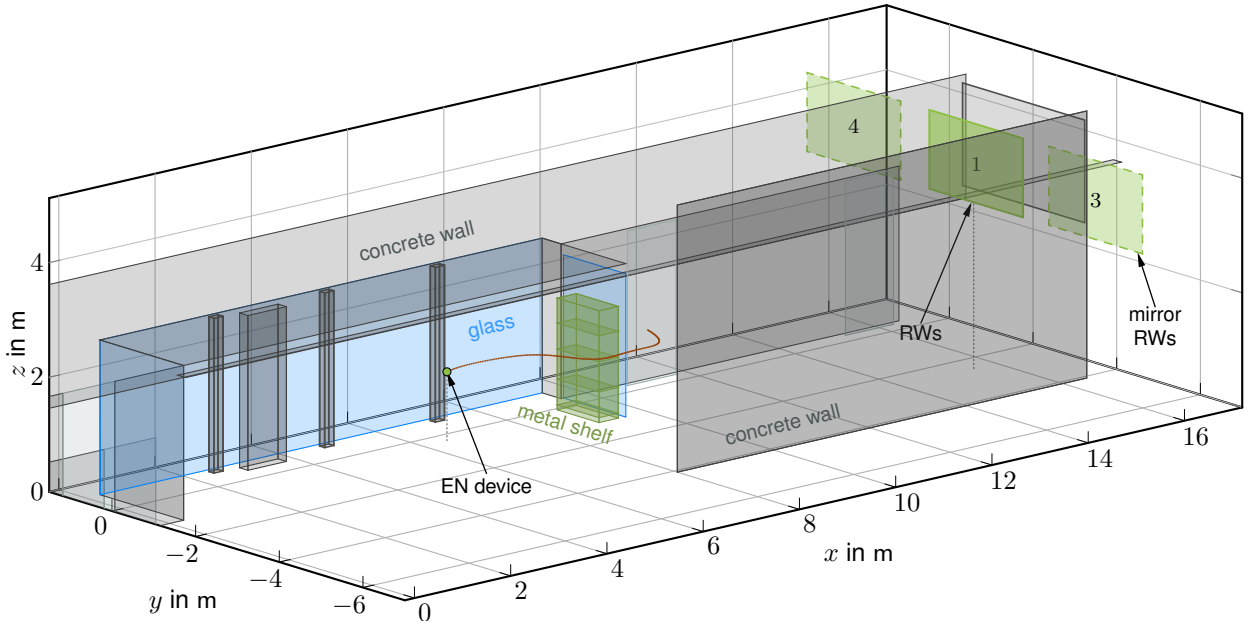

Figure 2.1: The trajectory scenario. An EN device is moving on a trajectory around a shelf from LoS conditions to non LoS conditions.

The remainder of Section 2.1 is organized as follows. In Section 2.1.1, we first introduce the real-life measurement scenario that we use to evaluate our method. We define a signal model in Section 2.1.2 that we believe to correspond most closely with the actual, physical measurements conducted. Later, in Section 2.1.3, we define an inference model that is a (low-complexity) approximation of the physical signal model and is well suited for estimating our parameters of interest. In Section 2.1.3, we briefly discuss how we perform geometry-based channel estimation in *local* per-RW parameters, but the solution to the DA problem between these estimates (for fusing them in *global* per-infrastructure parameters) will be contributed to a future deliverable. Eventually, after having discussed the model of our data for a single snapshot, we make the transition to measurements acquired at time steps n and the state-space filtering of our estimates along the trajectory of the EN device. This estimation and tracking task is implemented using a particle filter (PF) and described in Section 2.1.4. Using the state-space model, the position and velocity estimates at a current time step n are used to predict the device position at arbitrary (possibly non-integer) time steps $n' > n$. Our geometry-based channel model is leveraged in Section 2.1.5 to solve the forward problem of predicting CSI using the predicted device position, after previously being used to solve the inverse problem of estimating the EN device position. Closing the loop, in Section 2.1.7 we fuse our estimated and predicted CSI.

2.1.1 Scenario and dataset description

The scenario considered in this section is depicted in Fig. 2.1. We consider an EN device moving on a trajectory and transmitting uplink pilots. A set of $N_{\text{RW}} = 15$ RWs receives the uplink pilots.

Each RW is equipped with $M = 64$ antennas arranged as an (8×8)-uniform rectangular array (URA) with an antenna spacing of $\Delta = \frac{\lambda}{2}$ with the wavelength $\lambda = \frac{c}{f_c}$ defined at a center frequency $f_c = 6\,\text{GHz}$. Measurements were acquired at a bandwidth B centered around f_c. We consider the RWs to operate *temporally* coherent, i.e., the phase offsets and frequency offsets of their individual clocks are known and compensated for, and *spatially* coherent, i.e., their positions and orientations w.r.t. each other are known. Hence, they can be operated as a single, physically large, and jointly coherent aperture.

We acquired a synthetic aperture measurement dataset with a vector network analyzer (VNA) and a mechanical positioner[8] to evaluate the performance of our method in a real-life scenario. As depicted in Fig. 2.1, the starting position of the EN device along the trajectory is well in LoS conditions w.r.t. the single RWs. Along the trajectory, the EN device moves around a metal shelf and enters NLoS conditions. The shelf is filled with strongly absorbing material to cause severe blockage[9] of the LoS. Hypothesis 3 of our research is that robust algorithms can achieve resilience by exploiting spatial diversity to overcome sudden changes in the propagation channel. In the context of this dataset, the task is to reach the EN device in NLoS conditions by exploiting SMC channels. As depicted in Fig.2.1, we model these channels through an SMC channel model, where reflections at large, planar surfaces are represented through images of the physical RWs mirrored across these surfaces (e.g., walls, windows, or the floor).

We first describe a "generative" *signal model* in Section 2.1.2 that we believe corresponds most accurately to the "true" physical mechanisms generating our measured data. Later, we describe an *inference model* in Section 2.1.3 where we approximate the "true" physical model and trade its accuracy and complexity for computational efficiency and simplicity.

2.1.2 Signal model

Before diving into the details of our "generative" *signal model* it is worth highlighting what position-related *information* is available in our measured signals. In array signal processing, there exist three fundamental array responses:

- (a) The *spatial* array response (cf. Sec. 2.1.3.2) models the phase shifts of a signal at different points in space (sampled through antennas or other sensors) due to different propagation distances, or arrival with different phases, respectively. It is conventionally used to find the direction[10] of a signal incident at an antenna array.
- (b) The *temporal* array response (cf. Sec. 2.1.3.1) models the phase shifts of a signal at different points in the frequency-domain due to the propagation distance the signal traveled from its source to a receiving antenna. It is conventionally used to determine the distance to the signal source.
- (c) The *Doppler* array response models the phase shifts of a signal at different points in time due to the Doppler frequency shift caused by the relative motion (i.e., the velocity) between the signal source and a receiving antenna. It is conventionally used to determine the velocity of the signal source, but can also be used to perform positioning [5].

[8] Refer to [4] for more details on the measurement system.

[9] The shelf has been filled with absorbers intentionally to create an extreme "worst case" scenario.

[10] In the array near-field, the spatial array response (a) can also be used to determine the distance to the signal source without demanding bandwidth resources.

With "only" $N = 199$ measurements along a trajectory spanning multiple meters, the corresponding Doppler-aperture is rather coarse. Hence, in this work, we do not use the Doppler aperture ⓒ and focus on the spatial array response ⓐ and the temporal array response ⓑ for positioning the EN device.

As described in Section 2.1.1, we consider a single-antenna EN device moving on a trajectory and transmitting uplink pilots. The uplink pilots impinge on the N_{RW} RWs, each equipped with M receive antennas. At a single time instance t_n, each RW acquires *noisy* frequency-domain channel vectors

$$\widetilde{\boldsymbol{h}}_m = \sum_{k=1}^{K} \boldsymbol{h}_{m,k} + \boldsymbol{h}_{\text{DM},m} + \boldsymbol{n}_m \quad \in \mathbb{C}^{N_f \times 1} \tag{2.1}$$

per antenna $m \in \{1 \ \dots \ M\}$ in complex baseband with elements $[\widetilde{\boldsymbol{h}}_m]_{n_f}$, $n_f \in \{-\frac{N_f-1}{2} \ \dots \ \frac{N_f-1}{2}\}$ being discrete-frequency samples equally-spaced at $\Delta f = \frac{B}{N_f-1}$ and the number of frequency bins N_f either being an odd integer, or n_f being centered between two integers. Equation (2.1) consists of three terms: The first term represents a sum of an LoS channel vector $\boldsymbol{h}_{m,1}$ and $(K-1)$ SMC channel vectors $\{\boldsymbol{h}_{m,k} \,|\, 2 < k < K\}$ modeling reflections at large, planar surfaces. The second term represents *diffuse multipath* which models stochastic scattering at small, distributed objects, or surfaces that are rough w.r.t. the wavelength λ [6]. The third term represents a noise vector of N_f i.i.d. circular Gaussian noise samples $[\boldsymbol{n}_m]_{n_f} \sim \mathcal{CN}(0, \sigma^2)$.

For inference, we neglect diffuse multipath in this work and focus on the other two terms. We model the *noise-free* SMC channel vector $\boldsymbol{h}_{m,k}$ (including the LoS) using a geometry-based channel model initially defined in [7] and later refined in [1]:

$$[\boldsymbol{h}_{m,k}]_{n_f} = \underbrace{\sqrt{G_{\text{r}}} \frac{\lambda}{\sqrt{4\pi}}}_{\sqrt{A_{\text{r}}}} \sqrt{G_{\text{t}}} \frac{1}{\sqrt{4\pi} d_{k,m}} \gamma_{k,m} \, g^{\text{pol}}_{k,m} \, e^{-j\frac{2\pi}{\lambda_{n_f}} d_{k,m}} \tag{2.2}$$

$$= \sqrt{G_{\text{r}}} \sqrt{G_{\text{t}}} \frac{\lambda}{4\pi d_{k,m}} \gamma_{k,m} \, g^{\text{pol}}_{k,m} \, e^{-j\frac{2\pi}{c}(f_{\text{c}} + \Delta f \, n_f) \, d_{k,m}} \tag{2.3}$$

In this equation, G_{r} and G_{t} denote the angle-dependent antenna gains of the receive and transmit antennas, where A_{r} represents the aperture of a receive antenna. Possible reflection coefficients[11] at specular surfaces and polarization losses are modeled through $\gamma_{k,m} \in \mathbb{C}$ and $g^{\text{pol}}_{k,m} \in [0, 1]$, respectively. The symbol $d_{k,m}$ denotes the scalar distance between the transmit antenna located at position $\boldsymbol{p}$ (notation for brevity; later denoted $\boldsymbol{p}_n$ considering a moving device) and the position $\boldsymbol{p}_{k,m}$ of the m^{th} receiving antenna of the k^{th} SMC, i.e., $d_{k,m} = \|\boldsymbol{r}_{k,m}\|$ with the vectorial distance $\boldsymbol{r}_{k,m} = \boldsymbol{p}_{k,m} - \boldsymbol{p}$. As is indicated in Fig. 2.1, we model first-order[12] SMCs through *virtual* images of the *physical* RWs mirrored across specular surfaces. If the RWs were transmitting, the EN device would receive signals virtually impinging from the location of the mirror sources. With the EN device transmitting, the RWs would receive signals impinging from images of the EN device virtually mirrored across specular surfaces. Due to channel *reciprocity*, both of these models are equivalent regardless of whether an RW acts as a transmitter or receiver. The exponential term in (2.2) models the phase shift of the signal at each *passband*

[11] Reflection coefficients γ are computed through the Fresnel equations and depend on electromagnetic material parameters. Lossy materials (conductivity $\sigma > 0$) may result in complex-valued reflection coefficients, and hence shift the signal in phase.

[12] To save computational complexity and knowing that most power is contained in the LoS and some first-order reflections [1], we focus on these only and leave extending the model for higher-order mirror sources to future work.

frequency $(f_c + \Delta f\, n_f)$ depending on the distance $d_{k,m}$ traveled. Note the dependence on both the frequency-domain bins as well as the spatial-domain positions of the antennas, hence the *spatiotemporal sampling* of the received signal.

2.1.2.1 Geometrical specular multipath model

We consider *physical* RWs $n_s \in \{1 \ \dots \ N_{RW}\}$ centered around $\boldsymbol{p}_{n_s}^{RW}$ with antennas $m \in \{1 \ \dots \ M\}$ located at positions $\boldsymbol{p}_m^a$ *relative* to $\boldsymbol{p}_{n_s}^{RW}$. The complete template RW array *layout* relative to $\boldsymbol{p}_{n_s}^{RW}$ is captured in $\boldsymbol{P}_t = [\boldsymbol{p}_1^a \ \dots \ \boldsymbol{p}_M^a] \in \mathbb{R}^{3\times M}$. The antenna positions of an actual *physical* RW are computed by shifting it out of the origin to its intended position $\boldsymbol{p}_{n_s}^{RW}$ through

$$\boldsymbol{P}_{n_s}^{(1)} = \boldsymbol{P}_t + \boldsymbol{p}_{n_s}^{RW}\, \mathbf{1}_{1\times M}\,, \tag{2.4}$$

where $\mathbf{1}_{i\times j}$ denotes an $(i \times j)$-matrix of all ones.

Our considered geometric model is constrained to first-order SMCs, which allows to sufficiently describe the surfaces[13] with normal vectors $\boldsymbol{n}_k^w$ and one arbitrary point $\boldsymbol{p}_k^w$ on the plane. To mirror an RW across a surface $k > 1$, it is practical to first mirror its physical center position $\boldsymbol{p}_{n_s}^{RW}$

$$\boldsymbol{p}_{n_s,k}^{SMC} = \boldsymbol{p}_{n_s}^{RW} - 2\underbrace{\left(\left(\boldsymbol{p}_{n_s}^{RW} - \boldsymbol{p}_k^w\right)^T \boldsymbol{n}_k^w\right)}_{:=l} \boldsymbol{n}_k^w\,, \tag{2.5}$$

l being the (minimum) scalar distance between physical RW and the surface (see Fig. 2.2), and use the householder matrix

$$\boldsymbol{\mathcal{H}} = \boldsymbol{I} - 2\,\boldsymbol{n}_k^w\,\boldsymbol{n}_k^{wT} \tag{2.6}$$

to compute the array layout of its mirror image

$$\boldsymbol{P}_{n_s}^{(k)} = \boldsymbol{\mathcal{H}}\ \boldsymbol{P}_t + \boldsymbol{p}_{n_s,k}^{SMC}\, \mathbf{1}_{1\times M}\,. \tag{2.7}$$

2.1.3 Inference model

Both for the reverse problem (i.e., inference) as well as the forward problem (i.e., prediction), we focus on the LoS and first-order SMC channel vectors $\boldsymbol{h}_{m,k}^{(n_s)}$ of each RW n_s, since they contain most of the signal power [1].

2.1.3.1 Temporal array response

We define the *temporal array response* vector in complex baseband as

$$\boldsymbol{b}^{(n_s)}(\tau) = \left[e^{-j2\pi\Delta_f \frac{N_f-1}{2}\tau_{n_s}} \ \dots \ e^{j2\pi\Delta_f \frac{N_f-1}{2}\tau_{n_s}}\right] \in \mathbb{C}^{N_f\times 1}\,, \tag{2.8}$$

which describes the phase shifts of the signal in the N_f frequency domain bins depending on the propagation delay τ of a signal from the transmitting EN device to the center of a receiving[14] RW. Hence, we use (2.8) to find the scalar propagation distances $d_k := \|\boldsymbol{r}_{n_s}\|$ with $\boldsymbol{r}_{n_s} = \boldsymbol{p}_{k,m} - \boldsymbol{p}$ denoting the vectorial distance from the EN device at position $\boldsymbol{p}$ to the center of the n_s^{th} RW.

[13] Note that this definition models surfaces of infinite extent which is sufficient only for first-order SMCs and convex scenario/room geometries.

[14] According to our mirror source model defined in Section 2.1.2.1, the signal is received by both physical and virtual mirror RWs.

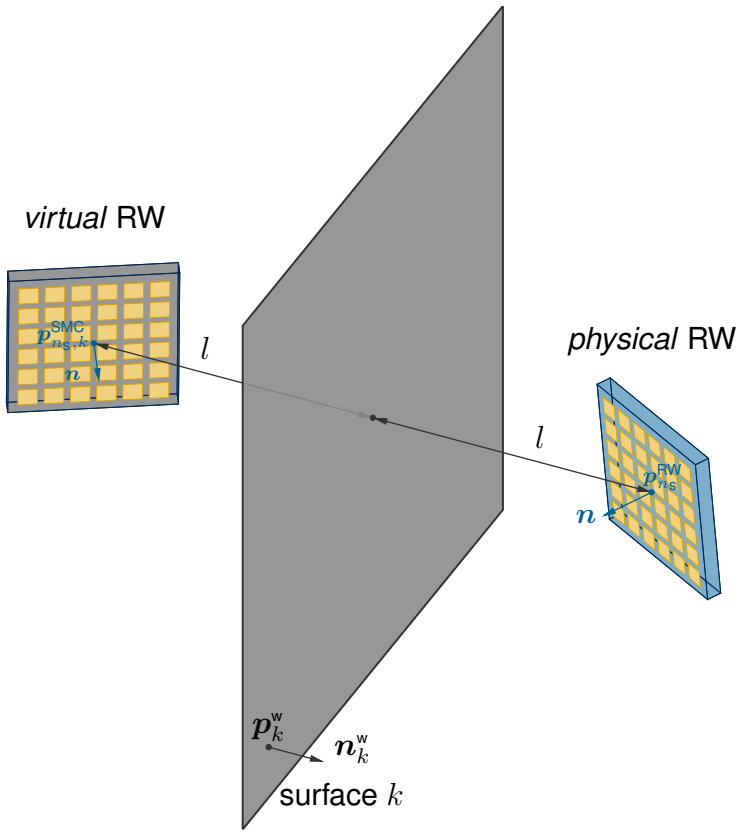

Figure 2.2: Courtesy of the IEEE P3343 Working Group: Illustration of the (virtual) mirror RW model. The antenna layout of the physical aperture is computed using (2.4) while the layout of the virtual aperture is computed using (2.7). Any specular surface k is described through its normal vector $\boldsymbol{n}^{\text{w}}_k$ and an arbitrary point $\boldsymbol{p}^{\text{w}}_k$ on the surface.

2.1.3.2 Spatial array response

In this section, we introduce a general *spatial array response* and decompose it into a *hierarchical* model of *local* array responses $\boldsymbol{a}^{\text{s}}_{n_\text{s}}$ for RWs, and *global* array responses $\boldsymbol{a}^{\text{i}}$ for the complete infrastructure of RWs. The word *local* refers to the fact that we first extract point estimates in local per-RW coordinates using SBL and later fuse these estimates on an infrastructure level in global coordinates.

We define the general spatial array response for a device at position $\boldsymbol{p}$ transmitting an uplink pilot that is received at RWs $n_\text{s} \in \{1 \ \dots \ N_{\text{RW}}\}$ centered around $\boldsymbol{p}^{\text{RW}}_{n_\text{s}}$ with antennas $m \in \{1 \ \dots \ M\}$ located at positions $\boldsymbol{p}^{\text{a}}_m$ *relative* to $\boldsymbol{p}^{\text{RW}}_{n_\text{s}}$:

$$[\boldsymbol{a}]^{(n_\text{s})}_m = \exp\left\{-j\boldsymbol{r}^{\text{T}}_m \boldsymbol{k}^{(n_\text{s})}_m\right\} = \exp\left\{-j\left(\boldsymbol{p} - (\boldsymbol{p}^{\text{a}}_m + \boldsymbol{p}^{\text{RW}}_{n_\text{s}})\right)^{\text{T}} \boldsymbol{k}^{(n_\text{s})}_m\right\} \tag{2.9}$$

where the wave vectors

$$\boldsymbol{k}^{(n_\text{s})}_m = \frac{2\pi}{\lambda}\begin{bmatrix}\sin\theta^{(n_\text{s})}_m \cos\varphi^{(n_\text{s})}_m \\ \sin\theta^{(n_\text{s})}_m \sin\varphi^{(n_\text{s})}_m \\ \cos\theta^{(n_\text{s})}_m\end{bmatrix} \tag{2.10}$$

are defined w.r.t. the phase centers of each individual antenna m within each sub-array n_s in local spherical antenna coordinates with $\theta_m^{(n_\mathsf{s})}$ denoting the elevation angle and $\varphi_m^{(n_\mathsf{s})}$ denoting the azimuth angle. The spatial array response in (2.9) describes the phase shifts of a signal at different points in space (i.e., antenna positions) due to different propagation distances from the the transmitting EN device to the individual antennas m of a receiving RWs.

Assumption A1:

Despite (2.9) generally representing a spherical wavefront model both regarding the *infrastructure* of N_RW RWs as well as the M antennas within an RW, we apply a *plane wave approximation* within an RW. Hence, we replace the wave-vector $\boldsymbol{k}_m^{(n_\mathsf{s})}$ defined w.r.t. the phase center of each antenna m with a wave vector $\boldsymbol{k}_{n_\mathsf{s}}$ defined w.r.t. the phase center of the n_s^{th} sub-array

$$\boldsymbol{k}_{n_\mathsf{s}} = \frac{2\pi}{\lambda} \begin{bmatrix} \sin\theta^{(n_\mathsf{s})} \cos\varphi^{(n_\mathsf{s})} \\ \sin\theta^{(n_\mathsf{s})} \sin\varphi^{(n_\mathsf{s})} \\ \cos\theta^{(n_\mathsf{s})} \end{bmatrix} . \tag{2.11}$$

Hence our array response becomes

$$[\boldsymbol{a}]_m^{(n_\mathsf{s})} = \exp\Big\{ -j \overbrace{(\underbrace{\boldsymbol{p} - \boldsymbol{p}_{n_\mathsf{s}}^{\mathsf{RW}}}_{:=\boldsymbol{r}_{n_\mathsf{s}}})^\mathsf{T} \boldsymbol{k}_m^{(n_\mathsf{s})}}^{:=\phi_{n_\mathsf{s}}} \Big\} \exp\left\{ j \boldsymbol{p}_m^{\mathsf{a}\,\mathsf{T}} \boldsymbol{k}_m^{(n_\mathsf{s})} \right\} \tag{2.12}$$

$$\overset{\text{A1}}{\approx} \underbrace{\exp\left\{ -j (\boldsymbol{p} - \boldsymbol{p}_{n_\mathsf{s}}^{\mathsf{RW}})^\mathsf{T} \boldsymbol{k}_{n_\mathsf{s}} \right\}}_{:=[\boldsymbol{a}^\mathsf{i}]_{n_\mathsf{s}}} \underbrace{\exp\left\{ j \boldsymbol{p}_m^{\mathsf{a}\,\mathsf{T}} \boldsymbol{k}_{n_\mathsf{s}} \right\}}_{:=[\boldsymbol{a}_{n_\mathsf{s}}^\mathsf{s}]_m} , \tag{2.13}$$

where we have now factorized our general array response into a *per sub-array response* $\boldsymbol{a}_{n_\mathsf{s}}^\mathsf{s} \in \mathbb{C}^{M\times 1}$ (subject to the plane wave assumption A1) and a *per infrastructure array response* $\boldsymbol{a}^\mathsf{i} \in \mathbb{C}^{N_\mathsf{RW}\times 1}$ that represents a spherical wavefront model.

2.1.3.3 Likelihood model

The local per-RW parameter vector for an RW n_s for component k is

$$\boldsymbol{\eta}_{\mathsf{RW},n_\mathsf{s}}^{(k)} = \left[\theta_{n_\mathsf{s}}^{(k)}, \varphi_{n_\mathsf{s}}^{(k)}, \tau_{n_\mathsf{s}}^{(k)}, \phi_{n_\mathsf{s}}^{(k)}, \alpha_{n_\mathsf{s}}^{(k)}, \sigma_{n_\mathsf{s}}^2, \widetilde{\gamma}^{(k)}\right]^\mathsf{T} \in \mathbb{R}^{7\times 1} , \tag{2.14}$$

containing elevation and azimuth angles, delay, phase, and amplitude of the k^{th} impinging component and a noise variance at the n_s^{th} RW (which is equal for all impinging components). Note that K_{n_s} components (i.e., the LoS and SMCs) are impinging on RW n_s. SBL, our chosen channel estimator, inherently estimates this model order K_{n_s}. The algorithm demands estimating a parameter $\widetilde{\gamma}^{(k)}$ per component k, which represents the ratio of amplitude variances to the noise variance, i.e., SNRs [3, Footnote 2]. The number of parameters to be estimated per RW is $7\,K_{n_\mathsf{s}} + 1$.

When arranging the noisy channel estimates $\widetilde{\boldsymbol{h}}_m$ of all antennas m of a RW n_s into a matrix $\widetilde{\boldsymbol{H}}_{n_\mathsf{s}} = \left[\widetilde{\boldsymbol{h}}_1 \ \ldots \ \widetilde{\boldsymbol{h}}_M\right] \in \mathbb{C}^{M\times N_f}$ and stacking them into a "measured data" vector $\boldsymbol{y}_{n_\mathsf{s}} := \mathrm{vec}(\widetilde{\boldsymbol{H}}_{n_\mathsf{s}}) \in \mathbb{C}^{MN_f\times 1}$, the likelihood of the data parameterized by the vectors $[\boldsymbol{\eta}_{\mathsf{RW},n_\mathsf{s}}^{(1)} \ \ldots \ \boldsymbol{\eta}_{\mathsf{RW},n_\mathsf{s}}^{(K)}]$ for

all components k is

$$p\left(\boldsymbol{y}_{n_\mathsf{s}}; [\boldsymbol{\eta}^{(1)}_{\mathsf{RW},n_\mathsf{s}} \ \dots \ \boldsymbol{\eta}^{(K)}_{\mathsf{RW},n_\mathsf{s}}]\right) = \frac{1}{\pi^{MN_f}|\boldsymbol{C}_y|} \exp\left\{ -\left(\boldsymbol{y}_{n_\mathsf{s}} - \sum_{k=1}^{K} \alpha^{(k)}_{n_\mathsf{s}} e^{j\phi^{(k)}_{n_\mathsf{s}}} \boldsymbol{a}^{\mathsf{s}}_{n_\mathsf{s}} \otimes \boldsymbol{b}\right)^{\mathsf{H}} \boldsymbol{C}_y^{-1} \left(\boldsymbol{y}_{n_\mathsf{s}} - \sum_{k=1}^{K} \alpha^{(k)}_{n_\mathsf{s}} e^{j\phi^{(k)}_{n_\mathsf{s}}} \boldsymbol{a}^{\mathsf{s}}_{n_\mathsf{s}} \otimes \boldsymbol{b}\right) \right\} \tag{2.15}$$

where $\boldsymbol{C}_y \approx \sigma^2_{n_\mathsf{s}} \boldsymbol{I}$ can be assumed for the covariance matrix in the additive white Gaussian noise (AWGN)-only case for narrow-band MIMO channels [8]. The per-RW spatial array response is captured in $\boldsymbol{a}^{\mathsf{s}}_{n_\mathsf{s}}(\theta^{(k)}_{n_\mathsf{s}}, \varphi^{(k)}_{n_\mathsf{s}},)$, while the temporal array response is captured in $\boldsymbol{b}(\tau^{(k)}_{n_\mathsf{s}})$.

Note that the implementation in [3] models the amplitudes $\alpha^{(k)}_{n_\mathsf{s}}$ through $\widetilde{\gamma}^{(k)}$ and $\sigma^2_{n_\mathsf{s}}$ and hence reduces the actual number of parameters to estimate to $6\,K_{n_\mathsf{s}}$.

2.1.4 Tracking

In the previous sections, we have considered a single snapshot of data (i.e., CSI), and hence our parameters were defined "quasi-static", i.e., independent of the time steps n. For tracking, we make the transition to a dynamic setup, hence many of our parameters become dependent on n. We employ a PF which both inherently computes estimates using the likelihood in (2.15) and performs Bayesian state-space filtering along the trajectory.

The global per-infrastructure parameter vector is

$$\boldsymbol{\eta}_{\mathsf{i},n} = \begin{pmatrix} \boldsymbol{p}_n & \in \mathbb{R}^3 & \dots & \text{physical device position} \\ \boldsymbol{v}_n & \in \mathbb{R}^2 & \dots & \text{device velocity} \\ \overline{\boldsymbol{p}}_n & = [\boldsymbol{p}_n^{(2)\mathsf{T}} \dots \boldsymbol{p}_n^{(K)\mathsf{T}}]^\mathsf{T} \in \mathbb{R}^{2(K-1)} & \dots & \text{mirror device positions} \\ \overline{\boldsymbol{\chi}_n} & = [\boldsymbol{\chi}_n^{(2)\mathsf{T}} \dots \boldsymbol{\chi}_n^{(K)\mathsf{T}}]^\mathsf{T} \in \mathbb{B}^{N_\mathsf{RW}(K-1)} & \dots & \text{component visibility} \\ \boldsymbol{\gamma} & = [\gamma_2 \dots \gamma_K]^\mathsf{T} \in \mathbb{R}^{K-1} & \dots & \text{reflection coefficient vector} \\ \overline{\boldsymbol{\phi}}_n & = [\boldsymbol{\phi}_n^{(1)\mathsf{T}} \dots \boldsymbol{\phi}_n^{(N_\mathsf{RW})\mathsf{T}}]^\mathsf{T} \in \mathbb{R}^{\overline{K}-N_\mathsf{RW}} & \dots & \text{component phase vector} \\ \boldsymbol{s} & = [\sigma_1^2 \dots \sigma^2_{N_\mathsf{RW}}]^\mathsf{T} \in \mathbb{R}^{N_\mathsf{RW}} & \dots & \text{noise variance vector} \end{pmatrix} \tag{2.16}$$

where $\overline{K} = \sum_{n_\mathsf{s}=1}^{N_\mathsf{RW}} K_{n_\mathsf{s}}$. The global parameter vector is divided into

blue dynamic global parameters that are tracked by the PF,

orange quasi-static global parameters that are derived from SBL point estimates, and

green local parameters that are inherently estimated by SBL as point estimates.

We will focus on the dynamic parameters, i.e., the device position $\boldsymbol{p}_n$, the device velocity $\boldsymbol{v}_n$, and the positions of mirror devices $\overline{\boldsymbol{p}}_n$, to formulate the state-space model for our PF and hence perform Bayesian state-space filtering over the steps n. The point estimates of the other parameters (extracted from SBL) will be treated as deterministic knowns in each step n of our tracker.

Our choice of a state-space model is a nearly constant velocity model [9, Section 6.3.2], with a state transition equation

$$\boldsymbol{\eta}^{\mathsf{PF}}_k = \boldsymbol{\Phi}\, \boldsymbol{\eta}^{\mathsf{PF}}_{k-1} + \boldsymbol{\Gamma} \boldsymbol{n}_k\,, \tag{2.17}$$

where $\boldsymbol{\eta}_k^{\mathsf{PF}}$ are the parameters of the current step k that are composed a sum of i) the parameters of the previous step $k-1$ propagated over the state transition matrix $\boldsymbol{\Phi}$ and ii) a circular Gaussian noise $[\boldsymbol{n}]_i \sim \mathcal{CN}(0,1)$ propagated over the noise gain $\boldsymbol{\Gamma}$.

2.1.5 Channel prediction

In the following, we introduce the channel prediction based on the channel model in (2.2). For notational brevity, we formulate channel prediction and fusion results for a single frequency bin n_f in Sections 2.1.5 and 2.1.7, knowing that our method needs to be applied to each frequency $n_f \in \{1 \ \dots \ N_f\}$ to construct a channel vector $\boldsymbol{h}_{m,k} \in \mathbb{C}^{N_f \times 1}$.

In the following, we define a parameter vector $\boldsymbol{\eta}_{\mathsf{p}} := [\boldsymbol{p}_n^{\mathsf{T}}, \boldsymbol{\gamma}^{\mathsf{T}}]^{\mathsf{T}}$ of dimension $\mathcal{D}_{\mathsf{p}} = \dim(\boldsymbol{\eta}_{\mathsf{p}}) = K+2$ holding a subset of our global parameter vector $\boldsymbol{\eta}_{\mathsf{i},n}$ in (2.16) that describes our geometry-based channel model.

We compute narrow-band channel predictions $\widetilde{\boldsymbol{h}} \in \mathbb{C}^{M \times 1}$ using

$$[\widetilde{\boldsymbol{h}}]_m(\boldsymbol{\eta}_{\mathsf{p}}) = \sum_{k=1}^{K} [\widetilde{\boldsymbol{h}}_k]_m = \sum_{k=1}^{K} \sqrt{G_{\mathrm{r}}}\,\sqrt{G_{\mathrm{t}}}\,\frac{\lambda}{4\pi d_{k,m}}\,\gamma_{k,m}\,\chi_{k,m}\,g_{k,m}^{\mathsf{pol}}\,e^{-j\frac{2\pi}{c}(f_{\mathsf{c}}+\Delta f\,n_f)\,d_{k,m}}\,, \tag{2.18}$$

where the parameters G_{r}, G_{t}, and $d_{k,m}$ are functions of the EN device position $\boldsymbol{p}_n$, while $\gamma_{k,m}$ is captured in $\boldsymbol{\gamma}$. The vector $\widetilde{\boldsymbol{h}}_k$ denotes the predicted LoS channel vector if $k = 1$ and predicted SMC channel vectors for $k > 1$. The parameter $\chi_k \in \mathbb{B}$, with $\mathbb{B} := \{0, 1\}$ denoting the binary set, models the visibility of component k.

2.1.6 Channel fusion

Measured CSI. Our channel estimates acquired on a received uplink pilot

$$\hat{\boldsymbol{h}} = \boldsymbol{h} + \boldsymbol{n}_h \quad \in \mathbb{C}^{M \times 1} \tag{2.19}$$

consist of the "true" channel vector $\boldsymbol{h}$ corrupted by i.i.d. additive white circular Gaussian noise $[\boldsymbol{n}_h]_m \sim \mathcal{CN}(0, \sigma_n^2)$. Hence, the uncertainty about our measured CSI is captured in the covariance matrix $\boldsymbol{C}_{\mathsf{m}} \triangleq \sigma_n^2 \boldsymbol{I}$.

Predicted CSI. The uncertainty of our predicted parameters $\hat{\boldsymbol{\eta}}_{\mathsf{p}}^{(k)}$ can be readily extracted from our PF using

$$\hat{\boldsymbol{C}}_{\boldsymbol{\eta}_{\mathsf{p}}}^{(k)} = \sum_{i=1}^{K} w^i\,(\boldsymbol{\eta}^i - \hat{\boldsymbol{\eta}}_{n\mathsf{MMSE}})^2 \quad \in \mathbb{C}^{\mathcal{D}_{\mathsf{p}} \times \mathcal{D}_{\mathsf{p}}} \tag{2.20}$$

$$\approx \int_{-\infty}^{\infty} (\boldsymbol{\eta}_{\mathsf{p}} - \mathbb{E}(\boldsymbol{\eta}_{\mathsf{p}}))\,(\boldsymbol{\eta}_{\mathsf{p}} - \mathbb{E}(\boldsymbol{\eta}_{\mathsf{p}}))^{\mathsf{T}}\,p(\boldsymbol{\eta}_{\mathsf{p}}|\boldsymbol{Y}_{1:n})\,d\boldsymbol{\eta}_{\mathsf{p}}\,, \tag{2.21}$$

where $\hat{\boldsymbol{\eta}}_{n\mathsf{MMSE}}$ denotes the minimum mean square error (MMSE) estimate of the parameter vector $\hat{\boldsymbol{\eta}}$, w^i is the weight of the i^{th} particle and $\boldsymbol{\eta}^i$ is its value, i.e., its state.

Note: In the following analysis, however, we will restrict the parameters of interest to the three-dimensional (3D) position, i.e., we reduce the parameter vector to $\boldsymbol{\eta}_{\mathsf{p}} := \boldsymbol{p}_n$ and thus $\mathcal{D}_{\mathsf{p}} = 3$.

Since (2.20) is the covariance about our estimated parameters $\hat{\boldsymbol{\eta}}_{\mathsf{p}}^{(k)}$, we need to *propagate* this *uncertainty* to our parameters of interest, i.e., the channel $\boldsymbol{h}$, through [10, Sec. 3.8]

$$\hat{\boldsymbol{C}}_{\mathsf{p}}^{(k)} = \boldsymbol{J}_k \, \hat{\boldsymbol{C}}_{\boldsymbol{\eta}_{\mathsf{p}}}^{(k)} \, \boldsymbol{J}_k^{\mathsf{H}} + \sigma_{\mathsf{r}}^2 \boldsymbol{I} \quad \in \mathbb{C}^{M \times M} \tag{2.22}$$

$$\text{with} \quad \boldsymbol{J}_k = \frac{\partial \widetilde{\boldsymbol{h}}_k}{\partial \boldsymbol{\eta}_{\mathsf{p}}^{\mathsf{T}}} \quad \in \mathbb{C}^{M \times \mathcal{D}_{\mathsf{p}}} \tag{2.23}$$

where $\boldsymbol{J}_k$ denotes the Jacobian matrix computed through the partial derivatives of the parameters $\boldsymbol{\eta}_{\mathsf{p}}^{(k)}$ w.r.t. the channel vector entries from (2.18). A small regularization constant $\sigma_{\mathsf{r}} = 10^{-3}\sigma_n^2$ is added to ensure the invertability of $\hat{\boldsymbol{C}}_{\mathsf{p}}^{(k)}$, because for $\sigma_{\mathsf{r}} = 0$ generally $\operatorname{rank}(\hat{\boldsymbol{C}}_{\boldsymbol{\eta}_{\mathsf{p}}}^{(k)}) \leq \mathcal{D}_{\mathsf{p}}$ and $\operatorname{rank}(\hat{\boldsymbol{C}}_{\mathsf{p}}^{(k)}) \leq M$ and $M \gg \mathcal{D}_{\mathsf{p}}$, which would make $\hat{\boldsymbol{C}}_{\mathsf{p}}^{(k)}$ not invertible.

The entries of the Jacobian $\boldsymbol{J}_k$ in (2.23) are derived in Appendix A.1.

CSI fusion. We perform channel fusion by computing the *fused channel* vector

$$\hat{\boldsymbol{h}}_{\mathsf{f}} = \underbrace{\left(\hat{\boldsymbol{C}}_{\mathsf{m}}{}^{-1} + \sum_{k=1}^{K} \hat{\boldsymbol{C}}_{\mathsf{p}}^{(k)}{}^{-1} \right)^{-1}}_{:=\hat{\boldsymbol{C}}_{\mathsf{f}}} \left(\hat{\boldsymbol{C}}_{\mathsf{m}}{}^{-1} \hat{\boldsymbol{h}} + \sum_{k=1}^{K} \hat{\boldsymbol{C}}_{\mathsf{p}}^{(k)}{}^{-1} \widetilde{\boldsymbol{h}}_k \right) , \tag{2.24}$$

through precision weighting of our measured CSI $\hat{\boldsymbol{h}}$ with our predicted CSI $\widetilde{\boldsymbol{h}}$ where $\hat{\boldsymbol{C}}_{\mathsf{f}} \in \mathbb{C}^{M \times M}$ denotes the covariance matrix of our fused channel vector.

2.1.7 Results

Section 2.1.7 introduces an outline of our algorithm and the measurement dataset acquired. Channel estimation and tracking results are not yet available at the time of this writing, hence they will be contributed to the REINDEER deliverable D5.3 [11] in the future.

Nevertheless, we demonstrate some initial results of our channel fusion method that combines *noisy* measured CSI and predicted CSI along the track of our measurements from Fig. 2.1. Fig. 2.3 shows the path gains (PGs), i.e., the efficiencies, of using the two types of CSI: noisy measured CSI realizations $\hat{\boldsymbol{h}}$ (∘), augmented by a $98\,\%$ confidence interval $U_{98\%}$ (▭) symmetric around the mean (—), and predicted CSI $\widetilde{\boldsymbol{h}}$ (—∘—). Both are compared versus using *perfect*CSI (-·-·-) and the expected SISO efficiency (- - -) equivalent to the efficiency of a random beamformer having *no CSI* available. Our *fused* CSI (—∘—) indicates the result of our channel fusion in (2.24). Note that CSI acquired with the VNA serves as "perfect" *CSI* as it is our best estimate of the ground truth.

Our *predicted* CSI relies only on the LoS path in this investigation, where we assume a known position information of the EN device. In [1], we have shown, that our spherical wavefront SMC beamformer outperforms a spherical wavefront LoS beamformer. As soon as we have our channel estimator and tracker put in place, we will be able to track SMCs which will increase the efficiency of the result in Fig. 2.3 even further.

Our *measured* CSI is generated according to (2.19), where we choose an $\mathrm{SNR} = -6\,\mathrm{dB}$ as

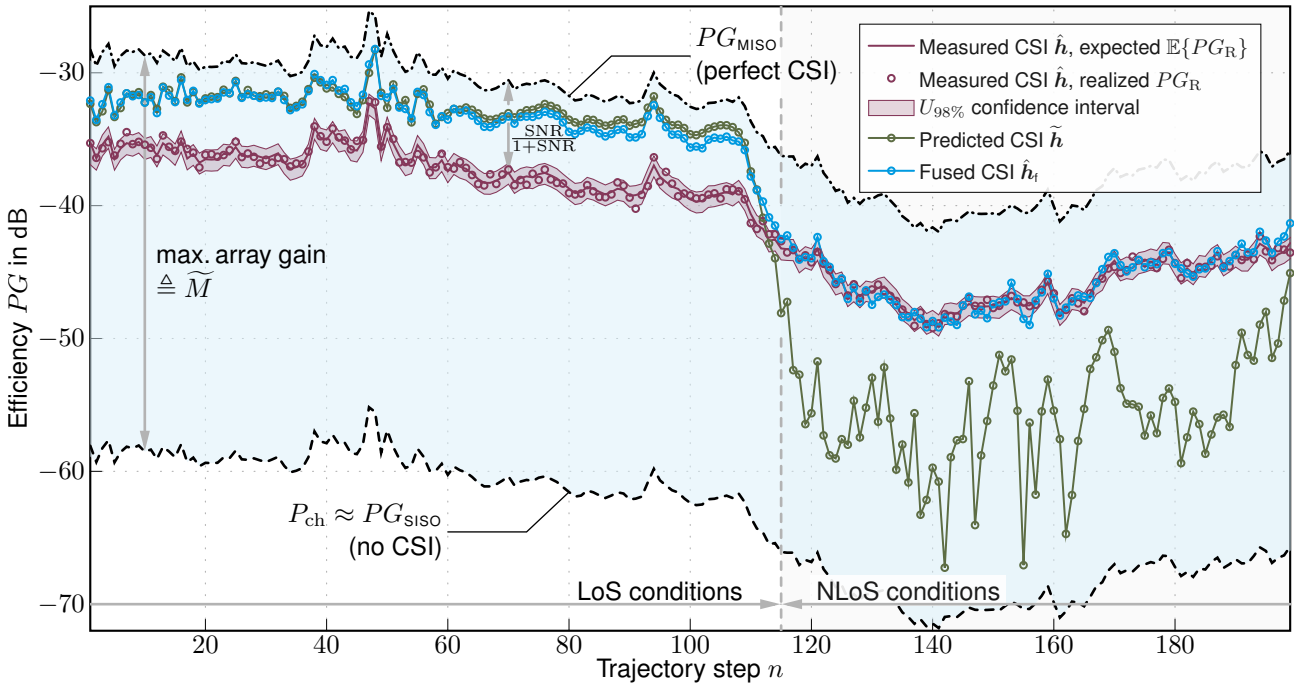

Figure 2.3: Efficiency (i.e., the PG) of beamformers given different types of CSI: A reciprocity-based beamformer using noisy measured CSI $\hat{\boldsymbol{h}}$, a geometry-based spherical wavefront LoS beamformer using predicted CSI $\widetilde{\boldsymbol{h}}$, as well as a beamformer given the fused CSI $\hat{\boldsymbol{h}}_{\text{f}}$ from(2.24).

defined in [1] through

$$\text{SNR} := \frac{1}{M}\|\boldsymbol{C}_{\text{m}}^{-\frac{1}{2}}\boldsymbol{h}\|^2 \tag{2.25}$$

$$= \underbrace{\frac{1}{\sigma_n^2}}_{:=\frac{1}{P_{\text{n}}}} \underbrace{\frac{1}{\widetilde{M}}\|\boldsymbol{h}\|^2}_{:=P_{\text{ch}}} \tag{2.26}$$

$$= \frac{P_{\text{ch}}}{P_{\text{n}}} \tag{2.27}$$

with $\sigma_n^2 = P_{\text{n}}$ denoting the AWGN noise variance per "SISO" channel m to the device. P_{ch} denotes the average channel power per channel m of the noise-free channel $\boldsymbol{h}$, i.e., perfect CSI. In [1], [12], we derived the expected efficiency of a reciprocity-based beamformer to be

$$\mathbb{E}\{PG_{\text{R}}\} \approx \widetilde{M}\, P_{\text{ch}} \frac{\text{SNR}}{1+\text{SNR}} \tag{2.28}$$

in the linear-SNR regime in $1/\widetilde{M} < \text{SNR} < 1$, where $\widetilde{M} \triangleq G_{\text{array}}$ denotes the maximum array gain given perfect CSI. While the efficiency of a reciprocity-based beamformer (◦) may vary due to individual noise *realizations*, we compute its expected efficiency. For the chosen $\text{SNR} = -6\,\text{dB} \approx 25.12\,\%$, the expected efficiency loss (actually a gain < 1) of a reciprocity-based beamformer using measured CSI is approximately $\frac{\text{SNR}}{1+\text{SNR}}$ when compared with perfect CSI (-----) $\hat{\boldsymbol{h}}$. The corresponding result $\mathbb{E}\{PG_{\text{R}}\}$ is indicated by (——) in Fig.2.3 and is closely corresponding to the realizations PG_{R} for the individual steps n along the trajectory. The expected efficiency is augmented by a symmetric $98\,\%$ confidence interval $U_{98\%}$.

Our initial results address the our hypotheses (see Section 2.1) as follows:

1. **Efficiency** With the initial analysis presented, we show (cf. Fig. 2.3) that even a simple geometry-based spherical wavefront LoS beamformer (—◦—) can outperform a reciprocity beamformer (◦) in the *linear SNR regime*[15] and as long as the corresponding beam (i.e., the LoS) is not blocked (which will be tackled by estimating and tracking the component visibility $\chi_n^{(k)}$ in D5.3 [11]). Pilots received from EN devices operating through backscatter communication are likely to have a low SNR and hence our method is particularly valuable in that case.

3. **Robustness:** The robustness aspect of our channel fusion method is demonstrated through the successful selection (actually a combination) of the most reliable type of CSI (i.e., measured and predicted CSI). Rather than relying on a single type of CSI, our method demonstrates (cf. Fig. 2.3) that our fused CSI (—◦—) relies mostly on predicted CSI as long as it outperforms noisy measured CSI in LoS conditions and resorts to measured CSI in case predicted CSI model breaks down due to blockage.

4. **Reliability:** In the initial results presented, we addressed the reliability aspect only in terms of a successful "handover" through *measured CSI* from RWs with less favorable channel conditions to RWs with more favorable channel conditions. Only as soon as our channel estimator and tracker are put into operation, we will be able to detect the LoS blockage and be able to either bypass it through SMCs, or hand over to another set of RWs mounted on the other side of the hallway.

Hypothesis 2 **Mobility Support** will be demonstrated as soon as our channel tracker is fully implemented, as it will largely rely on predicting CSI with a motion model (i.e., a state-space model) that tracks the EN device.

It is worth comparing Fig. 2.14 in the next Section, where another trajectory is presented along which a device is moving from LoS conditions to NLoS conditions. Different schemes for learning and predicting CSI are evaluated. With an appropriate uncertainty measure, these types of predicted CSI can likewise be used to fuse CSI and benefit from 1, 3, and 4.

[15] Refer to [1] for a detailed explanation.

2.2 Geometry-based amplitude modeling

In this section, we analyze channel measurements from a synthetic massive MIMO system interacting with its surroundings and build an amplitude model based on the geometric layout of the indoor environment. We use signal amplitudes extracted from the LoS and MPCs to show the behavior of obstructions in the surroundings of the measurement devices and impact of different building materials on MPCs. For this, we leverage channel estimators in combination with ray tracing techniques to extract the components from the measurements and assign them to the corresponding LoS or specular reflection position using floor plan knowledge. After this pre-processing extraction step, we build a model of the environment using compression and regression techniques. The former reduces the necessary data size to be used while the latter tries to find a predicting function relating a wall position to an amplitude value. Then, the model can be used for interpolation and regression of the signal amplitudes and specular reflections. Finally, we use the environment model to enhance WPT algorithms and show its performance enhancing capabilities.

2.2.1 Measurement environment

A laboratory room on campus of TU Graz at Inffeldgasse 10 is used as environment for investigative indoor measurements. The presence of different building materials (plasterboard, glass, concrete) and many small scattering objects ensures a realistic office indoor measurement scenario. Due to the box shape of the room, all agent measurement positions are in the LoS if no additional obstructions are introduced. Previous measurement campaigns already analyzed the electromagnetic properties for wave propagation inside the laboratory, showing that strong specular reflections are present originating from the northern window wall and southern whiteboard [13], [14]. Thus, the presence of well suited (from a modeling perspective) specular MPCs can be assumed. From earlier measurement campaigns, three-dimensional floor plan information of the room is available and used throughout the data analysis as ground truth information. Figures 2.4 (a) and 2.4 (b) depict the indoor measurement room. As seen in the pictures, the room is not empty, but full of smaller objects that are expected to leads scattering effects within the channel measurements, in addition to the stronger MPCs attributable to walls, windows, floor and ceiling. Fig. 2.4 (a) shows the view from the western back wall to the measurement area antenna positioning device. Fig. 2.4 (b) illustrates the opposite view to the back wall from the point of view of the measurement array. Both walls are adjacent to the measuring synthetic aperture array. A large mechanical positioner in the y-z-plane with dimensions of $2.5\,\mathrm{m} \times 1.6\,\mathrm{m}$ is used to take evenly spaced array measurements of the radio channel, while also accurately tracking the positions of the antennas. The positioner can be used for arbitrary array layouts and number of measurements.

Two measurement scenarios are designed for different use cases. A static scenario comprising six single agent positions, distributed around the laboratory, allows for analysis of the LoS, MPCs and diffuse scattering at different heights and locations in the room. A dynamic, J-shaped trajectory of closely spaced measurements with added obstructions in the form of shelves filled with absorbers is measured to show shadowing that happens during the gradual transition from LoS into NLoS condition. The agent moves along its trajectory and over time, more and more sections of the measurement array become obstructed. The static scenario is depicted in Fig. 2.5 and the trajectory in Fig. 2.6.

Fig. 2.7 displays both the measurement array on the east wall and all measurement locations

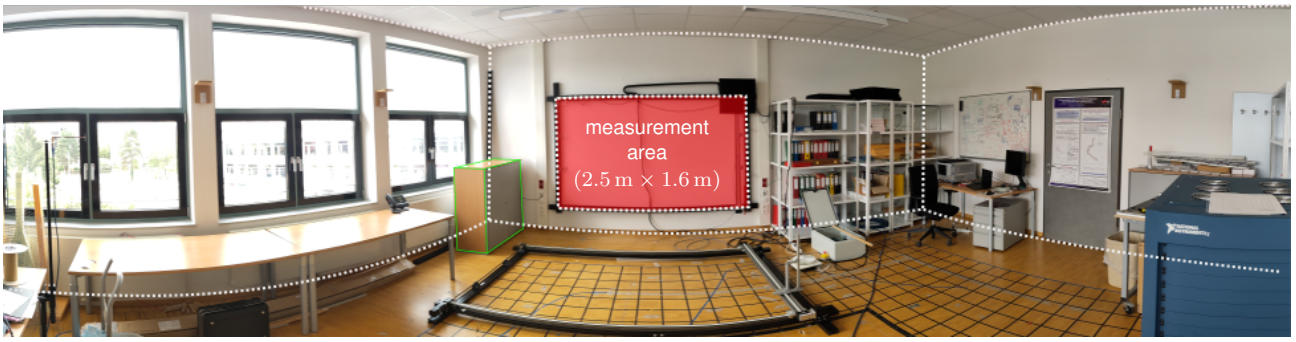

(a) view towards measurement array

(b) view from measurement array to back wall

Figure 2.4: View from inside the room towards the array and from the array into the room. The measurement area that can be covered is indicated as red shaded rectangle. For ease of visualization the corners of the room are highlighted as white dotted lines.

for both campaigns. Trajectory measurements are denoted with a T, while single positions are marked with an S and their respective index. Specular multipath components produced by the north window wall and the west plasterboard wall will be analyzed in detail. These are represented by virtual agent positions that correspond to the mirror images of the agent positions present due to these flat surfaces. The parameters of the west wall and the north window wall extracted from the ground truth knowledge of the floor plan are found in Tab. 2.1. The position vector $\boldsymbol{w}_{\mathrm{P}}$ represents an arbitrary point on the wall

$$\boldsymbol{w}_{\mathrm{P}} = \begin{bmatrix} w_{\mathrm{P,x}} & w_{\mathrm{P,y}} & w_{\mathrm{P,z}} \end{bmatrix} \mathsf{T} \in \mathbb{R}^3, \tag{2.29}$$

the vector $\boldsymbol{w}_{\mathrm{N}}$ defines the orientation of the wall by its normal vector

$$\boldsymbol{w}_{\mathrm{N}} = \begin{bmatrix} w_{\mathrm{N,x}} & w_{\mathrm{N,y}} & w_{\mathrm{N,z}} \end{bmatrix} \mathsf{T} \in \mathbb{R}^3. \tag{2.30}$$

The measurements were performed using a Rohde & Schwarz ZVA24 VNA in a two-port configuration which measured the transmission coefficient $S_{21}(f)$ between the XETS antennas [15] connected to port 1 and 2. The measured frequency bins are uniformly spaced in the respective frequency range. The number of acquired samples is denoted as N_f. All parameters and measurement details can be found in Tab. 2.2.

2.2.2 Amplitude extraction

In this section, the influence of the environment on the received and transmitted signals are modeled, extracted and analyzed. It is assumed that a signal of flat frequency spectrum without

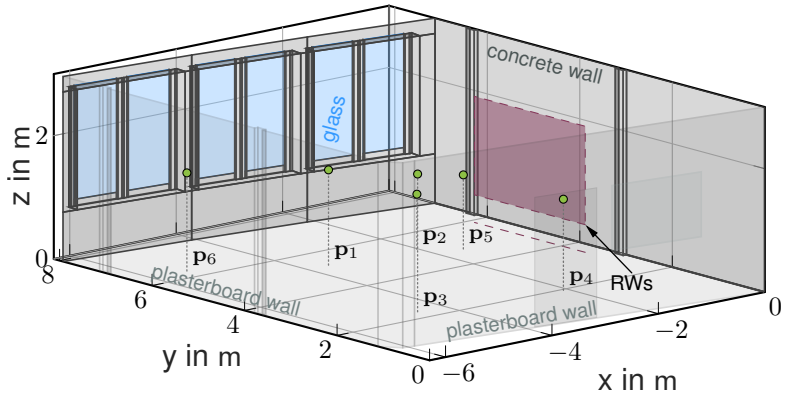

Figure 2.5: The static scenario. Measurement positions in LoS condition used for learning of amplitude and phase characteristics.

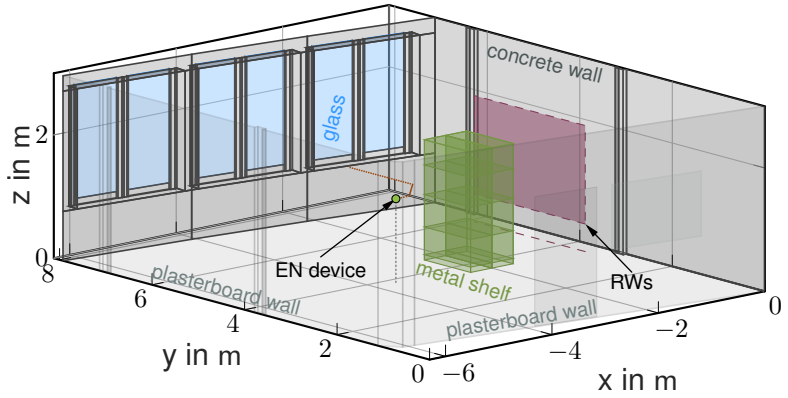

Figure 2.6: The dynamic scenario. An agent is moving on a trajectory around a shelf from LoS conditions to non LoS conditions.

pulse shape and unit energy $S(f)$ is transmitted over the radio channel. In the time domain, this corresponds to an impulse that, once measured at the receiving end, contains the channel impulse response. The corresponding pulse signal $s(t)$ is impinging on the measurement setup with a delay that is proportional to the distance between sending and receiving antenna. Thus, the CIR is modeled as

$$h_{ij}(t) = \alpha_{ij} \times \delta(t - \tau_{ij}), \tag{2.31}$$

where the notation of subscript ij means that antenna j sends a signal to antenna i and $\tau_{ij} = \tau_{ji} = \frac{||\boldsymbol{p}_i - \boldsymbol{p}_j||}{\mathsf{c}}$ is the distance-dependent delay, with c being the speed of light constant. Since a unit energy pulse is transmitted, the energy of the received component is directly linked to $\mid \alpha_{ij} \mid$.

The extension to multiple sending antennas that transmit signals to a measurement setup becomes essential due to the presence of virtual sources even for single physical antenna setups. The superposition principle applies due to the linearity of the wave equation [16] and the impulse

Table 2.1: Wall parameters computed from the floor plan used for amplitude extraction.

Wall	$\boldsymbol{w}_{\mathsf{N}}$	$\boldsymbol{w}_{\mathsf{P}}$
West wall	$\begin{bmatrix}-1 & 0 & 0\end{bmatrix}^{\mathsf{T}}$	$\begin{bmatrix}-6.35 & 0 & 0\end{bmatrix}^{\mathsf{T}}$
Window wall	$\begin{bmatrix}0.105 & 0.994 & 0\end{bmatrix}^{\mathsf{T}}$	$\begin{bmatrix}-2.578 & 7.72 & 0\end{bmatrix}^{\mathsf{T}}$

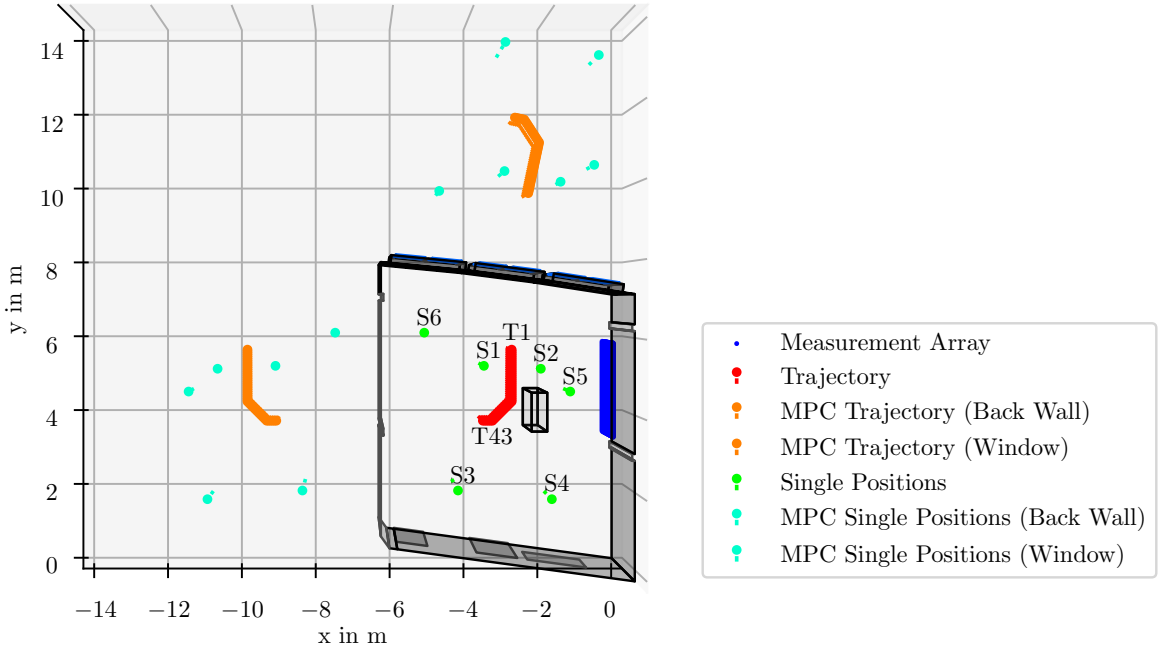

Figure 2.7: Three-dimensional illustration of the demo room measurement setup for trajectory and single positions including virtual agents.

responses of all channels that impact one measuring antenna i are summed up

$$h_i(t) = \sum_{k \in K_i} \alpha_i^k \times \delta(t - \tau_{ji}^k),$$

where the set $K_i = \{0, \ldots, K\}$ contains the indices of all antennas corresponding to the physical antenna i and index $k = 0$ denoting the physical component, while larger indices $k > 0$ are reserved for virtual positions. The physical and virtual antenna positions are collected into the set $\mathcal{P}\{\boldsymbol{p}_{A,i}^k, k \in K^i\}$ for each receiving antenna.

The received measurement is a convolution of the sent signal and the channel with additive white

Table 2.2: Measurement settings used for the synthetic aperture massive MIMO test bed.

Campaign	Index	Array Dimensions $(L_x \times L_y \times L_z)$	f_{min} GHz	f_{max} GHz	N_f	RX/TX
(T)rajectory	1 - 43	$(1 \times 89 \times 59)$	3.5	7.5	1024	XETS/XETS
(S)ingle	1 - 3	$(1 \times 112 \times 75)$	3	10	4096	XETS/XETS
(S)ingle	4 - 6	$(1 \times 112 \times 75)$	3	10	2048	XETS/XETS

Gaussian process noise $\nu(t)$ described by a double-sided power spectral density of $N_0/2$.

$$y_i(t) = h_i(t) * s(t) + \nu = \sum_{k \in K_i} \alpha_i^{(k)} \times s(t - \tau_{ji}^k) + \nu(t) \tag{2.32}$$

The frequency domain representation is straightforward and needed to describe the VNA measurements

$$y_i(f) = \sum_{k \in K_i} \alpha_i^k \times s(f) \times \exp\{-2j\pi f \tau_{ji}^{(k)}\} + \mathcal{V}(f), \tag{2.33}$$

where $\mathcal{V}(f)$ is the Fourier transform (FT) of the noise proccess.

The distance dependency of the channel becomes visible when stacking measured array signals. For measurements of close antennas, the LoS wavefront arrives earlier than for measurements where the two antennas are farther apart. This behavior is shown in Fig. 2.8, where the time domain signals of the first measurement from both scenarios are compared to the calculated distances from the floor plan and antenna location knowledge. The three distance lines show which amplitudes are to be extracted, with the LoS component hitting the receiving antenna first. This illustration also confirms the correctness of the computed distances, as they correspond well to the magnitude peaks in the signal. The phase values are nearly constant before the first wavefront, change when the wave hits, and are random afterwards. The randomness may be caused by diffuse scattering and the interplay of MPCs and diffuse multipath components (DMCs).

The extraction of amplitude information is carried out utilizing a best linear unbiased estimator (BLUE) as described in [17], in conjunction with a channel model that compensates for path loss using the Friis equation [18]. The estimates for all amplitudes of an array for a distance vector containing the distances between sending and receiving antennas are given by

$$\boldsymbol{\alpha} = \mathrm{diag}(\boldsymbol{C}(\boldsymbol{d})^{\mathsf{H}} \boldsymbol{Y}) \cdot \frac{\boldsymbol{d}}{N_f}. \tag{2.34}$$

Here, N_f denotes the number of frequency bins in the discrete-time Fourier transform (DTFT), $\boldsymbol{d}$ represents the vector containing the distances between transmitting and receiving antennas, $\boldsymbol{Y}$ signifies the stacked measurement in the frequency domain, and $\boldsymbol{C}(\boldsymbol{d})$ is the matrix for the distance-dependent channel model given by

$$\boldsymbol{C}(\boldsymbol{d}) = \exp\{\frac{-2j\pi}{\mathrm{c}} \boldsymbol{d} \otimes \boldsymbol{f}\}. \tag{2.35}$$

The absence of a signal component before the LoS impact allows for the estimation of the noise level using a variance estimator for the antenna ensemble

$$\sigma = \sqrt{\frac{1}{L} \frac{1}{T_{\mathsf{noise}}} \sum_{i=1}^{L} \sum_{t=1}^{T_{\mathsf{noise}}} \mid y_i(t) - \mu_y \mid^2}, \tag{2.36}$$

with

$$\mu_y = \frac{1}{L} \frac{1}{T_{\mathsf{noise}}} \sum_{i=1}^{L} \sum_{t=1}^{T_{\mathsf{noise}}} y_i(t) \tag{2.37}$$

of the noisy measurement $y_i(t)$ at time index t for all antennas i in the array with number of antennas L. The moment in time T_{noise} is chosen such that only noise samples are taken into

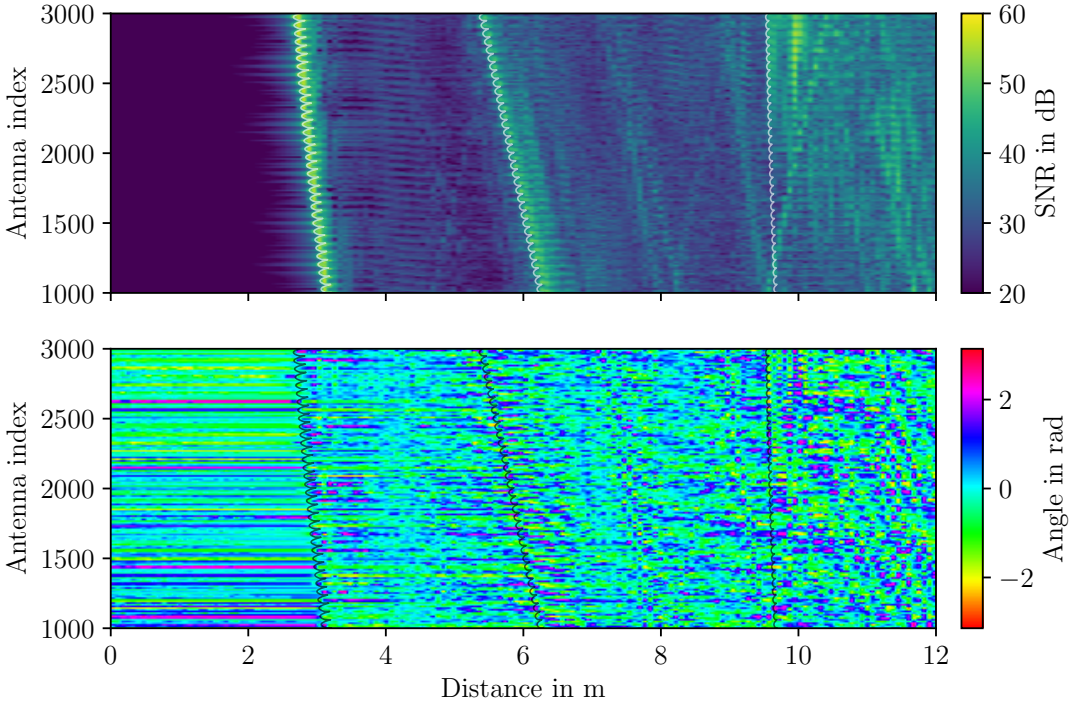

(a) Channel impulse responses measured at trajectory position 1.

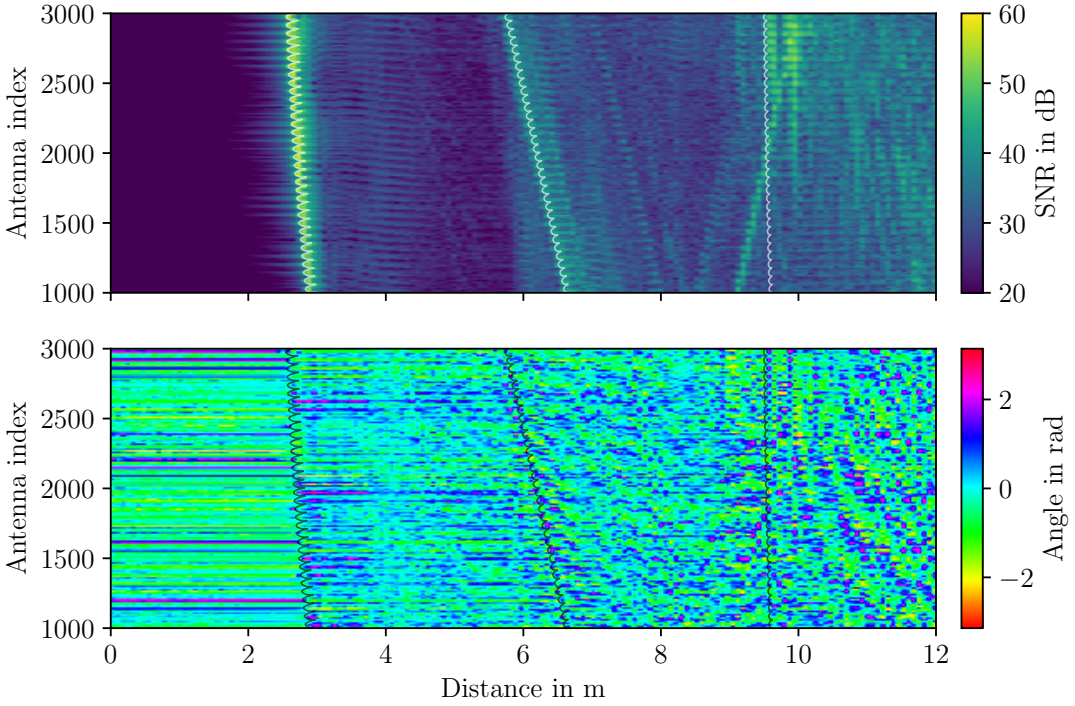

(b) Channel impulse responses measured at static position 1.

Figure 2.8: Stacked time-domain channel measurements and comparison to distance from measurement array to physical/virtual antennas.

consideration. The noise level estimate is then used to compute the SNR together with the magnitudes of the signals

$$\alpha_{\text{SNR}} = 20 \cdot \log_{10} \frac{\alpha}{\sigma}, \tag{2.38}$$

used in all representations of the signal magnitude.

2.2.2.1 Line-of-Sight

The amplitudes of the first impinging wavefront $k = 0$ are extracted and illustrated over the antenna positions of the array in Fig. 2.9. The LoS path is not yet affected by multipath propagation effects, but the deterministic influence of the antenna gain pattern can be seen. As the path loss is already compensated for, one would expect the two measurements to produce the same results, which however is not the case.

The difference in the surroundings of the measuring antenna in the trajectory case may be the cause of this. According to Fresnel's theory of additional aberrant waves due to obstructions near the direct path, either constructive or destructive inference can be observed [19]. The order n of the Fresnel zone together with the distance from transmit antenna to obstruction d_1, from receive antenna to obstruction d_2 and carrier frequency f_c determines the radius r_n around the direct path in which an obstruction affects signal transmission

$$r_n = \sqrt{\frac{n \cdot d_1 \cdot d_2 \cdot f_\text{c}}{d_1 + d_2}}. \tag{2.39}$$

This radius spans an ellipsoidal region around the ray cast from transmit to receive antenna. Obstructions in these regions produce aberrant waves due to reflections which either result in constructive or destructive inference. The obstructing shelf is present in the first Fresnel region which creates an additional wave that is shifted by less than a quarter wave-length or $90°$. This effect creates constructive inference in the received magnitude and a shift in the phase.

The magnitude and phase course over the array is smoother in the unobstructed case while interference is present in the obstructed case. Variations in the measured signal due to the angle-dependent antenna gain pattern also need to be considered when comparing the extracted amplitudes from the different scenarios.

2.2.2.2 Multipath components

The amplitude extraction process is repeated for the virtual agent positions $k > 0$ with an additional ray tracing step to find the intersection points in the environment that are hit during wave propagation. The locations of the analyzed virtual and physical agents remain the same, which are the first trajectory position and first single measurement. The magnitudes and phases of the extracted amplitudes are now shown over the respective wall segments.

Fig. 2.10 displays the extracted amplitudes at their reflection points on the western wall segment. The impact of the obstructing shelves can be observed, as the received magnitudes are lower on the left half of the wall segment. This effect also shows in the phase behavior, where visible parts of the wall exhibit a continuous course, while blocked sections only display randomly distributed noisy angles. This is even more evident examining the phase behavior of the unobstructed measurement, which shows minimal phase fluctuations across the entire back wall segment.

The amplitudes extracted from the fully visible northern window wall segment shown in Fig. 2.11, exhibit different behavior. Due to the non-uniformity of the building materials (glass, metal, etc.),

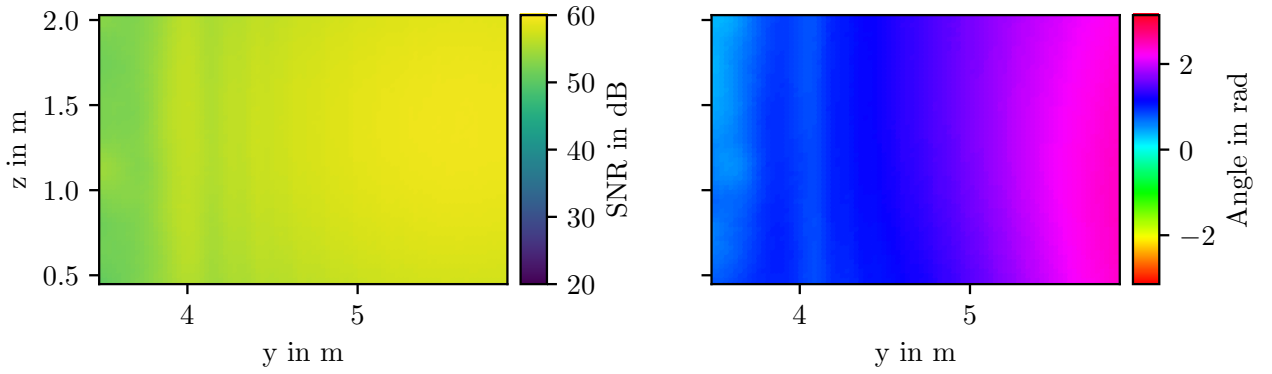

(a) Trajectory position 1.

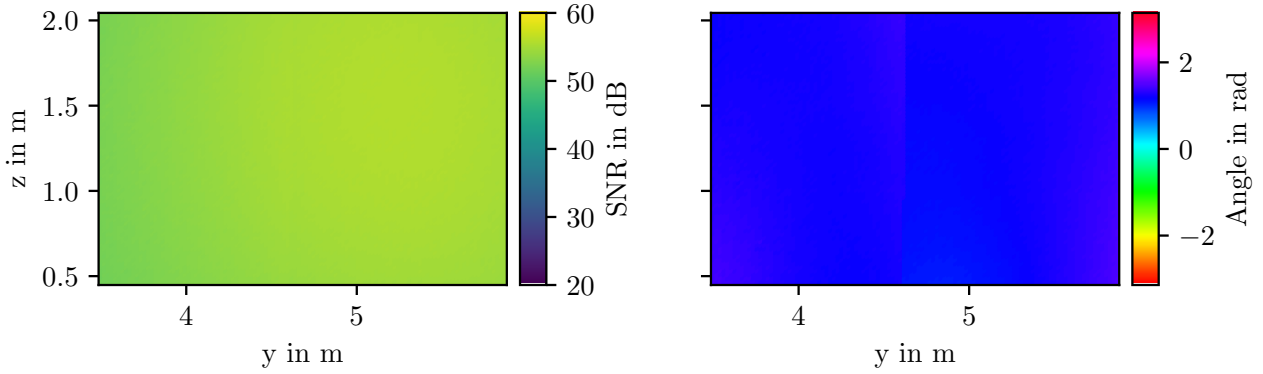

(b) Static position 1.

Figure 2.9: LoS magnitude and phase for the measurement antenna array elements compared for the first position of each measurement campaign.

the phase behavior is not consistent throughout the entire section, but rather varies in different spots. Furthermore, the window wall on the northern side has a slight curve, which cannot be accurately modeled using only two wall vectors describing a plane. As a result, estimating the amplitudes is imprecise which also affects the extracted angle.

2.2.2.3 Conclusion

Structural patterns in both magnitude and phase behavior indicate that information is present in both components and should be considered for further evaluation. The environment of the measurement system affects not only the MPCs in the received signal, but also the LoS component. The amplitudes are shaped and affected in magnitude and phase values depending on the objects present in the vicinity of the transmit and receive antennas and their characteristics. Obstructions lower the received magnitude and randomize the phase behavior, objects in the different Fresnel zones produce either constructive or destructive interference, and the antenna layout also changes the behavior of the observed amplitudes.

Moving on to MPCs, the surface and building material of the specularly reflecting surfaces encountered during signal propagation will affect the signals depending on their specular reflection coefficient. In an indoor environment, however, not only perfectly specular reflections can be observed, but also reflections from diffuse reflectors or even diffuse scatterers.

The discussed model only considers an amplitude snapshot at a specific delay or time instance,

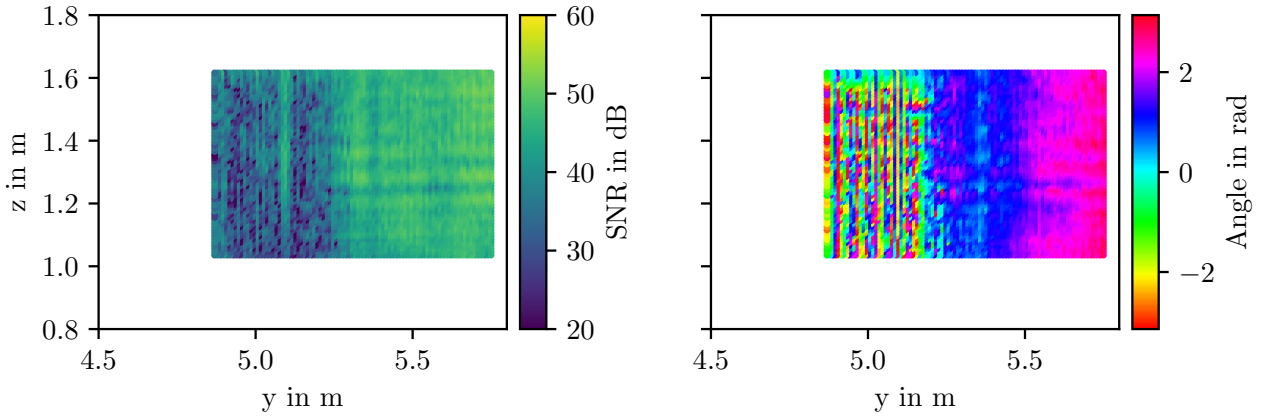

(a) Trajectory position 1.

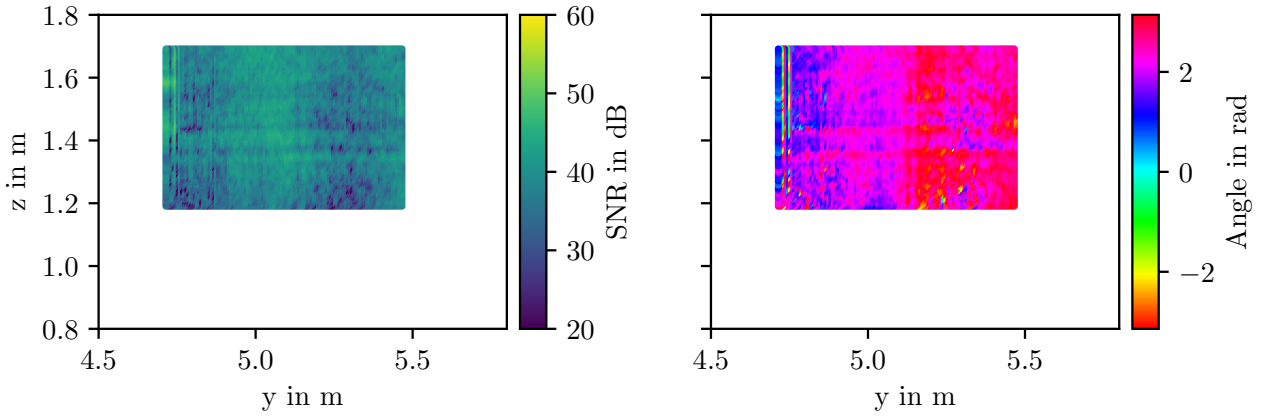

(b) Static position 1.

Figure 2.10: Extracted back wall intersection amplitudes for the first single (unobstructed) and trajectory (obstructed) measurement position.

which means that these more diffuse effects cannot be fully described. Another drawback of modeling an indoor propagation channel with reflective surfaces is the inability to describe curved surfaces. To model curved objects, diffuse scatterers, or imperfect specular reflectors, multiple snapshots with slight variance in the delay domain could be used. This would lead to a ”fuzzy” description of the environment capable of dealing with different types of objects.

The presented methods still rely on an exact knowledge of the floor plan. In reality, this assumption is impossible to make, since the ground truth knowledge is either inaccurate or not available at all. With this limitation, the extraction of amplitude values may still be possible, but since phase values fluctuate faster in space, the extraction of angular information is not possible.

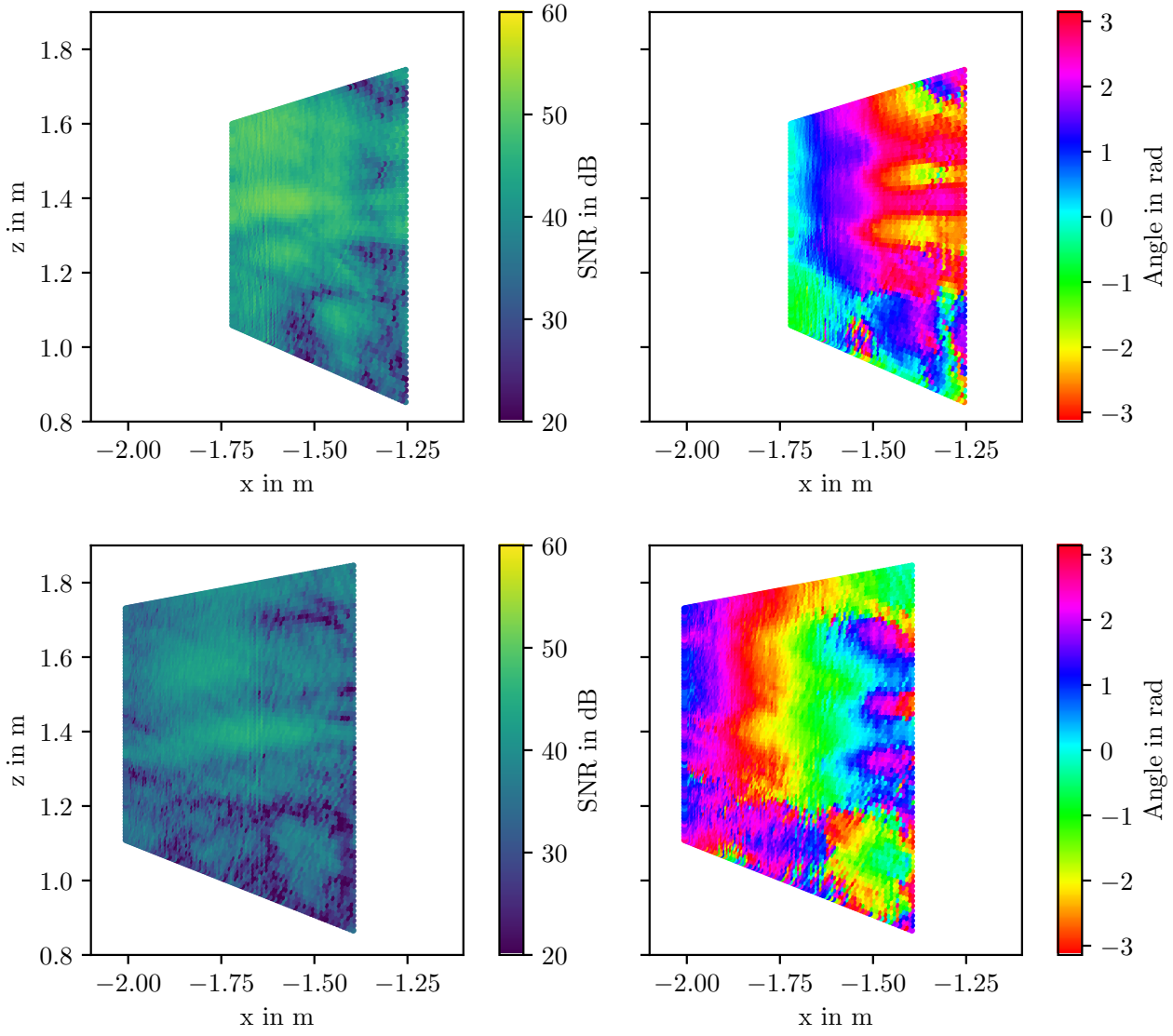

Figure 2.11: Extracted window wall intersection amplitudes for the first single and trajectory measurement position.

2.2.3 Environment modeling

This section discusses the efficient storage of signal amplitudes and the reuse of channel measurements at new, previously unseen locations. One of the biggest downsides of massive MIMO systems is the large amount of data to be processed. To counteract against this limitation, data compression algorithms could be employed to reduce the data load. After storing the extracted data about the surroundings of the measurement system, a model of the environment could be leveraged to enhance the performance of other algorithms such as WPT or tracking applications by interpolation and prediction of CSI at arbitrary locations.

To model the environment, wall intersection amplitudes extracted from channel measurements are processed and associated with their respective reflective surfaces. The data association step can be performed using either known floor plan knowledge (as shown in the previous section) or a channel estimator, when knowledge of the environment is not available. First, FT based data compression methods are developed and applied to the extracted wall components. Then, the reconstruction capabilities are evaluated, showing how well the data can be recovered after compression. Finally, in an application example of WPT, the trajectory measurements are used to compare different channel modeling approaches for MRT. WPT is also used to analyze the prediction horizon of beamforming weights extracted at different trajectory positions and to decompose the channel into LoS, MPCs and diffuse scatterers to show the energy distribution.

After extracting the wall features at a trajectory or static measurement position, environment modeling can be formulated as a regression or prediction task, where the training data set consists of a set of wall points $\hat{\boldsymbol{p}}$, together with their extracted amplitude $\hat{\alpha}$

$$\{\mathcal{X}, \mathcal{Y}\} = \{\{\hat{\boldsymbol{p}}\}, \{\hat{\alpha}\}\}. \tag{2.40}$$

A function $\mathsf{Y} : \mathcal{X} \rightarrow \mathcal{Y}$ predicting amplitude (magnitude and phase) information at arbitrary points $\boldsymbol{p}$

$$\tilde{\alpha} = \mathsf{Y}(\boldsymbol{p}) \tag{2.41}$$

is searched for. A simple and straightforward machine learning technique for regression is the k-Nearest-Neighbors (kNN) approach, which uses the k nearest wall points and calculates an average over their values for interpolation. The advantages of such an algorithm are mainly the simplicity of the learning step, since it operates directly on the available data and the ability to deal with highly local features, since it only considers the nearest points. However, it is also highly sensitive to noisy outliers in the data, which is problematic in safety-critical systems. Another downside is the memory consumption of the algorithm, since all data points must be stored at all times [20].

When dealing with sequential signals transmitted from a moving target, the amount of data to be stored and processed increases rapidly. At each trajectory step of the agent, for each wall segment, as many intersection points as antenna elements in the massive MIMO system are possible and can be extracted. For the measurement setup in the lab room, this would require $89 \times 59 \times (5+1) \times 43 = 1,354,758$ complex data points, where 89×59 are the array dimensions, $(5+1)$ the number of virtual and physical agents considered, and 43 the number of trajectory positions. The latter can become arbitrarily large in a tracking scenario, so a data reduction method that can, in the best case, combine the regression and compression tasks becomes essential.

Based on the idea of JPEG [21], a compression algorithm based on the FT is developed. Since JPEG deals with real-valued data, the approach has to be adapted for complex-valued amplitude

data, resulting in the use of the FT instead of the cosine transform (CT). Due to the nature of the FT, oversampling and interpolation is possible. An anti-aliasing low-pass filter is applied before each transformation step to eliminate unwanted frequency components in the spectrum. The wall intersection points are shaped into a matrix of the same size as the measurement array and transformed into frequency domain using a two-dimensional discrete Fourier transform (DFT).

$$\boldsymbol{P}_{k_1,k_2} = \sum_{n_x=0}^{L_x-1} \sum_{n_y=0}^{L_y-1} \boldsymbol{P}_{n_x,n_y} \times \exp\left\{-j\frac{2\pi n_x}{L_x}k_1\right\} \times \exp\left\{-j\frac{2\pi n_y}{L_y}k_2\right\}. \tag{2.42}$$

The two image dimensions x and y are brought into a two-dimensional frequency space indexed by k_1 and k_2. All frequency bins smaller than a chosen percentage of the maximum are set to zero and only the remaining are kept. This becomes the transformed lossy compressed wall "image" to be stored. Once necessary, the inverse of the transform

$$\boldsymbol{P}_{n_x,n_y} = \frac{1}{L_x \cdot L_y} \sum_{k_1=0}^{L_x-1} \sum_{k_2=0}^{L_y-1} \boldsymbol{P}_{k_1,k_2} \times \exp\left\{j\frac{2\pi n_x}{L_x}k_1\right\} \times \exp\left\{j\frac{2\pi n_y}{L_y}k_2\right\} \tag{2.43}$$

can be applied to the compressed frequency domain image to reconstruct the original image. This process is fully deterministic and relies on the fact that the position domain image is not a random collection of "pixels", but can be described by a superposition of multiple sine and cosine functions.

The FT based compression and reconstruction process is now shown for the amplitudes extracted from the back wall in the lab room at the first trajectory position. Amplitudes lower than 90% relative to the frequency bin with the highest magnitude are discarded (set to zero), which reduces the number of complex valued data samples to be stored from 5251 to 336. Thus, the algorithm is able to achieve a compression level of 93% relative to the uncompressed "image". The mean-square of the reconstruction error was evaluated which resulted in a value of 0.011. Figures 2.12 and 2.13 display the different steps of the algorithm, comparing the magnitude and phase of the original and reconstructed wall images and also showing intermediate steps. The first intermediate step is the two dimensional frequency domain representation of the wall amplitudes, shown in the lower left part of the figure. The result after thresholding in the spectrum is shown in the lower right part, where unwanted components are set to zero and not depicted anymore.

The image in the upper left corner shows the original extracted wall amplitudes, which can be compared to the reconstructed image in the upper right corner. The reconstructed image displays fewer random fluctuations in magnitude and phase behavior due to the anti-aliasing low-pass filter in the pre-processing step and the filtering nature of the FT. The amplitudes are overall well reconstructed by the Fourier transform-based method. The bottom half of Fig. 2.12 and 2.13 displays the frequency domain representation of the signal amplitudes. The left-hand side shows the transformed original image, while the right-hand side shows the bins that contain the most information and are kept for further processing. This demonstrates the level of compression and reduction that is possible using such an algorithm.

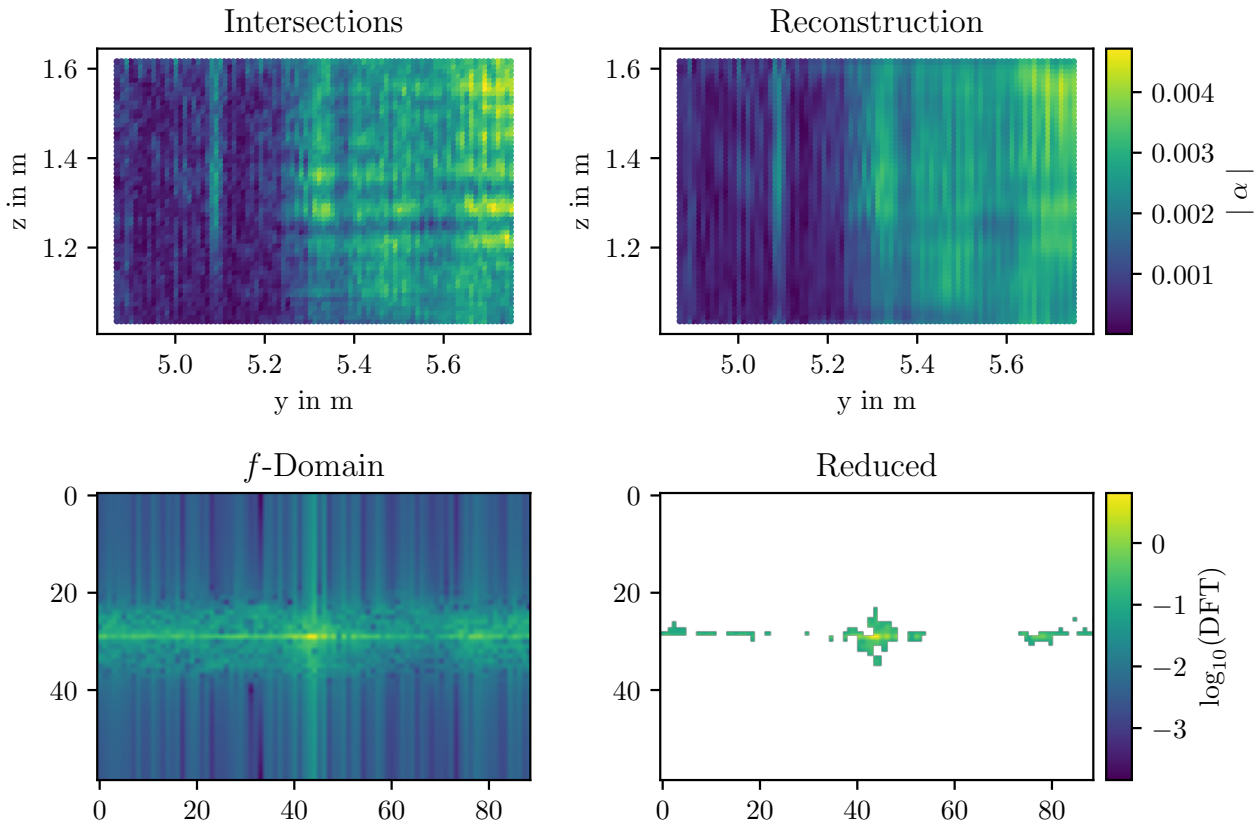

Figure 2.12: From left to right and top to bottom: Extracted back wall magnitudes, reconstructed wall segment magnitudes, magnitudes frequency domain representation of the extracted wall segment and remaining frequency bins after application of the compression threshold.

2.2.4 Application to wireless power transfer

Prediction This section analyzes the prediction and interpolation capabilities of the FT based compression algorithm presented earlier. It will be applied to a practical wireless power transfer scenario, where an agent moves along a trajectory and is tracked. To avoid introducing unnecessary inaccuracies into the analysis, the ground truth agent positions are used for geometric position information. However, the process could be extended with a tracking algorithm, such as a tracking Kalman filter, to retrieve a-priori estimates of the agent's position. The amplitudes are extracted from the ultra-wideband (UWB) measurements using floor plan knowledge to find the virtual agent (VA) positions, but also this step could be extended to include a channel estimator which finds the mirrored agent positions. Prediction of CSI is performed from measurements of the closest available position, i.e. the previous step in the trajectory.

At each trajectory step, indexed by $t \in \{1, \ldots, 43\}$, the CSI is measured as $\boldsymbol{h}_t$. For the channel model $\tilde{\boldsymbol{h}}_t$, the predicted amplitudes $\tilde{\boldsymbol{\alpha}}$ are used in conjunction with Eq. (2.33) for a superposition of all channel components

$$\tilde{\boldsymbol{h}}_t(f, \boldsymbol{d}_t, \boldsymbol{d}_{t-1}, \tilde{\boldsymbol{\alpha}}_t) = \sum_{k \in K} \mid \tilde{\boldsymbol{\alpha}}_t^{(k)} \mid \times \exp\left\{ \frac{-2j\pi \cdot \boldsymbol{d}_t^{(k)}}{\mathrm{c}} \cdot f \right\} \times \exp\left\{ j\angle\tilde{\boldsymbol{\alpha}}_t^{(k)} + \frac{2j\pi(\boldsymbol{d}_t^{(k)} - \boldsymbol{d}_{t-1}^{(k)})}{\mathrm{c}} \cdot f \right\}, \tag{2.44}$$

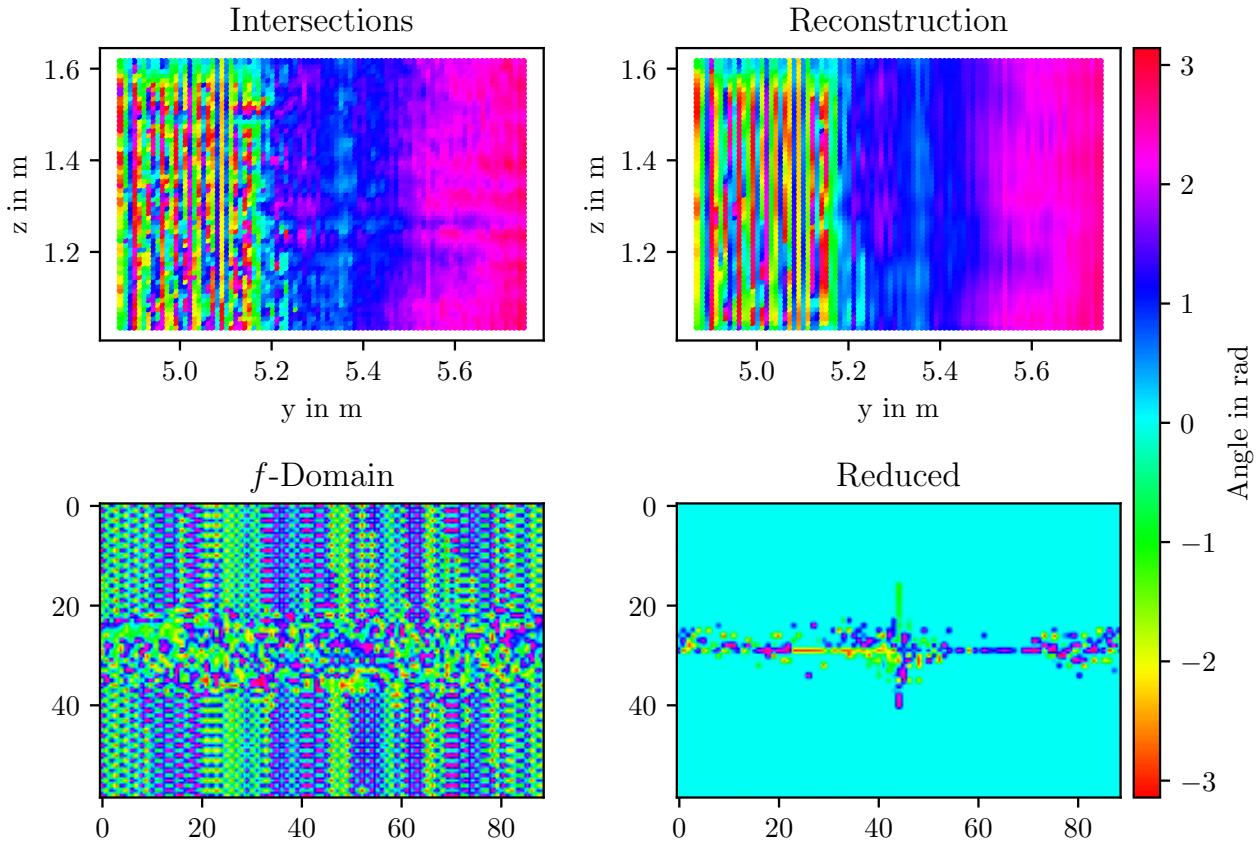

Figure 2.13: From left to right and top to bottom: Extracted back wall phase values, reconstructed wall segment phase course, frequency domain representation of the extracted wall segment and remaining frequency bins after application of the compression threshold.

where t is the trajectory step index, k denotes the index of the LoS ($k = 0$) or MPCs ($k > 0$), c is the speed of light constant, $\boldsymbol{d}_i$ contains the distances from the antenna array elements to the physical or virtual agent either at index t or $t-1$ and f is the operating frequency. An additional phase shift needs to be included in order to account for the movement of the agent from one time instance to another, which is taken into consideration in the second phase term. MRT is used to compute beamforming weights at the selected frequency of $f = 3\,\text{GHz}$ for the array antenna elements, using the modeled channel vectors $\tilde{\boldsymbol{h}}$ according to the following beamforming scheme

$$\boldsymbol{w}_t = \frac{\tilde{\boldsymbol{h}}_t^*}{|| \tilde{\boldsymbol{h}}_t^* ||}. \tag{2.45}$$

The received path gain at the agent for a measured channel $\boldsymbol{h}$ is then computed as

$$\gamma_t = 20 \cdot \log_{10} \left(| \boldsymbol{h}_t^{\mathsf{T}} \boldsymbol{w}_t | \right). \tag{2.46}$$

The achievable path gain γ_t for different methods of computation of the MRT beamforming weights is now compared. The amplitudes of the LoS component and an additional five MPCs, namely the back wall, window wall, south wall, floor, and ceiling are available together with the agent and wall locations are considered.

- Perfect CSI ▬
  The measured CSI knowledge at the current trajectory t is used as a benchmark case to compare perfect knowledge of the channel to the modeled approaches.

- Channel model (kNN)
  The CSI at the current agent position t is predicted using a kNN algorithm which stores all wall locations together with their amplitudes from the previous trajectory step $t-1$. To compute the average in each point, the $k = 10$ nearest neighbors are used.
- Channel model (FT)
  Relying on the FT based algorithm, the MPCs and the LoS amplitudes from trajectory step $t-1$ are compressed and reconstructed to be used in the CSI model at the current trajectory index t.
- Outdated CSI
  As a comparison algorithm, the perfect CSI model from time step $t-1$ is stored and re-used for the current time instance t. This is repeated at every trajectory index.
- Geometry-based channel model
  This model does not consider any signal amplitudes and only models the LoS component using the current position of the agent at time t.

In Fig. 2.14, the course of the received power using the different channel modeling schemes is shown over the trajectory of the moving agent. Additionally, the influence of the MPCs used in the kNN based model on received power are displayed.

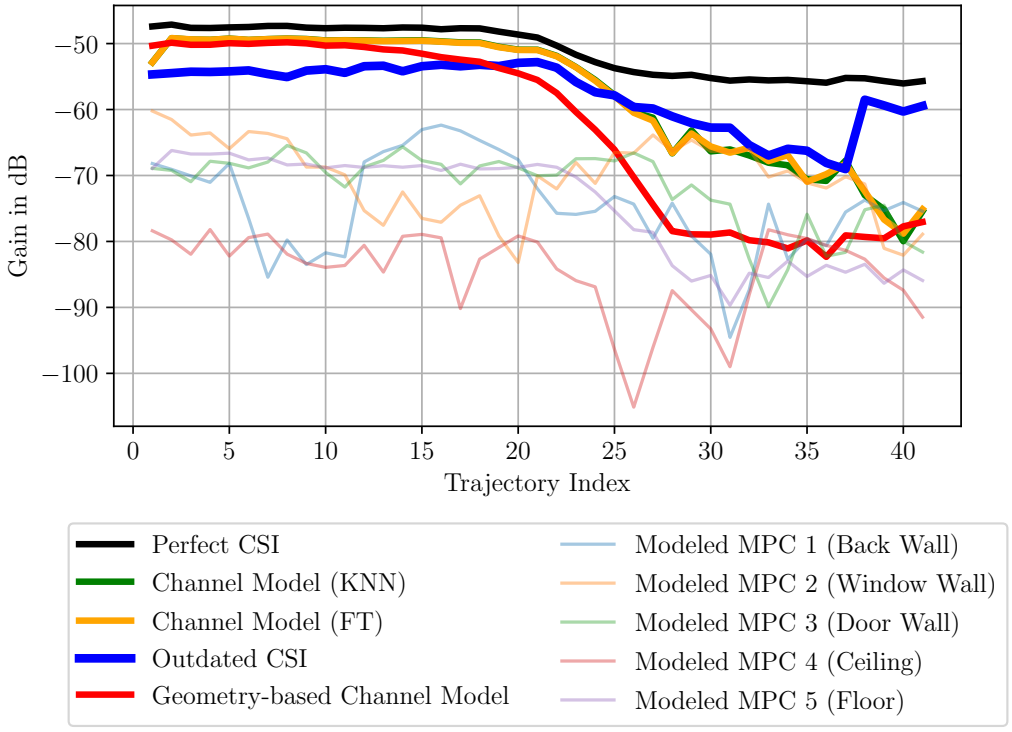

Figure 2.14: Received signal power over the trajectory for different MRT beamforming weights.

The impact of the obstructing shelves is evident as there is a decrease in received power at around trajectory index 20. When the obstruction completely blocks the agent, the importance of utilizing MPCs becomes apparent. The window wall is the primary contributor to the received power, but its impact decreases slightly at certain positions.

A significant improvement in performance is possible when augmenting the geometry-based model of the fully visible LoS with the signal amplitudes and additional MPCs. Both algorithms

that leverage MPCs are more efficient and nearly achieve the outcome of MRT using perfect CSI. When comparing the two modeling approaches (kNN and FT based), the results are very close. This shows, that using the compression algorithm, due to its low reconstruction losses, it is possible to only store a small amount of data compared and still be able to perform maximum ratio transmission with the reconstructed channel vector. A jump in performance can be seen from trajectory index 1 to 2, as in the first iteration of the WPT process, the difference in phase due to movement from one position to another cannot be compensated for. Once the a-priori for the new position estimate is possible, the second phase term in Eq. (2.47) is able to deal with the additional phase shift. The results of the outdated CSI weights are initially worse than all model based methods, but after $t = 25$, this changes possibly due to the large influence of DMCs which are completely disregarded. Since the environment is highly cluttered with diffuse scatterers, large parts of the channel cannot only be described by specularly reflecting surfaces and alternative models are necessary. The beamforming weights from previous steps exploit these diffuse reflections and are able to increase the received power at the agent.

The optimal value given by full channel state information from the current time step is not reached for multiple reasons. First of all, the constructed channel models are simply predictions of the current trajectory iteration and errors are unavoidable. Next, uncertainties in the physical and virtual agent position propagate further to the wall positions which results in deviations in the extracted amplitude values. Finally, systematic measurement setup errors should also not be disregarded, since there might be deviations in the ground truth position or floor plan information and the antenna delay which needs to be compensated on both ends, transmitting and receiving.

Prediction Horizon The prediction horizon describes how well constant beamforming weights keep their WPT capabilities for a changing agent position. Using the decomposition of the channel into LoS and MPCs, the beamforming weights are directly computed without any prediction or interpolation step. For each antenna, the assigned amplitude $\hat{\alpha}_t$ and wall intersections $\hat{\boldsymbol{p}}_t^{(k)}$ are used to build the channel model

$$\hat{\boldsymbol{h}}_t(f, \boldsymbol{d}_t, \hat{\boldsymbol{\alpha}}_t) = \sum_{k \in K} \mid \hat{\boldsymbol{\alpha}}_t^{(k)} \mid \times \exp\left\{ j \angle \tilde{\boldsymbol{\alpha}}_t^{(k)} \right\} \times \exp\left\{ \frac{-2j\pi \cdot \boldsymbol{d}_t^{(k)}}{\mathrm{c}} \cdot f \right\}. \tag{2.47}$$

To analyze the loss in performance when simply keeping the beamforming weights for WPT constant, the prediction horizon of four weight vectors, $\boldsymbol{w}_0$, $\boldsymbol{w}_{10}$, $\boldsymbol{w}_{20}$, $\boldsymbol{w}_{30}$, i.e. computed at indices 0, 10, 20 and 30 are used for WPT over the full course of the trajectory. Fig. 2.15 shows the possible path gain over the trajectory indices in the four cases, compared to the weights computed using perfect CSI. The best possible outcome for a given weight vector lies around the trajectory index used for beamforming and the received path gain at the agent drops quickly when not adapting the weights at each time instance.

Diffuse Scattering To show the influence of the direct path, MPCs and diffuse scatterers, MRT is performed for different parts of the reconstructed channel vector. The extracted amplitudes from the current trajectory step t are directly used as amplitudes for the geometry-based model of the channel which is then split up into its different components. To find the residual of the channel vector not described by the modeled specular reflections, the full channel model $\hat{\boldsymbol{h}}$ (see Eq. (2.47)) is subtracted from the measured signal

$$\hat{\boldsymbol{h}}_{\mathrm{DMC}} = \boldsymbol{h} - \hat{\boldsymbol{h}}. \tag{2.48}$$

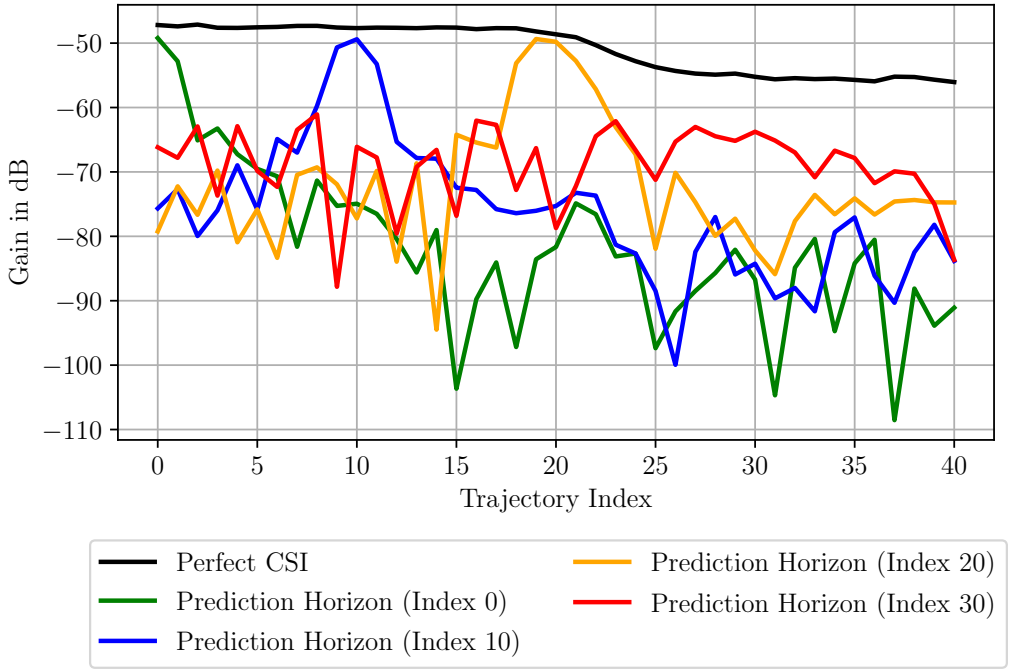

Figure 2.15: Performance evaluation of the prediction horizon for MRT beamforming weights computed from channel models at different trajectory time indices.

The results of MRT using the different extracted components of the channel model are shown in Fig. 2.16, where the received path gain of each method is again compared to a perfect CSI model.

When the LoS condition is given, most of the energy of the channel from array to agent lies within the direct path ▬. In this part of the trajectory, the performance of the weights computed using LoS and full model ▬ nearly overlap. Once visibility to the agent is blocked, the behavior changes and most of the power is transmitted through the MPCs weights ▬. However, the channel cannot be fully modeled only using the LoS and specular MPC which can be seen in the results from the WPT scheme using the diffuse part of the channel ▬. Initially, the path gain of the full model and diffuse weights is similar, due to the environment being full of small scattering objects. Thus, large parts of the channels energy lies within components that cannot described by specular reflections. Such an environment is typical for an indoor setting, thus additional modeling steps for the diffuse part of the channel should be made. After trajectory index 30, the channel exhibits mostly diffuse behavior, since the LoS component vanishes. Still, the contribution of the modeled MPCs varies about ± 5dB over the course of the trajectory.

2.2.5 Conclusion

Knowledge about flat surfaces in the environment and their reflectivity properties with respect to the line-of-sight can drastically improve the efficiency and robustness of wireless power transfer algorithms. When the line-of-sight condition is not given, geometric beamforming or other methods which only exploit the direct path suffer. Previous channel state information should not be disregarded as it contains valuable information about future radio channels. The prediction horizon of previous beamforming weights is rather small, meaning that the parameters need constant tuning in order for the system to remain efficient and robust. Using old CSI, an environment

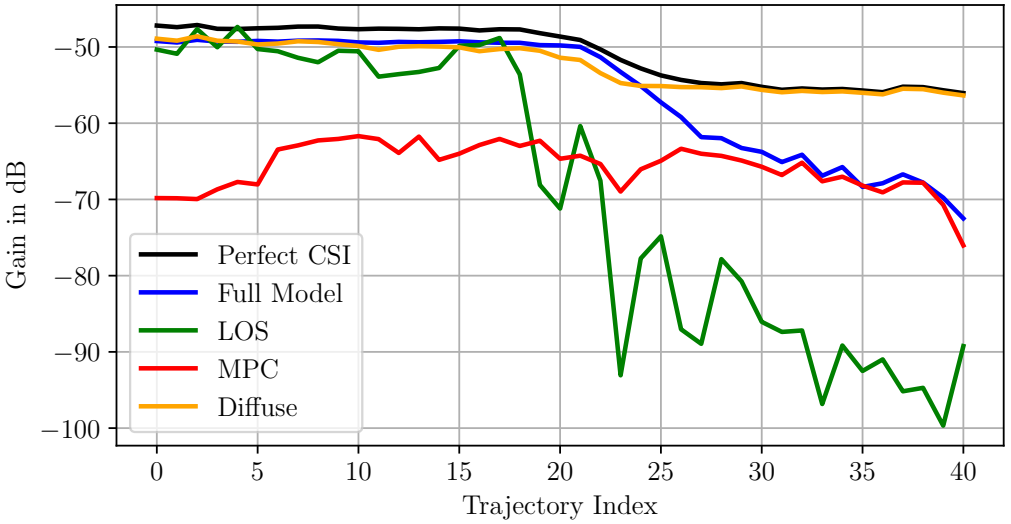

Figure 2.16: Performance comparison of MRT beamforming weights for various channel modeling approaches.

model of the radio system can be constructed, which contains information about both the physical line-of-sight component as well as the virtual multipath components. By leveraging the prediction and regression capabilities of an environment model, a channel model can be constructed and used for beamforming schemes.

Even though the specular reflection surfaces can be precisely modeled using massive MIMO, the amount of data which is needed quickly becomes infeasible. Compression schemes which allow for reduction in the data size and accurate reconstruction become essential. A Fourier-based approach which transforms the ”image” of the specularly reflecting surfaces into the frequency domain and only keeps the most meaningful components is able to highly reduce the burden on data storage while maintaining comparable performance with respect to uncompressed techniques. This is due to the low reconstruction errors which are possible for both magnitude and phase.

Extensions of the frequency domain representation of wall segments should be the focus of future work. A unified model which can store not only one single segment, but all previous channel state information and agent positions could yield higher predicting capabilities. For this, non uniform sampling of the environment could be leveraged to process the wall intersection coordinates which depending on the array layout and wall orientation do not lie on a regularly spaced grid.

Chapter 3

Signal processing for backscatter-based communication

There are several network infrastructure setups that can be used for backscatter communication (BC) with IoT nodes/EN devices. One of them is a bistatic setup where there is a need for high dynamic range and high-resolution ADCs at the reader side. In this chapter, we investigate a bistatic BC (BiBC) setup with RW panels.

In a BC setup, we have the following types of equipment: a carrier emitter (CE), a reader, and an END. In the BiBC setup, the CE and reader are spatially separated from each other, and therefore do not share radio frequency (RF) circuitry, which is beneficial for many reasons [22]. In BiBC, due to the double path-loss effect on the two-way backscatter link, the received backscattered signal is typically weak compared to the direct link interference (DLI) from a CE. This requires a high dynamic range of the circuitry in the reader: this dynamic range must be proportional to the signal strength ratio between the weak backscattered signal and the received signal from the direct link [23]. As a result, a high-resolution ADC is required to detect the weak backscattered signal under heavy DLI; this is an important consideration as with multiple-antenna technology, ADCs are major power consumers [24]. Moreover, the backscattered signal is pushed to the last bits of ADC due to the DLI which causes a low signal-to-interference-plus-noise ratio (SINR) [23].

We propose a new transmission scheme that reduces the DLI, along with a detection algorithm for use at the reader. Our contributions can be summarized as follows:

- To address the high-resolution ADC/high dynamic range problem in a BiBC system, we propose a transmission scheme that suppresses the DLI by steering the transmission from the CE using beamforming.
- We analyze the effect of the proposed transmission scheme on the dynamic range under channel estimation errors.
- We derive an algorithm based on a generalized log-likelihood ratio test (GLRT) to detect the END symbol/presence in BiBC. We propose an iterative algorithm to estimate the unknown parameters in the GLRT.
- Using the derived GLRT detector, we analyze the performance of END symbol detection at the reader in a BiBC setup with multiple antennas.

3.1 Review of previous and related work

In this subsection, we survey the literature on interference suppression in monostatic, ambient, and bistatic BC systems, respectively.

Monostatic: In [25], the authors propose a front-end architecture for the reader to cancel the self interference (SI) in a full-duplex monostatic system. In [26], the authors cancel the SI using a directional coupler and an adjustable reflective modulator. The authors of [27] propose a method to cancel the SI using the regenerated transmitted signal at the reader. However, interference cancellation methods for monostatic BC (MoBC) are usually complex and have high power consumption. They cannot directly be implemented in a BiBC system: the structure of the problem is different, and has new elements, such as a carrier frequency offset between the CE and reader [28].

Ambient: Receive beamforming techniques to cancel the DLI are proposed for ambient BC (AmBC) with a single-antenna transmitter setup in [29] and [30]. However, in [29], the authors only provide the solution for a parametric channel model, and in [30], DLI is canceled after the ADCs in the reader, which requires the use of high-resolution ADCs. In [31], a multi-antenna receiver operating without digital computation is proposed to decode the backscattered signal by separating the DLI from the received signal. In [32] and [33], the authors avoid the DLI by shifting the carrier frequency of the incident signal in a END in AmBC. However, the use of different frequency bands can reduce the spectral efficiency, and increase the power consumption and complexity at the END. In [34] and [35], the authors propose methods to avoid DLI in OFDM AmBC systems using null subcarriers [34] and cyclic prefixes [35]. However, in [35], the interference is canceled after the ADC which does not solve the dynamic range problem.

Bistatic: The authors of [23] investigate the coverage region for IoT communication, and the effect of the DLI on the dynamic range in the BiBC and AmBC systems. They show that the high dynamic range limits the system performance. In [36] and [37], the carrier frequency of the reflected signal is changed at the END to solve the DLI problem in a SISO BiBC system. In [28], the authors apply Miller coding at the END and exploit the periodicity of the carrier signal to mitigate the DLI in a SISO BiBC system. However, the proposed method cancels the interference after the ADC which does not address the high-resolution ADC/high dynamic range problem.

3.2 Proposed transmission scheme

In this section, we present a model of our bistatic communication system. We also describe our proposed transmission scheme, consisting of two phases: the channel estimation phase and the END symbol detection phase.

3.2.1 System model

Fig. 3.1 gives an overview of the system. CSP A with M antennas is the carrier emitter, CSP B with N antennas is the reader, and END C has a single antenna. The END can change its antenna reflection coefficient by varying the impedance of the load connected to the antenna in order to modulate the backscattered signal. Additionally, CSP A and CSP B can be a part of a larger distributed MIMO setup with several panels [38], and perform regular uplink/downlink communication, positioning, and sensing in addition to BC. Note, however, that if the distributed MIMO system operates in time division multiplexing (TDD) mode (the default assumption, for

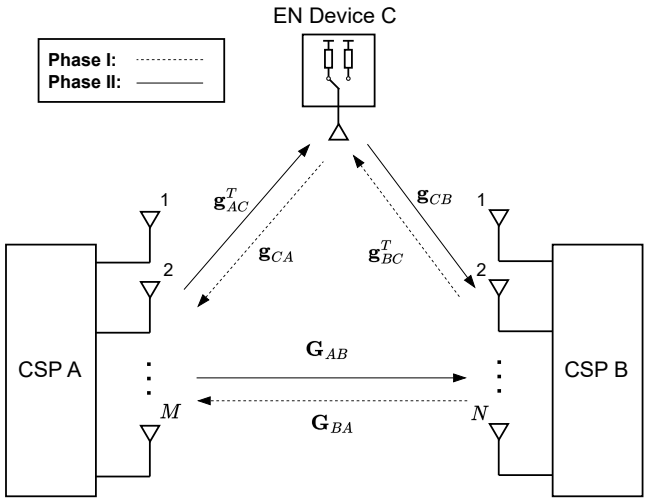

Figure 3.1: Model of the multiantenna BiBC system.

example, in [39]), then when communicating with the END, one of the panels must switch to reception mode while the other panel is transmitting. In this respect, the interaction with the END breaks the TDD flow.

Our aim is to decrease the required dynamic range of the reader, and detect the symbol/presence of the END. In Phase 1 (P1), we estimate the channel between CSP A and CSP B. In Phase 2 (P2), we construct a beamformer using a projection matrix that is designed based on the estimated channel. The proposed beamformer decreases the dynamic range and increases the detection performance by suppressing the interference due to the direct link CSP A $\rightarrow$ CSP B. [1]

In Fig. 3.1, $\mathbf{g}_{AC}^{\mathsf{T}}, \mathbf{g}_{CA}, \mathbf{g}_{CB}, \mathbf{g}_{BC}^{\mathsf{T}}, \mathbf{G}_{AB}$, and $\mathbf{G}_{BA}$ stand for the channels from CSP A to END, END to CSP A, END to CSP B, CSP B to END, CSP A to CSP B, and CSP B to CSP A, respectively. Note that, channels are the effective baseband channels between the units, and not the wireless propagation channels. This is because, in its most general form, channels account for 1) wireless propagation effects, 2) (non-reciprocal) transceiver effects, and 3) calibration effects. In this work, we have assumed that CSP A and CSP B are jointly reciprocity-calibrated such that $\mathbf{G}_{AB} = \mathbf{G}_{BA}^{\mathsf{T}}$. Here, the dimensions of $\mathbf{g}_{AC}, \mathbf{g}_{CA}, \mathbf{g}_{CB}, \mathbf{g}_{BC}$, and $\mathbf{G}_{AB}$ are $M \times 1, M \times 1, N \times 1, N \times 1$, and $N \times M$, respectively. It is assumed that all channels are time-invariant during P1 and P2.

3.2.2 Transmission scheme

In Fig. 3.2, the proposed transmission scheme of our bistatic communication setup is illustrated. There are two phases, as explained below.

3.2.2.1 Phase 1: Channel estimation at CSP A

The first phase comprises J_p slots ($\tau_p J_p$ symbols). In each slot, CSP B sends N orthogonal pilot signals one per antenna, which each has τ_p symbols, in order to facilitate estimation of $\mathbf{G}_{BA}$ at CSP A. The orthogonal pilot signals sent in a slot can be written in matrix form as $\mathbf{\Phi} \in \mathbb{C}^{N \times \tau_p}$

[1] Note that our proposed interference suppression algorithm for BiBC uses beamforming in the CE, relying on explicit channel state information between the CE and the reader. This is feasible for the assumed BiBC setup, but it would not be possible for AmBC as there is no dedicated CE in AmBC.

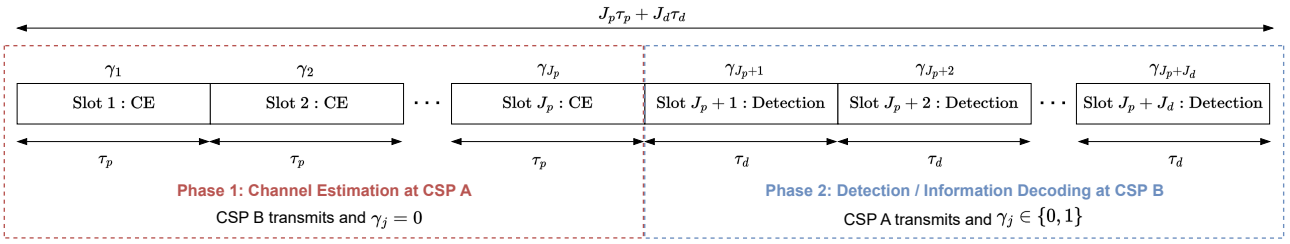

Figure 3.2: The proposed transmission scheme.

and satisfy

$$\mathbf{\Phi}\mathbf{\Phi}^{\mathsf{H}} = \alpha_p \mathbf{I}_N, \tag{3.1}$$

where $\alpha_p = \frac{p_t \tau_p}{N}$, $\tau_p \geq N$, and p_t stands for the transmit power. The total transmitted energy during P1 is

$$E_p \triangleq J_p ||\mathbf{\Phi}||^2 = J_p p_t \tau_p. \tag{3.2}$$

In Fig. 3.2, $\gamma_j \in \{0,1\}$ denotes the reflection coefficient. In P1, we select $\gamma_j = 0$ for $j \in \mathcal{S}_p = \{1, 2, \ldots, J_p\}$, i.e., the END is silent in each slot. When the END is silent, its reflection coefficient is a part of $\mathbf{G}_{BA}$ like other scattering objects in the environment. (It is also possible to design a END that absorbs the incoming signal for energy harvesting during $\gamma_j = 0$ [40]; that, however, would not make a difference to our proposed algorithms.) When $\gamma_j = 1$, the relative difference in the channel as compared to when $\gamma_j = 0$ from CSP B to CSP A is $\mathbf{g}_{CA}\mathbf{g}_{BC}^{\mathsf{T}}$. Alternating between two different values of γ_j corresponds to on-off keying modulation with two states, which is commonly used also in much other literature, for example [30], [40], [41].

3.2.2.2 Phase 2: Detection at CSP B

The second phase consists of J_d slots ($\tau_d J_d$ symbols). In each slot, CSP A sends a probing signal to detect the symbol of the END at CSP B. The probing signal sent in a slot can be represented in matrix form as $\mathbf{\Psi} \in \mathbb{C}^{M \times \tau_d}$ and satisfy

$$\mathbf{\Psi}\mathbf{\Psi}^{\mathsf{H}} = \alpha_d \mathbf{I}_M, \tag{3.3}$$

where $\alpha_d = \frac{p_t \tau_d}{M}$ and $\tau_d \geq M$.

The received signal of dimension $N \times \tau_d$ at CSP B, in slot j can be written as:

$$\mathbf{Y}_j = \mathbf{G}_{AB}\mathbf{P}_s\mathbf{\Psi} + \gamma_j \mathbf{g}_{CB}\mathbf{g}_{AC}^{\mathsf{T}}\mathbf{P}_s\mathbf{\Psi} + \mathbf{W}_j, \tag{3.4}$$

where $j \in \mathcal{S}_d = \{J_p + 1, J_p + 2, \ldots, J_p + J_d\}$ and $J_p + J_d = J$. Similar to in P1, when the END is silent ($\gamma_j = 0$), its contribution to the propagation environment is considered to be included in $\mathbf{G}_{AB}$. Therefore, $\mathbf{g}_{CB}\mathbf{g}_{AC}^{\mathsf{T}}$ represents the *difference* in the channel from CSP A to CSP B when $\gamma_j = 1$ as compared to when $\gamma_j = 0$. Due to this fact and because of reciprocity of propagation, $\mathbf{G}_{AB} = \mathbf{G}_{BA}^{\mathsf{T}}$. We assume that all channels are time-invariant during the J slot durations, i.e., the coherence time of all the channels exceeds $J_p\tau_p + J_d\tau_d$ symbols. $\mathbf{P}_s \in \mathbb{C}^{M \times M}$ is a scaled projection matrix introduced in order to minimize the DLI between CSP A and CSP B; the design principles for it will be explained in Section 3.3. $\mathbf{W}_j \in \mathbb{C}^{N \times \tau_d}$ comprises additive Gaussian noise; all elements of $\mathbf{W}_j$ are independent and identically distributed (i.i.d.) $\mathcal{CN}(0,1)$. Depending on a pre-determined pattern associated with the END, in some slots of P2, $\gamma_j = 0$, and in the remaining slots $\gamma_j = 1$. $\mathcal{S}_d$ is a set of $\{J_p + 1, \ldots, J\}$, and $\mathcal{S}_d^0$ and $\mathcal{S}_d^1$, which are subsets of $\mathcal{S}_d$,

Table 3.1: Summary of notation

Parameter	Notation	Dimension
Received signal at CSP B	$\mathbf{Y}_j$	$N \times \tau_d$
Received signal at CSP A	$\mathbf{Y}_j^p$	$M \times \tau_p$
Channel from CSP A to CSP B	$\mathbf{G}_{AB}$	$N \times M$
Channel from CSP B to CSP A	$\mathbf{G}_{BA}$	$M \times N$
Channel from CSP A to END	$\mathbf{g}_{AC}^{\mathsf{T}}$	$1 \times M$
Channel from END to CSP A	$\mathbf{g}_{CA}$	$M \times 1$
Channel from END to CSP B	$\mathbf{g}_{CB}$	$N \times 1$
Channel from CSP B to END	$\mathbf{g}_{BC}^{\mathsf{T}}$	$1 \times N$
Scaled projection matrix	$\mathbf{P}_s$	$M \times M$
Probing signal	$\mathbf{\Psi}$	$M \times \tau_d$
Additive Gaussian noise at CSP B	$\mathbf{W}_j$	$N \times \tau_d$
Additive Gaussian noise at CSP A	$\mathbf{W}_j^p$	$M \times \tau_p$
Pilot signal	$\mathbf{\Phi}$	$N \times \tau_p$
Reflection coefficient at END	γ_j	1×1
Cardinalities: $\lvert\mathcal{S}_p\rvert = J_p, \lvert\mathcal{S}_d\rvert = J_d, \lvert\mathcal{S}_d^0\rvert = J_d^0$, and $\lvert\mathcal{S}_d^1\rvert = J_d^1$		

contain the indices for which $\gamma_j = 0$ and $\gamma_j = 1$ in P2, respectively. The cardinalities of $\mathcal{S}_d, \mathcal{S}_d^0$, and $\mathcal{S}_d^1$ are $|\mathcal{S}_d| = J_d, |\mathcal{S}_d^0| = J_d^0$ and $|\mathcal{S}_d^1| = J_d^1$, where $J_d = J_d^0 + J_d^1$. The dimensions of the quantities in the model are summarized in Table 3.1.

The next sections explain our proposed choice of the projector $\mathbf{P}_s$ to minimize DLI, and the detection algorithm to be used at the reader.

3.3 Proposed interference suppression algorithm

In this section, we first define the dynamic range in our system. Next, we present the channel estimation algorithm in P1 for the direct link between CSP B and CSP A. We then propose a novel algorithm based on the estimated direct link channel to mitigate the DLI at CSP B in P2. The proposed algorithm decreases the required dynamic range of the system, and increases the SINR and the detection performance. In practice, it also enables the use of low-resolution ADCs due to the decreased dynamic range.

3.3.1 Dynamic range

The dynamic range of an n-bit resolution ADC is $6.02n$ dB, and the quantization error of the ADC decreases exponentially with increasing n [42], [43]. A high-resolution ADC, which has low quantization error, is required to detect the weak backscatter signal under strong DLI. We also define the *dynamic range of the received signal* during P2 as [23], [44]

$$\zeta = E\left\{\frac{\|\mathbf{G}_{AB}\mathbf{P}_s\mathbf{\Psi}\|^2 + \left\|\mathbf{g}_{CB}\mathbf{g}_{AC}^{\mathsf{T}}\mathbf{P}_s\mathbf{\Psi}\right\|^2}{\left\|\mathbf{g}_{CB}\mathbf{g}_{AC}^{\mathsf{T}}\mathbf{P}_s\mathbf{\Psi}\right\|^2}\right\}, \tag{3.5}$$

where the matrix product $\mathbf{G}_{AB}\mathbf{P}_s\mathbf{\Psi}$ represents the DLI. In Eq. (3.5), ζ, the dynamic range of the received signal, is a good indicator of the required dynamic range of the reader circuitry. In this equation, the expectation is taken with respect to random channel estimation errors (which

affect $\mathbf{P}_s$); the channels here are considered fixed. Note that the received signal from the END is added to the numerator to satisfy $\zeta \geq 1$ (0 dB). When there is no projection, i.e., $\mathbf{P}_s = \mathbf{I}_M$, the dynamic range can be large: $\zeta \gg 1$. When $\zeta \gg 1$, we need high-resolution ADCs which are not energy and cost efficient. This is because, in this operating regime, the backscattered signal is pushed to the last bits of the ADC, and the low-resolution ADCs cannot distinguish the weak backscatter signal under strong DLI due to the high quantization error. The aim of the scaled projection matrix, $\mathbf{P}_s \in \mathbb{C}^{M\times M}$, is to project the transmitted signal in P2 onto the nullspace of the dominant directions of $\mathbf{G}_{AB}$ (or more exactly, an estimate of it); consequently, the received DLI decreases which reduces the dynamic range requirements on the reader circuitry. The design of the projection matrix is detailed in Section 3.3.3.

3.3.2 Channel estimation at CSP A

In this subsection, we present the algorithm to estimate the channel from CSP B to CSP A, $\mathbf{G}_{BA}$. In the channel estimation phase, CSP B sends the same pilot signal $\mathbf{\Phi}$ in each slot, that is, J_p times. At CSP A, the received pilot signal in slot j is given by

$$\mathbf{Y}_j^p = \mathbf{G}_{BA}\mathbf{\Phi} + \gamma_j \mathbf{g}_{CA}\mathbf{g}_{BC}^{\mathsf{T}}\mathbf{\Phi} + \mathbf{W}_j^p, \tag{3.6}$$

where $j = 1, 2, \ldots, J_p$ and $\mathbf{W}_j^p \in \mathbb{C}^{M\times\tau_p}$ comprises additive noise and all elements of $\mathbf{W}_j^p$ are i.i.d. $\mathcal{CN}(0,1)$. We select the reflection coefficients $\gamma_j = 0$ for $j = 1, 2, \ldots, J_p$, i.e., the END is silent. As a result, Eq. (3.6) simplifies to

$$\mathbf{Y}_j^p = \mathbf{G}_{BA}\mathbf{\Phi} + \mathbf{W}_j^p. \tag{3.7}$$

The channel $\mathbf{G}_{BA}$ is estimated by least-squares (LS) as follows:

$$\hat{\mathbf{G}}_{BA} = \frac{1}{J_p}\sum_{j=1}^{J_p} \mathbf{Y}_j^p \mathbf{\Phi}^{\mathsf{H}}(\mathbf{\Phi}\mathbf{\Phi}^{\mathsf{H}})^{-1}. \tag{3.8}$$

Due to the reciprocity, the channel $\mathbf{G}_{AB}$ is simply $\mathbf{G}_{AB} = \mathbf{G}_{BA}^{\mathsf{T}}$; the same holds for their estimates: $\hat{\mathbf{G}}_{AB} = \hat{\mathbf{G}}_{BA}^{\mathsf{T}}$.

The singular value decomposition (SVD) of $\hat{\mathbf{G}}_{AB}$ can be written as

$$\hat{\mathbf{G}}_{AB} = \mathbf{U}\mathbf{\Delta}\mathbf{V}^{\mathrm{H}}, \tag{3.9}$$

where $\mathbf{U} \in \mathbb{C}^{N\times K_0}$ and $\mathbf{V} \in \mathbb{C}^{M\times K_0}$ are semi-unitary matrices, and $K_0 \leq \min\{M, N\}$ is the rank of $\hat{\mathbf{G}}_{AB}$. $\mathbf{\Delta}$ is a $K_0 \times K_0$ diagonal matrix with positive diagonal elements ordered in decreasing order.

3.3.3 Interference suppression algorithm

This subsection explains our proposed design of the projector, $\mathbf{P}_s$, whose application at CSP A will reduce the DLI and consequently improve the detection performance at CSP B.[2]

In P2, CSP A transmits a probing signal to enable CSP B to detect the symbol of the END. The probing signal, $\mathbf{\Psi}$, satisfies $\mathbf{\Psi}\mathbf{\Psi}^{\mathsf{H}} = \alpha_d \mathbf{I}_M$. Before transmitting $\mathbf{\Psi}$, CSP A first designs a

[2]Since the location of the END is unknown, we focus on the suppression of DLI, and we do not attempt to beamform power towards the END in order to increase the backscattered power.

projection matrix based on the channel estimates obtained in P1. After that, CSP A projects the probing signal onto the nullspace of $\hat{\mathbf{G}}_{AB}$ in order to minimize the CSP A $\rightarrow$ CSP B DLI, decrease the dynamic range, and increase the detection probability of END symbol at CSP B. After the projection, CSP A transmits the following signal

$$\mathbf{P}_s\mathbf{\Psi} = \Lambda\mathbf{P}\mathbf{\Psi}, \tag{3.10}$$

where $\mathbf{P}$ is an orthogonal projection of dimension $M \times M$ and rank $M - K$, with K to be appropriately selected, and

$$\Lambda = \sqrt{\frac{M}{M-K}} \tag{3.11}$$

is the non-zero eigenvalue of $\mathbf{P}_s = \Lambda\mathbf{P}$. In Eq. (3.10), Λ is used to keep the total radiated energy the same as without the projector, that is,

$$E_d \triangleq J_d||\mathbf{\Psi}||^2 = J_d||\mathbf{P}_s\mathbf{\Psi}||^2. \tag{3.12}$$

We select $\mathbf{P}$ to project onto the orthogonal complement of the space spanned by the columns of $\mathbf{V}_K$:

$$\mathbf{P} = \mathbf{I} - \mathbf{V}_K\mathbf{V}_K^{\mathrm{H}}, \tag{3.13}$$

where $\mathbf{V}_K$ contains the first K columns of $\mathbf{V}$ in Eq. (3.9). The choice of the value of K depends on several parameters, such as the number of antennas on the panels, the panel shapes (e.g., uniform linear arrays and rectangular linear arrays), the SNR, and the channel model. For instance, when there are a strong LoS link and SMC, setting K to 1 makes it possible to cancel the LoS link and decrease the dynamic range. As K increases, the dynamic range continues to decrease by the cancellation of SMCs, but the coverage area also decreases due to the increasing nulls in the antenna radiation pattern. Clearly, we must have $K \leq M$. Selecting an appropriate value of K is critical, and it could be chosen based on a predetermined dynamic range requirement and/or the number of dominant singular values of $\mathbf{G}_{AB}$ (or more exactly, an estimate of it).

Note that the location of the END is unknown. To avoid reducing the backscatter link power, $\mathbf{g}_{CB}\mathbf{g}_{AC}^{\mathsf{T}}$ should not lie in the subspace spanned by the dominant right singular vectors of $\mathbf{G}_{AB}$. For example, when $\mathrm{rank}(\mathbf{G}_{AB}) = 1$ in line-of-sight conditions, the proposed algorithm requires that the CE, END, and reader should not be located on a line, i.e., $\mathbf{g}_{CB}\mathbf{g}_{AC}^{\mathsf{T}} \neq \rho\mathbf{G}_{AB}$ for all $\rho \in \mathbb{C}$.

In summary, the received signals during both phases are given by

$$\begin{aligned}
&\mathbf{Y}_j^p = \mathbf{G}_{BA}\mathbf{\Phi} + \mathbf{W}_j^p, j \in \{1, \ldots, J_p\} \\
&\mathbf{Y}_j = \mathbf{G}_{AB}\mathbf{P}_s\mathbf{\Psi} + \gamma_j\mathbf{g}_{CB}\mathbf{g}_{AC}^{\mathsf{T}}\mathbf{P}_s\mathbf{\Psi} + \mathbf{W}_j, j \in \{J_p + 1, \ldots, J\}
\end{aligned} \tag{3.14}$$

3.4 A detector design without perfect CSI

In this section, we formalize the problem of detection during P2 as a hypothesis test, and develop a GLRT approach towards computing this test. The hypothesis test models the two scenarios absence and presence, respectively, of the END as $\mathcal{H}_0$ and $\mathcal{H}_1$. Specifically the test is:

$$\begin{aligned}
\mathcal{H}_0 : &\begin{cases} \mathbf{Y}_j = \mathbf{G}_{AB}\mathbf{P}_s\mathbf{\Psi} + \mathbf{W}_j, & j \in \mathcal{S}_d \\ \mathbf{Y}_j^p = \mathbf{G}_{BA}\mathbf{\Phi} + \mathbf{W}_j^p, & j \in \mathcal{S}_p \end{cases} \\
\mathcal{H}_1 : &\begin{cases} \mathbf{Y}_j = \mathbf{G}_{AB}\mathbf{P}_s\mathbf{\Psi} + \gamma_j\mathbf{g}_{CB}\mathbf{g}_{AC}^{\mathsf{T}}\mathbf{P}_s\mathbf{\Psi} + \mathbf{W}_j, & j \in \mathcal{S}_d \\ \mathbf{Y}_j^p = \mathbf{G}_{BA}\mathbf{\Phi} + \mathbf{W}_j^p, & j \in \mathcal{S}_p. \end{cases}
\end{aligned} \tag{3.15}$$

$$\frac{\max\limits_{\mathbf{G}_{AB},\mathbf{H}_{BL}} \left(\prod\limits_{j\in\mathcal{S}_p} p\left(\mathbf{Y}_j^p \mid \mathbf{G}_{BA}\right) \prod\limits_{j\in\mathcal{S}_d} p\left(\mathbf{Y}_j \mid \mathcal{H}_1, \mathbf{G}_{AB}, \mathbf{H}_{BL}, \gamma_j\right) \right)}{\max\limits_{\mathbf{G}_{AB}} \left(\prod\limits_{j\in\mathcal{S}_p} p\left(\mathbf{Y}_j^p \mid \mathbf{G}_{BA}\right) \prod\limits_{j\in\mathcal{S}_d} p\left(\mathbf{Y}_j \mid \mathcal{H}_0, \mathbf{G}_{AB}\right) \right)} \underset{\mathcal{H}_0}{\overset{\mathcal{H}_1}{\gtrless}} \eta. \tag{3.16}$$

Under $\mathcal{H}_1$, the END varies its antenna reflection coefficient γ_j according to a known (and pre-determined) pattern. Note that to detect the presence of the END, we detect a pre-determined sequence of symbols from it. Therefore, technically, the problems of symbol detection and presence detection are equivalent. Furthermore, this hypothesis test can be interpreted as detecting the END data, where the null hypothesis $\mathcal{H}_0$ corresponds to bit "0", and the alternative hypothesis $\mathcal{H}_1$ corresponds to bit "1".

We consider the standard distributed MIMO setup, with a backhaul link between the access points [45, p. 32], [38]. CSP A and CSP B can be any two antenna panels/access points in such a system. For this setup, we can assume that panels can share information, and also receive data over a backhaul network. Therefore, we assume that $\mathbf{\Psi}$, $\mathbf{\Phi}$, $\mathbf{P}_s$, and $\mathbf{Y}_j^p$ are known at CSP B. The only information that needs to be sent through the backhaul network on a slot-by-slot timescale is $\mathbf{P}_s$ and $\mathbf{Y}_j^p$. We also assume that $\mathbf{G}_{AB}$, $\mathbf{g}_{CB}$, and $\mathbf{g}_{AC}$ are unknown by the receiver.

The GLRT, using the received signals in P1 and P2, to detect the symbol/presence of the END is given in Eq. (3.16). In Eq. (3.16), $p\left(\mathbf{Y}_j^p \mid \mathbf{G}_{BA}\right)$, $p\left(\mathbf{Y}_j \mid \mathcal{H}_0, \mathbf{G}_{AB}\right)$, and $p\left(\mathbf{Y}_j \mid \mathcal{H}_1, \mathbf{G}_{AB}, \mathbf{H}_{BL}, \gamma_j\right)$ denote the likelihood functions of the observations in P1, and under $\mathcal{H}_0$ and $\mathcal{H}_1$ in P2, respectively; they are given as follows:

$$p\left(\mathbf{Y}_j^p \mid \mathbf{G}_{BA}\right) = \frac{1}{\pi^{M\tau_p}} \exp\left[-||\mathbf{Y}_j^p - \mathbf{G}_{BA}\mathbf{\Phi}||^2\right], \tag{3.17a}$$

$$p\left(\mathbf{Y}_j \mid \mathcal{H}_0, \mathbf{G}_{AB}\right) = \frac{1}{\pi^{N\tau_d}} \exp\left[-||\mathbf{Y}_j - \mathbf{G}_{AB}\mathbf{P}_s\mathbf{\Psi}||^2\right], \tag{3.17b}$$

$$p\left(\mathbf{Y}_j \mid \mathcal{H}_1, \mathbf{G}_{AB}, \mathbf{H}_{BL}, \gamma_j\right) = \frac{1}{\pi^{N\tau_d}} \exp\left[-||\mathbf{Y}_j - \mathbf{G}_{AB}\mathbf{P}_s\mathbf{\Psi} - \gamma_j\mathbf{g}_{CB}\mathbf{g}_{AC}^{\mathsf{T}}\mathbf{P}_s\mathbf{\Psi}||^2\right]. \tag{3.17c}$$

The detection threshold is η, and

$$\mathbf{H}_{BL} = \mathbf{g}_{CB}\mathbf{g}_{AC}^{\mathsf{T}}\mathbf{P}_s \tag{3.18}$$

is an $N \times M$ rank-1 matrix, where $\mathbf{g}_{CB}\mathbf{g}_{AC}^{\mathsf{T}}$ stands for the backscatter link cascade channel.

The next subsections develop the estimate of $\mathbf{G}_{AB}$ that maximizes the denominator of the the left hand side of Eq. (3.16), assuming $\mathcal{H}_0$ is true, and the estimates of $\mathbf{G}_{AB}$ and $\mathbf{H}_{BL}$ that maximize the numerator in Eq. (3.16), assuming $\mathcal{H}_1$ is true.

3.4.1 Estimation of unknown parameters under $\mathcal{H}_0$

Under $\mathcal{H}_0$, $\mathbf{G}_{AB}$ is the only unknown parameter. We estimate $\mathbf{G}_{AB}$, that maximizes the denominator in Eq. (3.16), using the received signals in P1 and P2 as follows:

$$\hat{\mathbf{G}}_{AB} = \arg\max_{\mathbf{G}_{AB}} \prod_{j\in\mathcal{S}_p} p\left(\mathbf{Y}_j^p \mid \mathbf{G}_{BA}\right) \prod_{j\in\mathcal{S}_d} p\left(\mathbf{Y}_j \mid \mathcal{H}_0, \mathbf{G}_{AB}\right) \tag{3.19a}$$

$$= \arg\min_{\mathbf{G}_{AB}} \left(\sum_{j\in\mathcal{S}_p} ||\mathbf{Y}_j^p - \mathbf{G}_{BA}\mathbf{\Phi}||^2 + \sum_{j\in\mathcal{S}_d} ||\mathbf{Y}_j - \mathbf{G}_{AB}\mathbf{P}_s\mathbf{\Psi}||^2 \right) \tag{3.19b}$$

$$\overset{(a)}{=} \arg\min_{\mathbf{G}_{AB}} \left(\sum_{j\in\mathcal{S}_p} ||\mathbf{Y}_{1,j} - \sqrt{\alpha_p}\mathbf{G}_{AB}||^2 + \sum_{j\in\mathcal{S}_d} ||\mathbf{Y}_{2,j} - \sqrt{\alpha_d}\mathbf{G}_{AB}\mathbf{P}_s||^2 \right) \tag{3.19c}$$

$$\overset{(b)}{=} \arg\min_{\mathbf{G}_{AB}} \left(||\mathbf{Y}_{P1} - \sqrt{\alpha_p}\mathbf{G}_{AB}\boldsymbol{\Upsilon}_{J_p}||^2 + ||\mathbf{Y}_{P2} - \sqrt{\alpha_d}\mathbf{G}_{AB}\mathbf{P}_s\boldsymbol{\Upsilon}_{J_d}||^2 \right) \tag{3.19d}$$

$$= \arg\min_{\mathbf{G}_{AB}} \left(|| \begin{bmatrix} \mathbf{Y}_{P1} & \mathbf{Y}_{P2} \end{bmatrix} - \mathbf{G}_{AB} \begin{bmatrix} \sqrt{\alpha_p}\boldsymbol{\Upsilon}_{J_p} & \sqrt{\alpha_d}\mathbf{P}_s\boldsymbol{\Upsilon}_{J_d} \end{bmatrix} ||^2 \right) \tag{3.19e}$$

$$= \begin{bmatrix} \mathbf{Y}_{P1} & \mathbf{Y}_{P2} \end{bmatrix} \begin{bmatrix} \sqrt{\alpha_p}\boldsymbol{\Upsilon}_{J_p}^{\mathsf{T}} \\ \sqrt{\alpha_d}(\mathbf{P}_s\boldsymbol{\Upsilon}_{J_d})^{\mathsf{T}} \end{bmatrix} \left(\begin{bmatrix} \sqrt{\alpha_p}\boldsymbol{\Upsilon}_{J_p} & \sqrt{\alpha_d}\mathbf{P}_s\boldsymbol{\Upsilon}_{J_d} \end{bmatrix} \begin{bmatrix} \sqrt{\alpha_p}\boldsymbol{\Upsilon}_{J_p}^{\mathsf{T}} \\ \sqrt{\alpha_d}(\mathbf{P}_s\boldsymbol{\Upsilon}_{J_d})^{\mathsf{T}} \end{bmatrix} \right)^{-1} \tag{3.19f}$$

$$= \left(\sum_{j\in\mathcal{S}_p} \sqrt{\alpha_p}\mathbf{Y}_{1,j} + \sum_{j\in\mathcal{S}_d} \sqrt{\alpha_d}\mathbf{Y}_{2,j}\mathbf{P}_s \right) (\alpha_p J_p \mathbf{I}_M + \alpha_d J_d \mathbf{P}_s)^{-1} \tag{3.19g}$$

$$= \left(\sum_{j\in\mathcal{S}_p} \boldsymbol{\Phi}^*(\mathbf{Y}_j^p)^{\mathsf{T}} + \sum_{j\in\mathcal{S}_d} \mathbf{Y}_j\boldsymbol{\Psi}^{\mathsf{H}}\mathbf{P}_s \right) (\alpha_p J_p \mathbf{I}_M + \alpha_d J_d \mathbf{P}_s)^{-1}, \tag{3.19h}$$

where equality (a) is shown in Appendix B.1. In (3.19c), $\mathbf{Y}_{1,j} = \boldsymbol{\Phi}^*(\mathbf{Y}_j^p)^{\mathsf{T}}/\sqrt{\alpha_p}$ and $\mathbf{Y}_{2,j} = \mathbf{Y}_j\boldsymbol{\Psi}^{\mathsf{H}}/\sqrt{\alpha_d}$. In (b), the block matrices $\mathbf{Y}_{P1} \in \mathbb{C}^{N\times MJ_p}$ and $\mathbf{Y}_{P2} \in \mathbb{C}^{N\times MJ_d}$ are created by ordering $\mathbf{Y}_{1,j}$ and $\mathbf{Y}_{2,j}$ in increasing order based on the index j, respectively. The block matrices $\boldsymbol{\Upsilon}_{J_p} \in \mathbb{R}^{M\times MJ_p}$ and $\boldsymbol{\Upsilon}_{J_d} \in \mathbb{R}^{M\times MJ_d}$ are $\boldsymbol{\Upsilon}_{J_p} = [\mathbf{I}_M \cdots \mathbf{I}_M]$ and $\boldsymbol{\Upsilon}_{J_d} = [\mathbf{I}_M \cdots \mathbf{I}_M]$. In Eq. (3.19h), $(\alpha_p J_p \mathbf{I}_M + \alpha_d J_d \mathbf{P}_s)$ is invertible and positive definite.

3.4.2 Estimation of unknown parameters under $\mathcal{H}_1$

Under $\mathcal{H}_1$, $\mathbf{G}_{AB}$ and $\mathbf{g}_{CB}\mathbf{g}_{AC}^{\mathsf{T}}$ are the unknown parameters, but the estimate of $\mathbf{g}_{CB}\mathbf{g}_{AC}^{\mathsf{T}}$ is not unique when $\mathbf{P}_s$ is not a full-rank matrix. Therefore, instead, we find the estimate of $\mathbf{H}_{BL}$, which is unique.

We assume that reflection coefficients are known under $\mathcal{H}_1$. We propose a cyclic optimization algorithm to minimize the sum of the squared norms in Eqs. (3.17a) and (3.17c), and consequently to estimate $\mathbf{G}_{AB}$ and $\mathbf{H}_{BL}$. The algorithm consists of following steps:

- *Step 1:* First find an initial value by minimizing the objective function with respect to (w.r.t.) $\mathbf{G}_{AB}$ using the observations $\mathbf{Y}_j$ and $\mathbf{Y}_{j'}^p$, where $j \in \mathcal{S}_d^0$ and $j' \in \mathcal{S}_p$.
- *Step 2:* Next, minimize the objective function w.r.t. $\mathbf{H}_{BL}$ by using the estimated value of $\mathbf{G}_{AB}$ and the observations $\mathbf{Y}_j$, where $j \in \mathcal{S}_d^1$. As mentioned earlier, $\mathcal{S}_d^0$ and $\mathcal{S}_d^1$ denote the sets of reflection coefficient indices for which $\gamma_j = 0$ and $\gamma_j = 1$ in P2, respectively.
- *Step 3:* Estimate $\mathbf{G}_{AB}$ by using all observations and the estimated value of $\mathbf{H}_{BL}$.
- *Step 4:* Iterate Steps 2–3 until convergence.

The details of these steps are given below.

3.4.2.1 Step 1 - Initial estimation of $\mathbf{G}_{AB}$

The estimate of $\mathbf{G}_{AB}$ using the observations $\mathbf{Y}_j$ and $\mathbf{Y}_{j'}^p$, where $j \in \mathcal{S}_d^0$ and $j' \in \mathcal{S}_p$, is calculated (similar to Eq. (3.19) but with $\mathcal{S}_d^0$ in lieu of $\mathcal{S}_d$) as

$$\hat{\mathbf{G}}_{AB}^{\mathcal{H}_1} = \arg\min_{\mathbf{G}_{AB}} \left(\sum_{j\in\mathcal{S}_p} ||\mathbf{Y}_j^p - \mathbf{G}_{BA}\boldsymbol{\Phi}||^2 + \sum_{j\in\mathcal{S}_d^0} ||\mathbf{Y}_j - \mathbf{G}_{AB}\mathbf{P}_s\boldsymbol{\Psi} - \gamma_j\mathbf{H}_{BL}\boldsymbol{\Psi}||^2 \right) \tag{3.20a}$$

$$\overset{(a)}{=} \arg\min_{\mathbf{G}_{AB}} \left(\sum_{j \in \mathcal{S}_p} ||\mathbf{Y}_j^p - \mathbf{G}_{BA}\mathbf{\Phi}||^2 + \sum_{j \in \mathcal{S}_d^0} ||\mathbf{Y}_j - \mathbf{G}_{AB}\mathbf{P}_s\mathbf{\Psi}||^2 \right) \tag{3.20b}$$

$$= \left(\sum_{j \in \mathcal{S}_p} \mathbf{\Phi}^*(\mathbf{Y}_j^p)^{\mathsf{T}} + \sum_{j \in \mathcal{S}_d^0} \mathbf{Y}_j \mathbf{\Psi}^{\mathsf{H}} \mathbf{P}_s \right) (\alpha_p J_p \mathbf{I}_M + \alpha_d J_d^0 \mathbf{P}_s)^{-1}. \tag{3.20c}$$

In (a), we have $\gamma_j = 0$ for $j \in \mathcal{S}_d^0$.

3.4.2.2 Step 2 - Estimation of $\mathbf{H}_{BL}$

In this step, we minimize our objective function w.r.t. $\mathbf{H}_{BL}$ by using $\hat{\mathbf{G}}_{AB}^{\mathcal{H}_1}$ and the observations $\mathbf{Y}_j$, where $j \in \mathcal{S}_d^1$.

To estimate $\mathbf{H}_{BL}$, we apply the following steps. We first express the scaled projection matrix as

$$\mathbf{P}_s = \Lambda \mathbf{P} = \Lambda \mathbf{Q}\mathbf{Q}^{\mathsf{H}} \tag{3.21}$$

in terms of its eigenvalue decomposition, where $\Lambda = \sqrt{M/(M-K)}$ and $\mathbf{Q}$ is an $M \times (M-K)$ matrix that satisfies $\mathbf{Q}^{\mathsf{H}}\mathbf{Q} = \mathbf{I}$. Note that $\mathrm{rank}\,(\mathbf{P}_s) = M - K$. The minimization problem has two constraints: (1) $\mathbf{H}_{BL} = \Lambda \mathbf{g}_{CB}\mathbf{g}_{AC}^{\mathsf{T}}\mathbf{Q}\mathbf{Q}^{\mathsf{H}}$ is a rank-1 matrix, and (2) $\mathbf{H}_{BL}^{\mathsf{H}}$ lies in the orthogonal complement of $\mathbf{V}_{1,K}$, i.e., $\mathbf{H}_{BL}^{\mathsf{H}} \in \mathrm{C}(\mathbf{P})$. To deal with this problem, we first estimate $\mathbf{H}'_{BL} = \mathbf{g}_{CB}\mathbf{g}_{AC}^{\mathsf{T}}\mathbf{Q}$, which is an unconstrained rank-1 matrix, as follows:

$$\hat{\mathbf{H}}'_{BL} = \arg\min_{\mathbf{H}'_{BL}} \sum_{j \in \mathcal{S}_d^1} ||\mathbf{Y}_j - \hat{\mathbf{G}}_{AB}^{\mathcal{H}_1}\mathbf{P}_s\mathbf{\Psi} - \gamma_j \Lambda \mathbf{g}_{CB}\mathbf{g}_{AC}^{\mathsf{T}}\mathbf{P}\mathbf{\Psi}||^2 \tag{3.22a}$$

$$\overset{(a)}{=} \arg\min_{\mathbf{H}'_{BL}} ||\mathbf{Y}_{DL} - \Lambda \mathbf{g}_{CB}\mathbf{g}_{AC}^{\mathsf{T}}\mathbf{Q}\mathbf{Q}^{\mathsf{H}}\mathbf{D}||^2 \tag{3.22b}$$

$$= \arg\min_{\mathbf{H}'_{BL}} \left(||\mathbf{Y}_{DL}||^2 + ||\Lambda \mathbf{g}_{CB}\mathbf{g}_{AC}^{\mathsf{T}}\mathbf{Q}\mathbf{Q}^{\mathsf{H}}\mathbf{D}||^2 - 2\,\mathrm{Re}\{\mathrm{Tr}\{\Lambda \mathbf{D}^{\mathsf{H}}\mathbf{Q}\mathbf{Q}^{\mathsf{H}}\mathbf{g}_{AC}^*\mathbf{g}_{CB}^{\mathsf{H}}\mathbf{Y}_{DL}\}\}\right) \tag{3.22c}$$

$$= \arg\min_{\mathbf{H}'_{BL}} \left(\mathrm{Tr}\{\Lambda^2 \mathbf{g}_{CB}\mathbf{g}_{AC}^{\mathsf{T}}\mathbf{Q}\mathbf{Q}^{\mathsf{H}}\mathbf{D}\mathbf{D}^{\mathsf{H}}\mathbf{Q}\mathbf{Q}^{\mathsf{H}}\mathbf{g}_{AC}^*\mathbf{g}_{CB}^{\mathsf{H}}\} - 2\,\mathrm{Re}\{\mathrm{Tr}\{\Lambda \mathbf{Y}_{DL}\mathbf{D}^{\mathsf{H}}\mathbf{Q}\mathbf{Q}^{\mathsf{H}}\mathbf{g}_{AC}^*\mathbf{g}_{CB}^{\mathsf{H}}\}\}\right) \tag{3.22d}$$

$$= \arg\min_{\mathbf{H}'_{BL}} \left(J_d^1 \alpha_d \Lambda^2 ||\mathbf{g}_{CB}\mathbf{g}_{AC}^{\mathsf{T}}\mathbf{Q}||^2 - 2\,\mathrm{Re}\{\mathrm{Tr}\{\Lambda \mathbf{Y}_{DL}\mathbf{D}^{\mathsf{H}}\mathbf{Q}\mathbf{Q}^{\mathsf{H}}\mathbf{g}_{AC}^*\mathbf{g}_{CB}^{\mathsf{H}}\}\}\right) \tag{3.22e}$$

$$= \arg\min_{\mathbf{H}'_{BL}} \left\{ ||\mathbf{g}_{CB}\mathbf{g}_{AC}^{\mathsf{T}}\mathbf{Q}||^2 - \frac{2\,\mathrm{Re}\{\mathrm{Tr}\{\mathbf{Y}_{DL}\mathbf{D}^{\mathsf{H}}\mathbf{Q}\mathbf{Q}^{\mathsf{H}}\mathbf{g}_{AC}^*\mathbf{g}_{CB}^{\mathsf{H}}\}\}}{J_d^1 \alpha_d \Lambda} \right\} \tag{3.22f}$$

$$= \arg\min_{\mathbf{H}'_{BL}} \left\| \mathbf{g}_{CB}\mathbf{g}_{AC}^{\mathsf{T}}\mathbf{Q} - \frac{1}{J_d^1 \alpha_d \Lambda} \mathbf{Y}_{DL}\mathbf{D}^{\mathsf{H}}\mathbf{Q} \right\|^2. \tag{3.22g}$$

In (a), we have $\gamma_j = 1$ for $j \in \mathcal{S}_d^1$, and the block matrix $\mathbf{Y}_{DL}$ of dimension $N \times J_d^1 \tau_d$ is created by ordering $\{\mathbf{Y}_j - \hat{\mathbf{G}}_{AB}^{\mathcal{H}_1}\mathbf{P}_s\mathbf{\Psi}\}$ in increasing order based on the index j. $\mathbf{D}$ is an $M \times J_d^1 \tau_d$-dimensional block matrix of $\mathbf{\Psi}$s: $\mathbf{D} = [\mathbf{\Psi} \ldots \mathbf{\Psi}]$, where $\mathbf{D}\mathbf{D}^{\mathsf{H}} = J_d^1 \alpha_d \mathbf{I}_M$.

We look for the best rank-one fit, in the Frobenius-norm sense, in Eq. (3.22g). The solution is given by the first term of the SVD of $\frac{1}{J_d^1 \alpha_d \Lambda} \mathbf{Y}_{DL}\mathbf{D}^{\mathsf{H}}\mathbf{Q}$ [46]:

$$\hat{\mathbf{H}}'_{BL} = \mathbf{u}_1 \delta_1 \mathbf{v}_1^{\mathsf{H}}, \tag{3.23}$$

where $\mathbf{u}_1, \mathbf{v}_1$, and δ_1 are the dominant left singular vector, the dominant right singular vector, and the dominant singular value, respectively.

Algorithm 1: The estimate of $\mathbf{G}_{AB}$ and $\mathbf{H}_{BL}$ that maximize the numerator in the GLRT under $\mathcal{H}_1$.

Require: $\mathbf{Y}_j, \mathbf{Y}_j^p, \gamma_j, \mathbf{P}_s, \mathbf{\Psi}$

Ensure: $\hat{\mathbf{H}}_{BL}, \hat{\mathbf{G}}_{AB}^{\mathcal{H}_1}$

1: $\upsilon = 0$

2: Compute

$$\hat{\mathbf{G}}_{AB}^{\mathcal{H}_1}(\upsilon) = \left(\sum_{j \in \mathcal{S}_p} \mathbf{\Phi}^*(\mathbf{Y}_j^p)^{\mathsf{T}} + \sum_{j \in \mathcal{S}_d^0} \mathbf{Y}_j \mathbf{\Psi}^{\mathsf{H}} \mathbf{P}_s \right) (\alpha_p J_p \mathbf{I}_M + \alpha_d J_d^0 \mathbf{P}_s)^{-1}$$

3: Compute $\hat{\mathbf{H}}_{BL}(\upsilon) = \Lambda \mathbf{u}_1(\upsilon)\delta_1(\upsilon)\mathbf{v}_1^{\mathsf{H}}(\upsilon)\mathbf{Q}^{\mathsf{H}}$

4: **repeat**

5: Compute

$$\hat{\mathbf{G}}_{AB}^{\mathcal{H}_1}(\upsilon+1) = \left(\sum_{j \in \mathcal{S}_p} \mathbf{\Phi}^*(\mathbf{Y}_j^p)^{\mathsf{T}} + \sum_{j \in \mathcal{S}_d} (\mathbf{Y}_j - \gamma_j \hat{\mathbf{H}}_{BL}(\upsilon)\mathbf{\Psi})\mathbf{\Psi}^{\mathsf{H}} \mathbf{P}_s \right) (\alpha_p J_p \mathbf{I}_M + \alpha_d J_d \mathbf{P}_s)^{-1}.$$

6: Compute $\hat{\mathbf{H}}_{BL}(\upsilon+1) = \Lambda \mathbf{u}_1(\upsilon+1)\delta_1(\upsilon+1)\mathbf{v}_1^{\mathsf{H}}(\upsilon+1)\mathbf{Q}^{\mathsf{H}}$

7: $\upsilon = \upsilon + 1$

8: **until** $||\hat{\mathbf{G}}_{AB}^{\mathcal{H}_1}(\upsilon) - \hat{\mathbf{G}}_{AB}^{\mathcal{H}_1}(\upsilon-1)||^2 \leq \epsilon$

Using Eq. (3.23), the estimate of $\mathbf{H}_{BL}$ that maximizes the numerator in the GLRT is given by

$$\hat{\mathbf{H}}_{BL} = \Lambda \hat{\mathbf{H}}'_{BL} \mathbf{Q}^{\mathsf{H}} = \Lambda \mathbf{u}_1 \delta_1 \mathbf{v}_1^{\mathsf{H}} \mathbf{Q}^{\mathsf{H}}, \tag{3.24}$$

where $\hat{\mathbf{H}}_{BL}^{\mathsf{H}}$ lies in $\mathrm{C}(\mathbf{P})$ because the eigenvectors of the projection matrix, i.e., the columns of $\mathbf{Q}$, lie in $\mathrm{C}(\mathbf{P})$.

3.4.2.3 Step 3 - Estimation of $\mathbf{G}_{AB}$

In Eq. (3.20), the initial estimate of $\mathbf{G}_{AB}$ is calculated without using the observations $\mathbf{Y}_j$, where $j \in \mathcal{S}_d^1$. After the estimation of $\mathbf{H}_{BL}$ in step 2, we can use all observations to estimate $\mathbf{G}_{AB}$ (similar to Eq. (3.19)) as follows:

$$\hat{\mathbf{G}}_{AB}^{\mathcal{H}_1} = \left(\sum_{j \in \mathcal{S}_p} \mathbf{\Phi}^*(\mathbf{Y}_j^p)^{\mathsf{T}} + \sum_{j \in \mathcal{S}_d} (\mathbf{Y}_j - \gamma_j \hat{\mathbf{H}}_{BL}\mathbf{\Psi})\mathbf{\Psi}^{\mathsf{H}} \mathbf{P}_s \right) (\alpha_p J_p \mathbf{I}_M + \alpha_d J_d \mathbf{P}_s)^{-1}. \tag{3.25}$$

3.4.2.4 Step 4 - Iteration

Finally, we iteratively estimate $\mathbf{H}_{BL}$ and $\mathbf{G}_{AB}^{\mathcal{H}_1}$ by using Eqs. (3.24) and (3.25) until the Frobenius norm of the difference between two successive estimation of $\mathbf{G}_{AB}^{\mathcal{H}_1}$ is smaller than a threshold.

A summary of our proposed algorithm is given in Algorithm 1. [3]

3.4.3 Modified estimator for the non-jointly calibrated case

Throughout the above derivation, we have assumed that CSP A and CSP B are jointly reciprocity-calibrated such that $\mathbf{G}_{AB} = \mathbf{G}_{BA}^{\mathsf{T}}$. In practice, such calibration can be achieved by distribution of

[3] Note that, if we assume that the pilot signal is sent from CSP A to CSP B, instead of from CSP B to CSP A in P1, the computational complexity of Algorithm 1 will remain the same.

a phase reference over a cable that connects the two panels, or by bi-directional intra- and inter-panel over-the-air measurements [47]. However, if such calibration has not been performed, and the panels are only *individually* calibrated for reciprocity, there will be an unknown residual phase offset, say ϕ, between the panels such that $\mathbf{G}_{AB} = e^{j\phi}\mathbf{G}_{BA}^{\mathsf{T}}$. In this scenario, the projection matrix designed in Section 3.3.3 will cancel the DLI similar to when joint reciprocity calibration is assumed (since $e^{j\phi}$ is only a complex scalar); however, we cannot directly use the signal received in P1 together with the signals received in P2 for the detection of the END symbol. A simple remedy in this case is to base the detector on *only* the signals received during P2. The corresponding algorithm is worked out in Appendix B.2, and is principally different from Algorithm 1 developed above, as $\mathbf{G}_{AB}$ is unidentifiable (even in the noise-free case) when only data from P2 are available; see the appendix for details.[4]

3.4.4 Approximate GLRT detector

Since $\hat{\mathbf{G}}_{AB}^{\mathcal{H}_1}$ and $\hat{\mathbf{H}}_{BL}$ are not maximum-likelihood estimates, inserting the estimates of $\mathbf{G}_{AB}$ and $\mathbf{H}_{BL}$ obtained above, we obtain an approximation of the GLRT detector in Eq. (3.16). Specifically, the resulting (approximate) GLRT detector is given in Eq. (3.26).

$$GLR = \frac{\prod\limits_{j\in\mathcal{S}_p} p\left(\mathbf{Y}_j^p \mid \hat{\mathbf{G}}_{AB}^{\mathcal{H}_1}\right) \prod\limits_{j\in\mathcal{S}_d} p\left(\mathbf{Y}_j \mid \mathcal{H}_1, \hat{\mathbf{G}}_{AB}^{\mathcal{H}_1}, \hat{\mathbf{H}}_{BL}, \gamma_j\right)}{\prod\limits_{j\in\mathcal{S}_p} p\left(\mathbf{Y}_j^p \mid \hat{\mathbf{G}}_{AB}^{\mathcal{H}_0}\right) \prod\limits_{j\in\mathcal{S}_d} p\left(\mathbf{Y}_j \mid \mathcal{H}_0, \hat{\mathbf{G}}_{AB}^{\mathcal{H}_0}\right)} \underset{\mathcal{H}_0}{\overset{\mathcal{H}_1}{\gtrless}} \eta. \tag{3.26}$$

Defining $\mathbf{A}_j, \mathbf{B}, \mathbf{C}_1$, and $\mathbf{C}_2$ as follows,

$$\mathbf{A}_j = \hat{\mathbf{G}}_{AB}^{\mathcal{H}_1}\mathbf{P}_s\mathbf{\Psi} + \gamma_j\hat{\mathbf{H}}_{BL}\mathbf{\Psi}, \tag{3.27a}$$

$$\mathbf{B} = \hat{\mathbf{G}}_{AB}^{\mathcal{H}_0}\mathbf{P}_s\mathbf{\Psi}, \tag{3.27b}$$

$$\mathbf{C}_1 = (\hat{\mathbf{G}}_{AB}^{\mathcal{H}_1})^{\mathsf{T}}\mathbf{\Phi}, \tag{3.27c}$$

$$\mathbf{C}_2 = (\hat{\mathbf{G}}_{AB}^{\mathcal{H}_0})^{\mathsf{T}}\mathbf{\Phi}, \tag{3.27d}$$

we can write $\log(GLR)$ as

$$\begin{aligned}\log(GLR) = &-\sum_{j\in\mathcal{S}_d} ||\mathbf{Y}_j - \hat{\mathbf{G}}_{AB}^{\mathcal{H}_1}\mathbf{P}_s\mathbf{\Psi} - \gamma_j\hat{\mathbf{H}}_{BL}\mathbf{\Psi}||^2 + \sum_{j\in\mathcal{S}_d} ||\mathbf{Y}_j - \hat{\mathbf{G}}_{AB}^{\mathcal{H}_0}\mathbf{P}_s\mathbf{\Psi}||^2 \\ &- \sum_{j\in\mathcal{S}_p} ||\mathbf{Y}_j^p - (\hat{\mathbf{G}}_{AB}^{\mathcal{H}_1})^{\mathsf{T}}\mathbf{\Phi}||^2 + \sum_{j\in\mathcal{S}_p} ||\mathbf{Y}_j^p - (\hat{\mathbf{G}}_{AB}^{\mathcal{H}_0})^{\mathsf{T}}\mathbf{\Phi}||^2 \qquad (3.28a) \\ = &-\sum_{j\in\mathcal{S}_d} \mathrm{Tr}\{(\mathbf{Y}_j - \mathbf{A}_j)(\mathbf{Y}_j - \mathbf{A}_j)^{\mathsf{H}}\} + \sum_{j\in\mathcal{S}_d} \mathrm{Tr}\{(\mathbf{Y}_j - \mathbf{B})(\mathbf{Y}_j - \mathbf{B})^{\mathsf{H}}\} \\ &- \sum_{j\in\mathcal{S}_p} \mathrm{Tr}\{(\mathbf{Y}_j^p - \mathbf{C}_1)(\mathbf{Y}_j^p - \mathbf{C}_1)^{\mathsf{H}}\} + \sum_{j\in\mathcal{S}_p} \mathrm{Tr}\{(\mathbf{Y}_j^p - \mathbf{C}_2)(\mathbf{Y}_j^p - \mathbf{C}_2)^{\mathsf{H}}\} \qquad (3.28b) \\ = &\sum_{j\in\mathcal{S}_d} \left(2\,\mathrm{Re}\{\mathrm{Tr}\{\mathbf{Y}_j(\mathbf{A}_j - \mathbf{B})^{\mathsf{H}}\}\} - ||\mathbf{A}_j||^2 + ||\mathbf{B}||^2\right) \\ &+ \sum_{j\in\mathcal{S}_p} \left(2\,\mathrm{Re}\{\mathrm{Tr}\{\mathbf{Y}_j^p(\mathbf{C}_1 - \mathbf{C}_2)^{\mathsf{H}}\}\} - ||\mathbf{C}_1||^2 + ||\mathbf{C}_2||^2\right). \qquad (3.28c)\end{aligned}$$

[4] In addition, it is also possible to use the modified estimator to decrease the backhaul overhead in the case of limited backhaul link capacity because there is no need to send the received signal in P1 over the backhaul link.

Finally, we can write the hypothesis test as follows:

$$\sum_{j\in\mathcal{S}_d}\left(2\,\mathrm{Re}\{\mathrm{Tr}\{\mathbf{Y}_j(\mathbf{A}_j-\mathbf{B})^{\mathsf{H}}\}\}-||\mathbf{A}_j||^2+||\mathbf{B}||^2\right) + \sum_{j\in\mathcal{S}_p}\left(2\,\mathrm{Re}\{\mathrm{Tr}\{\mathbf{Y}_j^p(\mathbf{C}_1-\mathbf{C}_2)^{\mathsf{H}}\}\}-||\mathbf{C}_1||^2+||\mathbf{C}_2||^2\right)\underset{\mathcal{H}_0}{\overset{\mathcal{H}_1}{\gtrless}}\log(\eta). \tag{3.29}$$

3.5 Performance evaluation of the proposed detector

In this section, we first provide the simulation parameters and then discuss numerical results. We assume that there is a specular reflector that causes a SMC. The channels are modeled as

$$[\mathbf{G}_{AB}]_{n,m}=[\mathbf{G}_{BA}^{\mathsf{T}}]_{n,m}=\sqrt{\beta_{m,n}}e^{-j\frac{2\pi}{\lambda}d_{m,n}}+g_{SMC}\sqrt{\beta'_{m,n}}e^{-j\frac{2\pi}{\lambda}d'_{m,n}}, \tag{3.30a}$$

$$[\mathbf{g}_{AC}]_m=[\mathbf{g}_{CA}]_m=\sqrt{\beta_m}e^{-j\frac{2\pi}{\lambda}d_m}+g_{SMC}\sqrt{\beta'_m}e^{-j\frac{2\pi}{\lambda}d'_m}, \tag{3.30b}$$

$$[\mathbf{g}_{CB}]_n=[\mathbf{g}_{BC}]_n=\sqrt{\beta_n}e^{-j\frac{2\pi}{\lambda}d_n}+g_{SMC}\sqrt{\beta'_n}e^{-j\frac{2\pi}{\lambda}d'_n}, \tag{3.30c}$$

where $m\in\{1,2,\ldots,M\}$, $n\in\{1,2,\ldots,N\}$, g_{SMC} is the amplitude gain of the SMC, λ is the wavelength of the emitted signal, and $[\mathbf{G}_{AB}]_{n,m}$, $[\mathbf{g}_{AC}]_m$, and $[\mathbf{g}_{CB}]_n$ are the $(n,m)^{\text{th}}$ element of $\mathbf{G}_{AB}$, m^{th} element of $\mathbf{g}_{AC}$, and n^{th} element of $\mathbf{g}_{CB}$, respectively. The path-gain coefficients are defined as

$$\beta_{m,n}=\frac{1}{d_{m,n}^2},\beta'_{m,n}=\frac{1}{(d'_{m,n})^2}, \tag{3.31a}$$

$$\beta_m=\frac{1}{d_m^2},\beta'_m=\frac{1}{(d'_m)^2}, \tag{3.31b}$$

$$\beta_n=\frac{1}{d_n^2},\beta'_n=\frac{1}{(d'_n)^2}, \tag{3.31c}$$

where $d_{m,n},d_m$, and d_n stand for the LoS path lengths between the m^{th} antenna in CSP A - the n^{th} antenna in CSP B, the m^{th} antenna in CSP A - the END, and the n^{th} antenna in CSP B - the END, respectively. The non-LoS path lengths $d'_{m,n},d'_m$, and d'_n are defined similarly. We choose a uniform linear array at both CSP A and CSP B.

Unless otherwise stated, we use the following parameters: $J_d=2,\tau_d=16,J_p=1,\tau_p=16$, $M=16,N=16$, $\lambda=0.1$ m, and $d_{\text{ant}}=0.5$, where d_{ant} denotes the inter-antenna distance normalized by the carrier wavelength. We select the reflection coefficients at the END as $\gamma_j=0$ for $j\in\mathcal{S}_p$ in P1. In P2, $\gamma_j\in\{0,1\}$ for $j\in\mathcal{S}_d$, and we have the same number of $\gamma_j=0$ and $\gamma_j=1$, i.e., $|\mathcal{S}_d^0|=|\mathcal{S}_d^1|=J_d/2$. The SNR during the channel estimation phase is defined as $\text{SNR}_p=\bar{\beta}_{BA}p_tJ_p\tau_p$, where p_t is the transmit power and $\bar{\beta}_{BA}=\frac{\|\mathbf{G}_{AB}\|^2}{MN}$. The SNR during the detection of END symbol is $\text{SNR}_d=\bar{\beta}_{CB}\bar{\beta}_{AC}p_tJ_d\tau_d\bar{\gamma}$, where $\bar{\gamma}=0.5$ is the average value of the reflection coefficients in P2, and $\bar{\beta}_{AC}=\|\mathbf{g}_{AC}\|^2/M$ and $\bar{\beta}_{CB}=\|\mathbf{g}_{CB}\|^2/N$. The centers of CSP A and CSP B are located at positions with coordinates $(0,0)$ and $(6,0)$ in meters, respectively. The specular reflector is located along the x-axis at $y=-4$ m. Table 3.2 lists all simulation parameters.

In Figs. 3.3 and 3.4, we investigate the total radiated energy from CSP A during a slot duration in P2, which is given by

$$E_t(\theta)\triangleq||\mathbf{g}(\theta)^{\mathsf{T}}\mathbf{P}_s\Psi||^2=\frac{\alpha_dM}{M-K}||\mathbf{g}(\theta)^{\mathsf{T}}\mathbf{P}||^2, \tag{3.32}$$

Table 3.2: Simulation Parameters

Parameter	Value
Number of slots for the probing signal	$J_d = 2$
Number of symbols in each slot for the probing signal	$\tau_d = 16$
Number of slots for the pilot signal	$J_p = 1$
Number of symbols in each slot for the pilot signal	$\tau_p = 16$
Number of antennas in CSP A	$M = 8, 16$
Number of antennas in CSP B	$N = 8, 16$
Number of antennas in END	1
The location of CSP A, CSP B, and END in meters	$(0, 0), (6, 0)$, and $(3, y)$, where $y \in [0\ 30]$
The location of the specular reflector in meters	$y = -4$
The amplitude gain of the SMC	$g_{SMC} = 0.5$
Reflection coefficients at END	$\gamma_j = 0$ for $j \in \mathcal{S}_p$ and $\gamma_j \in \{0, 1\}$ for $j \in \mathcal{S}_d$
The wavelength of the emitted signal in meters	$\lambda = 0.1$
Inter-antenna distance both in CSP A and CSP B in meter	$d_{\text{ant}}\lambda = 0.5\lambda = 0.05$
SNR during the detection of END symbol	$\text{SNR}_d = 2$ dB
SNR during the channel estimation	$\text{SNR}_p = 5, 20$ dB

where $\mathbf{g}(\theta) \in \mathbb{C}^{M\times 1}$ is the steering vector defined as follows:

$$\mathbf{g}(\theta) = \begin{bmatrix} 1 \\ \exp\left(j2\pi d_{\text{ant}} \sin(\theta)\right) \\ \vdots \\ \exp\left(j(M-1)2\pi d_{\text{ant}} \sin(\theta)\right) \end{bmatrix}, \tag{3.33}$$

and θ is the angle of departure of the transmitted signal. We select $\text{SNR}_d = 2$ dB, and assume that $\bar{\beta}_{AC} = 1$ and $\bar{\beta}_{CB} = 1$. The projection matrix is designed based on PCSI, i.e., $\hat{\mathbf{G}}_{AB} = \mathbf{G}_{AB}$, by CSP A for all scenarios except the no-projection case, i.e., $\mathbf{P}_s = \mathbf{I}_M$. Note that the number of antennas in CSP A and CSP B does not affect the antenna radiation pattern for the no-projection case.

In Fig. 3.3, we compare the antenna radiation patterns for the three different cases: (1) $M = 8, N = 16$, (2) $M = 16, N = 16$, and (3) $M = 16, N = 8$. CSP B is located at 0°, and in the first and third cases, the singular values of $\mathbf{G}_{AB}$ are $(1.81, 0.59, 0.47, \dots)$, and we select $K = 2$. In the second case, the singular values of $\mathbf{G}_{AB}$ are $(2.33, 1.25, 0.79, 0.30, \dots)$, and we select $K = 3$. As shown in the figure, the direct link, which is the LoS link plus SMC, is canceled due to the use of $\mathbf{P}_s$ except for the no projection case. In addition, with increasing M, the beamforming accuracy and consequently the coverage area after projection increase in this particular setup.

In Fig. 3.4, we compare the antenna radiation patterns for varying values of K for $M = N = 16$. As seen in the figure, we can cancel more components of the direct link channel with increasing K. For example, the dominant directions of the LoS link are canceled for $K = 1$ and $K = 2$, and the dominant direction of the SMC is also canceled for $K = 3$. This is because the first two dominant right singular vectors of $\mathbf{G}_{AB}$ are mostly associated with the LoS link, while the third dominant right singular vector is mostly associated with the SMC. Note that the dominant K right singular vectors of $\mathbf{G}_{AB}$ are used for designing the projection matrix.

In Fig. 3.5, we show the ratio ζ given in Eq. (3.5) for different END locations to investigate the change in the dynamic range in P2 for varying K and SNR_p values. The END is located at $(3, y)$, where we change the vertical position of the END, y, between 0 and 30 meters. For the perfect-

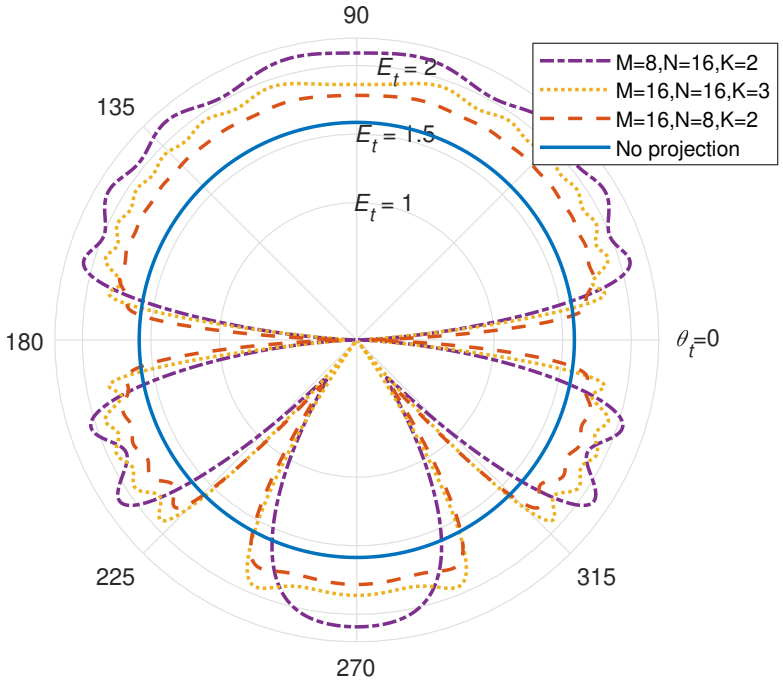

Figure 3.3: The 2-D antenna radiation patterns for the different number of antennas.

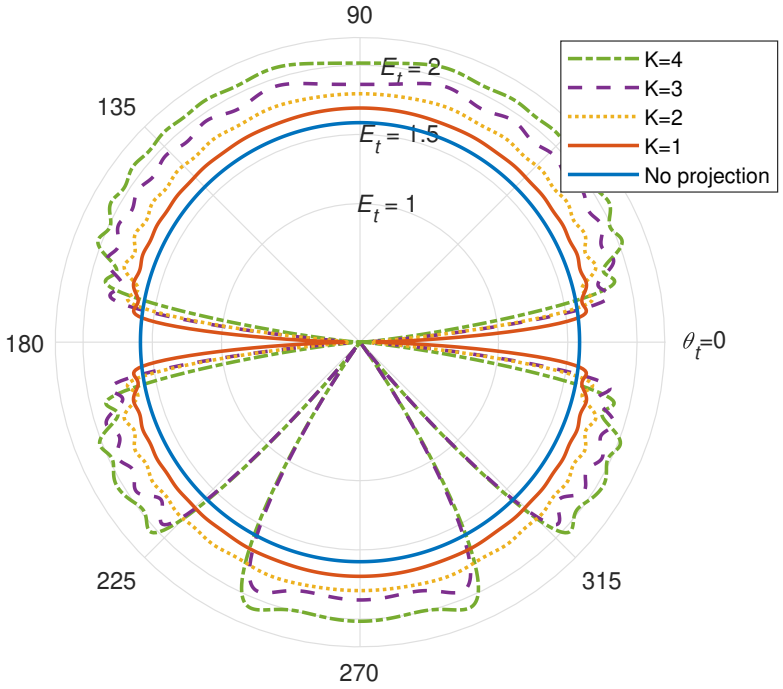

Figure 3.4: The 2-D antenna radiation patterns for the different K values $(M = 16, N = 16)$.

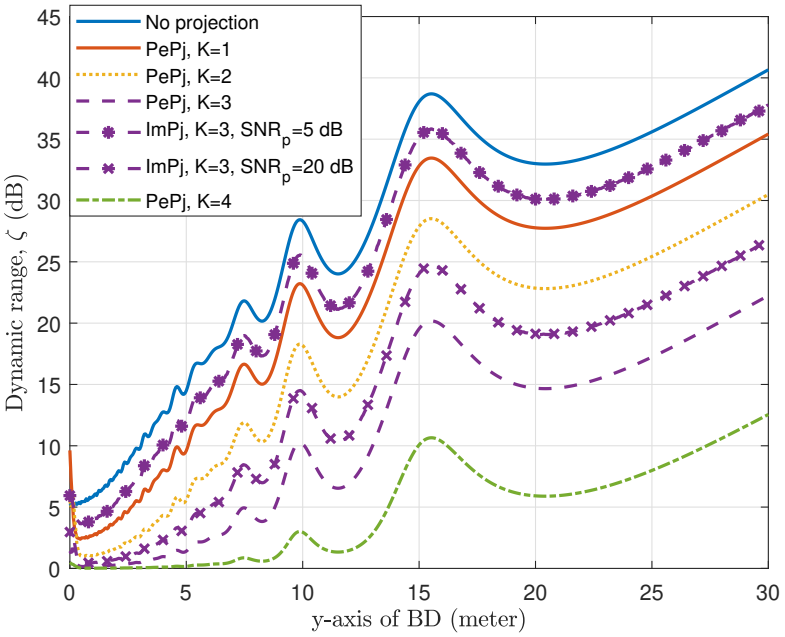

Figure 3.5: The dynamic range of the received signal.

projection (PePj) case, we assume that $\hat{\mathbf{G}}_{AB} = \mathbf{G}_{AB}$, for the no-projection case, $\mathbf{P}_s = \mathbf{I}_M$, and for the imperfect-projection (ImPj) case, we design $\mathbf{P}_s$ based on $\hat{\mathbf{G}}_{AB}$.

As seen in Fig. 3.5, for $y = 0$, the projection matrix cannot affect the dynamic range as intended since the END is located on the broadside direction of the CSP A. However, the dynamic range, ζ, decreases with increasing K when $y > 0$ because we can cancel more components of the direct link channel. For example, at $y = 10$ m, ζ is 28.32 dB, 23.10 dB, 18.18 dB, 10.14 dB, and 2.94 dB for the no projection, $K = 1$, $K = 2$, $K = 3$ (PePj), and $K = 4$ cases, respectively. For $y < 23$ m, there are fluctuations in the dynamic range curves due to the constructive and destructive interference between the LoS link and the SMC. However, after about 23 m, $d'_m \approx d_m + c_1$ and $d'_n \approx d_n + c_2$, and consequently $[\mathbf{g}_{CB}]_n \approx c_3 e^{-j\frac{2\pi}{\lambda}d_n}$ and $[\mathbf{g}_{AC}]_n \approx c_4 e^{-j\frac{2\pi}{\lambda}d_m}$, where $c_1, \ldots, c_4$ are some constants. As a result, the channels $\mathbf{g}_{CB}$ and $\mathbf{g}_{AC}$ behave like a LoS channel without multipath. Therefore, the dynamic range curves are smoother beyond $y = 23$ m for this particular setup.

In Fig. 3.5, we also show the effect of the imperfect projection on the dynamic range for $K = 3$. As seen from the figure, the dynamic range, ζ, decreases with increasing SNR$_p$ when $y > 0$. For example, at $y = 10$ m, ζ is 25.39 dB at SNR$_p = 5$ dB and 14.38 dB at SNR$_p = 20$ dB. This is because the projection matrix designed with high SNR$_p$ values has a better capability to decrease the DLI. In practice, with a decreased dynamic range, it is possible to use low-resolution ADCs which are more cost and energy efficient than high-resolution ADCs.

In Fig. 3.6, simulation results for the hypothesis test in Eq. (3.15) are shown. We use the GLRT detector in Eq. (3.29). A triangular setup is used with the END located at $(3, 3)$ meters. We consider three different scenarios: (1) perfect projection, i.e., $\mathbf{P}_s$ is designed based on $\hat{\mathbf{G}}_{AB} = \mathbf{G}_{AB}$, (2) imperfect projection, i.e., $\mathbf{P}_s$ is designed based on the estimated channel, and (3) no projection, i.e., $\mathbf{P}_s = \mathbf{I}_M$. In all scenarios, we select $K = 3$, SNR$_d = 2$ dB, and we use two different SNR$_p$ values as 5 dB and 20 dB in P1 to investigate the effect of the scaled projection matrix $\mathbf{P}_s$ on the probability of detection (P_D) and the probability of false alarm (P_{FA}) of the END.

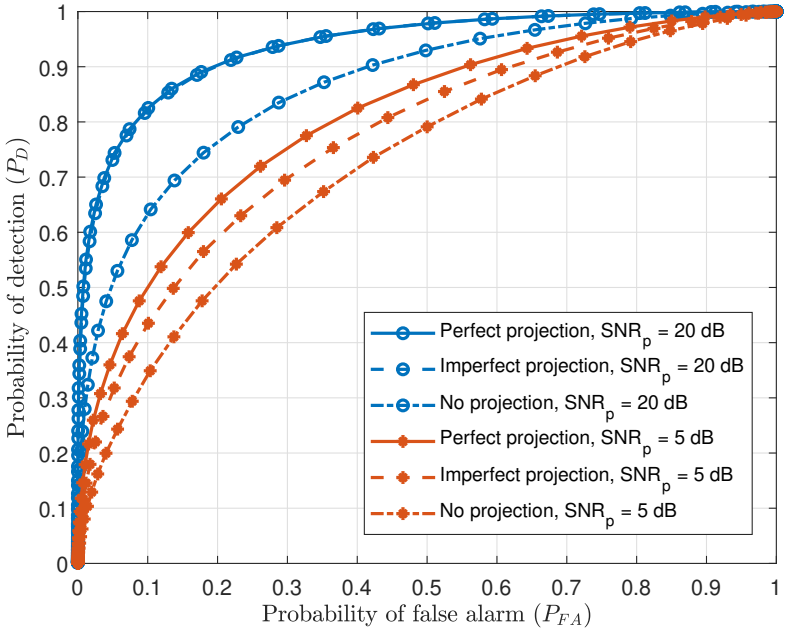

Figure 3.6: The END symbol detection performance at CSP B.

Note that, although we do not estimate $\mathbf{G}_{AB}$ using the pilot signal for the perfect projection and no projection cases, we send the pilot signal in P1 to use it in the detection phase (P2), for a fair comparison.

Compared to the system which works at low SNR$_p$ values, e.g., 5 dB, the system which works at high SNR$_p$ values, e.g., 20 dB, is superior in terms of projecting the transmitted signal onto the nullspace of the dominant direction of $\mathbf{G}_{AB}$ because $\hat{\mathbf{G}}_{AB}$ in P1 is more accurate at high SNR$_p$ values, and this affects the projection matrix accuracy. As seen in the figure, the detection performance of the perfect and imperfect projection cases are almost the same at SNR$_p = 20$ dB, while there is a performance difference between these two cases at SNR$_p = 5$ dB.

In addition, the performance of both the perfect and imperfect projection cases is better than that of the no projection case in each given SNR$_p$ value. This is because the radiated power in the directions which are close to the dominant directions of $\mathbf{G}_{AB}$ decreases while the emitted power in all other directions increases due to the use of $\mathbf{P}_s$. This phenomenon can also be seen in Fig. 3.4. Compared to the no-projection case, for $K = 3$ with the perfect projection case, the radiated power in all directions except the direct link is higher. For example, in Fig. 3.6 at $P_{FA} = 0.1$, the imperfect projection case has almost 0.09 and 0.19 gain in the probability of detection when compared to the no projection case at SNR$_p = 5$ dB and SNR$_p = 20$ dB, respectively.

Chapter 4

Signaling and optimal waveform design

Designing an optimal waveform is relevant to improve RF energy harvesting, as it affects RF-to-direct current (DC) efficiency. By optimizing the waveform design for WPT, the efficiency of the energy conversion process can be improved, and more energy can be harvested from the RF signals. Waveforms to ensure RF-to-DC efficiency gains, typically result in high peak-to-average power ratio (PAPR) signals, which is a property inherent in OFDM signals. In the following, we investigate how OFDM signals can be used in a backscatter communication system to extract wideband channel state information, a pre-requisite for time-of-arrival based localization.

4.1 CSI estimation using wide band OFDM signals

We investigate backscatter communication in wideband bistatic OFDM systems and focus on simultaneous DLI mitigation and CSI estimation in a single-path SISO setup. A time-domain signal model is established to derive an algorithm to separate the weak backscatter signal from the strong DLI by exploiting fast time-variations imposed by the binary OOK modulation of the backscatter modulator. First, an estimator is derived for the unknown phase and unknown frequency of the OOK modulation signal, which incorporates inherent cancellation of the direct link signal. Having an estimate of the phase and frequency of the backscatter modulation signal, the CIR of the direct link channel and the backscatter channel are estimated using a masked ML approach of the separated direct link signal and backscatter signal. The algorithm is evaluated using a scenario specific bistatic SISO setup based on an IEEE 802.11ax OFDM system for the infrastructure and using preambles specified in the electronic product code (EPC) Class 1 Gen 2 radio frequency identification (RFID) standard for the backscatter modulation waveform.

In summary, the derived algorithm is capable of estimating the unknown phase and frequency of the backscatter modulation signal of the system-agnostic END and is capable of providing wideband CSI of the backscatter channel which in turn may be used to enhance power transfer to the END, to enhance the communication (e.g., data-rates) between system and END, or for localisation purposes.

4.1.1 Signal and system model

We consider a bistatic backscatter system as depicted in Figure 4.1 with a single-antenna CSP operating in transmit mode (CSP A) and a single-antenna CSP operating in reception mode (CSP

B). The CSPs run a standardized OFDM transmission mode and are assumed to be phase and sample coherent.

The END is either reflecting or absorbing incoming signals according to a preamble bit sequence. While reflecting, we assume linear behaviour of the END. Transmission between CSPs, i.e. the DLI, and the transmission between END and CSPs, i.e. the downlink (DL) and uplink (UL) channel, are modelled using (complex) sampled baseband equivalent radio channels.

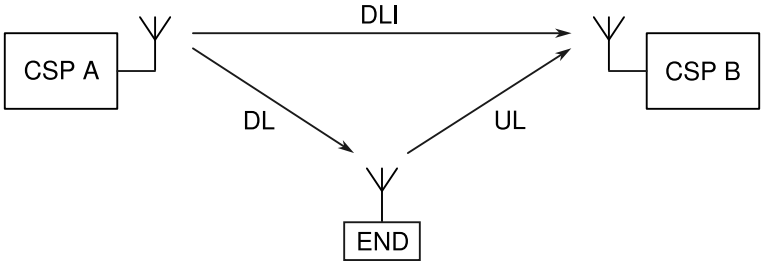

Figure 4.1: System block diagram.

For the following considerations, we use the SISO time-domain model depicted in Figure 4.2. The wide-band OFDM transmit signal $\mathbf{s} \in \mathbb{C}^{\tilde{N}_S \times 1}$ passes through the downlink channel $\mathbf{h}_{\mathrm{DL}} \in \mathbb{C}^{M_{\mathrm{DL}} \times 1}$ to the END where it is modulated with the OOK signal $\mathbf{b} \in \mathbb{C}^{(\tilde{N}_S + M_{\mathrm{DL}} - 1) \times 1}$ as shown in Figure 4.3. $\mathbf{b}$ is a pulse-width modulation (PWM) signal with 50% duty-cycle parameterized by a phase shift $\eta_b \in \mathbb{N}_0$ and a period of $2T_b$.

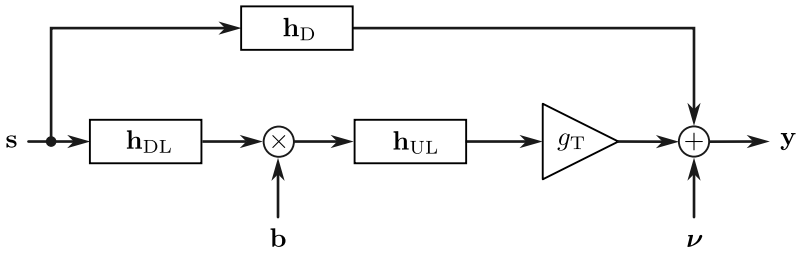

Figure 4.2: SISO time domain signal model.

The reflected signal passes through the uplink channel $\mathbf{h}_{\mathrm{UL}} \in \mathbb{C}^{M_{\mathrm{UL}} \times 1}$ to the system's receiver. Level differences between direct link signal and received backscatter signal are modelled using the gain factor $g_{\mathrm{T}} \in (0, 1)$ (since we assume normalized channel CIRs). At the receiver, the direct link interference ($\mathbf{s}$ passing through the direct link channel $\mathbf{h}_{\mathrm{D}} \in \mathbb{C}^{M_{\mathrm{D}} \times 1}$) is superimposing the backscattered signal along with zero-mean circularly-symmetric complex Gaussian noise $\boldsymbol{\nu} \in \mathbb{C}^{(\tilde{N}_S + M_{\mathrm{D}} - 1) \times 1}$.

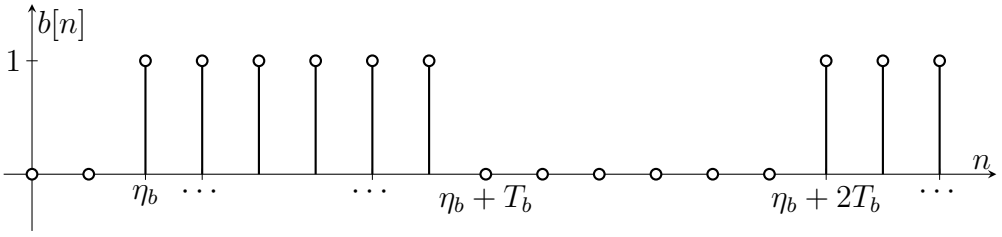

Figure 4.3: Backscatter modulation signal.

The resulting time-domain received signal vector $\mathbf{y} \in \mathbb{C}^{(\tilde{N}_S+M_\mathrm{D}-1)\times 1}$ is

$$\mathbf{y} = \mathbf{H}_\mathrm{D}\mathbf{s} + g_\mathrm{T}\mathbf{H}_\mathrm{UL}\mathbf{B}\mathbf{H}_\mathrm{DL}\mathbf{s} + \boldsymbol{\nu} \tag{4.1}$$

where $\mathbf{H}_\mathrm{DL} \in \mathbb{C}^{(\tilde{N}_S+M_\mathrm{DL}-1)\times \tilde{N}_S}$, $\mathbf{H}_\mathrm{UL} \in \mathbb{C}^{(\tilde{N}_S+M_\mathrm{D}-1)\times(\tilde{N}_S+M_\mathrm{DL}-1)}$ and $\mathbf{H}_\mathrm{D} \in \mathbb{C}^{(\tilde{N}_S+M_\mathrm{D}-1)\times \tilde{N}_S}$ are Toeplitz matrices representing the linear convolution with the corresponding channel CIRs $\mathbf{h}_\mathrm{DL}$, $\mathbf{h}_\mathrm{UL}$ and $\mathbf{h}_\mathrm{D}$. The backscatter modulation is modelled by $\mathbf{B} = \mathrm{diag}\,(\mathbf{b})$.

4.1.2 Direct link and backscatter channel estimation

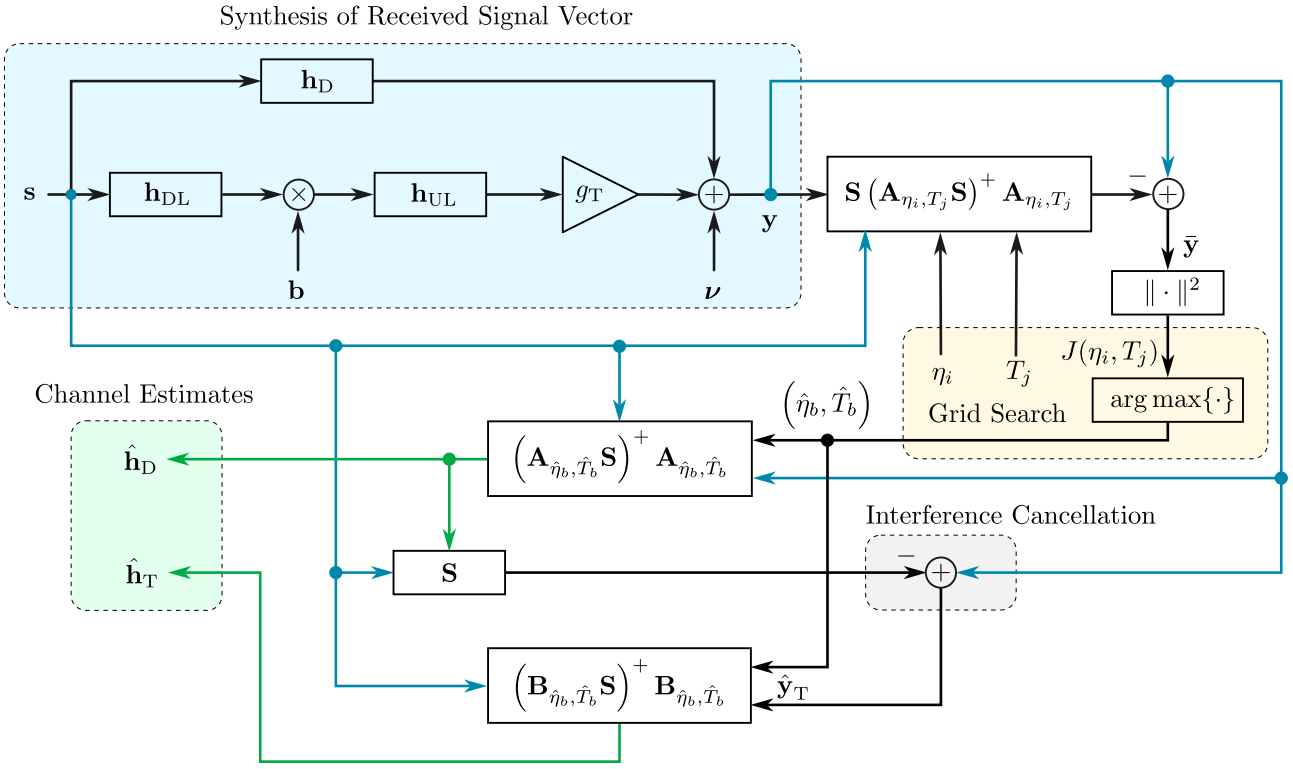

Figure 4.4: Implementation of the signal model and estimation algorithm.

Now that we have established the system and signal model, we implement the algorithm according to Figure 4.4 in order to determine the unknown backscatter modulation parameters and the unknown CIRs. First, we maximize the objective function defined in Equation (4.4) to obtain the unknown phase η_b and pulse-width T_b of the backscatter modulation signal.

$$(\hat{\eta}_b,\hat{T}_b) = \underset{\eta_b,T_b}{\arg\max}\,\|\bar{\mathbf{y}}\|^2 = \underset{\eta_b,T_b}{\arg\max}\,\|\mathbf{y}-\mathbf{S}\hat{\mathbf{h}}_\mathrm{D}\|^2 = \tag{4.2}$$

$$= \underset{\eta_b,T_b}{\arg\max}\left\|\mathbf{y}-\mathbf{S}\left(\mathbf{S}^\mathsf{H}\mathbf{A}^\mathsf{H}_{\eta_b,T_b}\mathbf{A}_{\eta_b,T_b}\mathbf{S}\right)^{-1}\mathbf{S}^\mathsf{H}\mathbf{A}^\mathsf{H}_{\eta_b,T_b}\check{\mathbf{y}}\right\|^2 \tag{4.3}$$

$$= \underset{\eta_b,T_b}{\arg\max}\left\|\left(\mathbf{I}-\mathbf{S}\left(\mathbf{A}_{\eta_b,T_b}\mathbf{S}\right)^+\mathbf{A}_{\eta_b,T_b}\right)\mathbf{y}\right\|^2 \tag{4.4}$$

As already mentioned, the algorithm incorporates inherent cancellation of the direct link signal $\mathbf{H}_\mathrm{D}\mathbf{s} = \mathbf{S}\mathbf{h}_\mathrm{D}$, where $\mathbf{S} \in \mathbb{C}^{M_\mathrm{D}\times(\tilde{N}_S+M_\mathrm{D}-1)}$ is a Toeplitz matrix representing the linear convolution

with the transmit signal s. This is achieved by using a masked and truncated version of the received signal vector

$$\check{\mathbf{y}} = \mathbf{A}_{\eta,T}\mathbf{y} \tag{4.5}$$

to make an attempt to estimate the direct link CIR $\mathbf{h}_{\mathrm{D}}$. The parameterized truncation matrix is of the form

$$\mathbf{A}_{\eta,T} = \left[\begin{array}{ccc|ccc|ccc|c} \overbrace{1 & 0 & \cdot}^{\eta} & \overbrace{\cdot & \cdot & \cdot}^{T} & \overbrace{\cdot & \cdot & \cdot}^{T} & \cdots \\ 0 & \ddots & 0 & \cdot & \cdot & \cdot & \cdot & \cdot & \cdot & \cdots \\ \cdot & \ddots & 1 & 0 & \cdot & \cdot & \cdot & \cdot & \cdot & \cdots \\ \cdot & \cdot & 0 & 0 & \cdots & 0 & 1 & 0 & \cdot & \cdots \\ \cdot & \cdot & \cdot & \cdot & \cdot & \cdot & 0 & \ddots & 0 & \cdots \\ \cdot & \cdot & \cdot & \cdot & \cdot & \cdot & \cdot & \ddots & 1 & \ddots \\ \cdot & \cdot & \cdot & \cdot & \cdot & \cdot & \cdot & \cdot & 0 & \cdots \end{array}\right] \tag{4.6}$$

which is derived from the mask signal $\mathbf{a}$ depicted in Figure 4.5. The mask signal is designed such that it corresponds to the binary complement of the modulation signal $\mathbf{b}$ if we set $\eta_a = \eta_b$ and $T_a = T_b$. The resulting truncation matrix removes all entries from the received signal vector $\mathbf{y}$ which contain components of the backscattered signal, in other words, it ensures that the direct link is estimated only if the END is not transmitting (We ignore transients to the envelope $\mathbf{b}$ caused by the uplink channel $\mathbf{h}_{\mathrm{UL}}$).

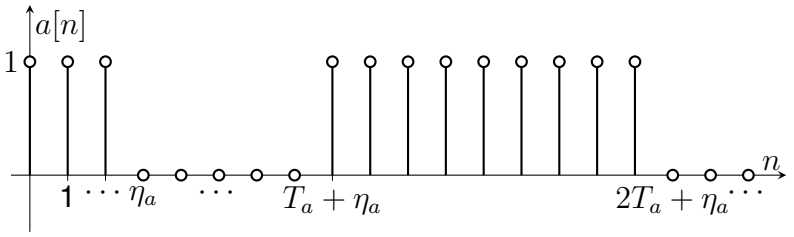

Figure 4.5: Mask signal.

From the truncated received signal vector we obtain the ML estimate

$$\hat{\mathbf{h}}_{\mathrm{D}} = \left(\mathbf{A}_{\eta_b,T_b}\mathbf{S}\right)^{+}\check{\mathbf{y}} \tag{4.7}$$

where $(\cdot)^{+}$ denotes the pseudoinverse. It is evident that Equation (4.7) only works if we know the parameters (η_b, T_b) of the backscatter modulation signal $\mathbf{b}$. This estimator is not suitable for the direct estimation of the parameters of $\mathbf{b}$, yet it can be used for cancelling the direct link signal, since in the noise-free case and with a truncation matrix with arbitrary parameters we get

$$\hat{\mathbf{h}}_{\mathrm{D}} = \mathbf{h}_{\mathrm{D}} + \mathbf{L}\mathbf{h}_{\mathrm{T}} \tag{4.8}$$

where $\mathbf{L} \in \mathbb{C}^{M_{\mathrm{D}} \times (M_{\mathrm{DL}}+M_{\mathrm{UL}}-1)}$ is a leakage matrix which does not depend on $\mathbf{h}_{\mathrm{D}}$, and $\mathbf{h}_{\mathrm{T}} \in \mathbb{C}^{(M_{\mathrm{DL}}+M_{\mathrm{UL}}-1)\times 1}$ is the convolution of downlink and uplink channel.

With this finding, we can construct the residual $\bar{\mathbf{y}}$ for the noise free case, which is

$$\bar{\mathbf{y}} = \mathbf{y} - \mathbf{S}\hat{\mathbf{h}}_{\mathrm{D}} = \mathbf{S}\mathbf{h}_{\mathrm{D}} + \underbrace{\mathbf{B}(\mathbf{S}\mathbf{h}_{\mathrm{T}})}_{\mathbf{y}_{\mathrm{T}}} - \mathbf{S}\hat{\mathbf{h}}_{\mathrm{D}} = \mathbf{S}\mathbf{h}_{\mathrm{D}} + \mathbf{y}_{\mathrm{T}} - \mathbf{S}\mathbf{h}_{\mathrm{D}} - \mathbf{S}\mathbf{L}\mathbf{h}_{\mathrm{T}} = \tag{4.9}$$

$$= \mathbf{y}_{\mathrm{T}} - \mathbf{S}\mathbf{L}\mathbf{h}_{\mathrm{T}} \tag{4.10}$$

where any influence of the direct link channel is eliminated. A crucial property of $\mathbf{L}$ is that it approaches zero if we have the right parameters of the backscatter modulation signal $\mathbf{b}$, i.e., $\mathbf{L} = \mathbf{L}_{\eta,T} \to \mathbf{0}$ for $(\eta, T) \to (\eta_b, T_b)$, which is equivalent to maximizing the energy of the residual $\bar{\mathbf{y}}$ as initially stated in Equation (4.4). Since Equation (4.4) is a nonlinear integer optimization problem, we employ grid search over a sensible set of parameters η_b and T_b which are of practical relevance. The implementation is summarized by Algorithm 2.

Now, having the parameters of $\mathbf{b}$, we can reapply the estimator in Equation (4.7) to obtain the direct link channel. This estimate is used to perform the final interference cancellation by convolving it with the transmit signal and subtracting it from the received signal $\mathbf{y}$ to get

$$\hat{\mathbf{y}}_{\mathrm{T}} = \mathbf{y} - \mathbf{S}\hat{\mathbf{h}}_{\mathrm{D}}. \tag{4.11}$$

The backscatter CIR is obtained in analogous fashion to Equation (4.7), resulting in

$$\hat{\mathbf{h}}_{\mathrm{T}} = \left(\mathbf{B}_{\hat{\eta},\hat{T}}\mathbf{S}\right)^{+} \mathbf{B}_{\hat{\eta},\hat{T}}\hat{\mathbf{y}}_{\mathrm{T}} \tag{4.12}$$

where $\mathbf{B}_{\hat{\eta},\hat{T}}$ is the truncation matrix derived from the estimated backscatter modulation signal, which corresponds to the binary complement of $\mathbf{A}_{\hat{\eta},\hat{T}}$.

Algorithm 2: Backscatter modulation signal parameter estimation.

Require: set of modulation phases $\{\eta_i\}_{i=1}^{N_\eta}$, set of modulation pulse widths $\{T_j\}_{j=1}^{N_T}$, reference transmit signal $\mathbf{s}$, synthesized or measured received signal $\mathbf{y}$

$J \leftarrow \mathbf{0}$

$\mathbf{S} \leftarrow \texttt{convmtx}(\mathbf{s})$; `// Create Toeplitz convolution matrix from transmit signal`

for all η_i, T_j **do**

$\mathbf{a} \leftarrow \neg\mathbf{b}(\eta_i, T_j)$; `// Mask derived from binary complement of modulation signal`

$\mathbf{A} \leftarrow \texttt{truncmtx}(\mathbf{a})$; `// Create truncation matrix from mask signal`

$\mathbf{S}^{+} \leftarrow (\mathbf{A}\mathbf{S})^{+}$; `// Create pseudoinverse of truncated transmit conv. matrix`

$\hat{\mathbf{h}}_{\mathrm{D}} \leftarrow \mathbf{S}^{+}(\mathbf{A}\mathbf{y})$; `// Direct link channel estimate for current parameters`

$\bar{\mathbf{y}} \leftarrow \mathbf{y} - \mathbf{S}\hat{\mathbf{h}}_{\mathrm{D}}$; `// Create residual by attempting a DLI cancellation`

$J(\eta_i, T_j) \leftarrow \|\bar{\mathbf{y}}\|^2$; `// Assign energy of residual to objective function`

end for

$(\hat{\eta}, \hat{T}) \leftarrow \arg\max J(\eta_i, T_j)$

Ensure: $\hat{\eta}$, $\hat{T}$, J

4.1.3 Estimation performance and outlook

The implementation in Figure 4.4 is evaluated using a scenario specific setup, where the system sample rate, the OFDM subcarrier count and the subcarrier spacing of the transmit signal are defined by an IEEE 802.11ax transmission mode operating at $2.44\,\text{GHz}$ with $80\,\text{MHz}$ bandwidth. The backscatter modulation signal is based on an FM0 Extended Preamble defined in the EPC Class 1 Gen 2 RFID standard, which corresponds to a $40\,\text{kHz}$ and $50\,\%$ duty-cycle PWM signal with a total duration of $300\,\mu\text{s}$.

The level difference g_T signal-to-interference ratio (SIR) between DLI and backscattered signal at the receiver is derived from a path-loss model (path-loss exponent $\alpha = 2$). The distances which determine the path-loss values are indicated in Figure 4.6. For the END, we assume ideal reflection for $b[n] = 1$ and ideal absorption for $b[n] = 0$. The resulting SIR is in the range of $-55\,\text{dB}$, for the DLI we assume a high quality transmission (SNR $> 30\,\text{dB}$).

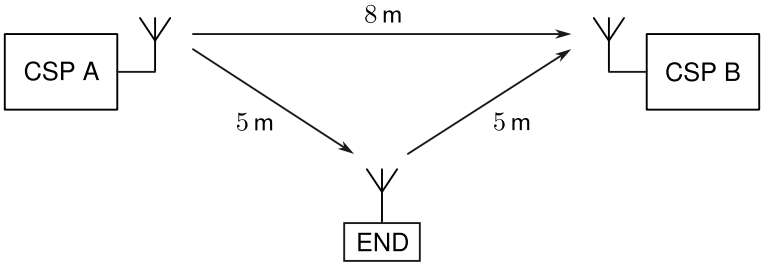

Figure 4.6: Scenario for the path-loss model.

For the defined scenario, the parameters of the backscatter modulation signal $\mathbf{b}$ are correctly detected, which is crucial to perform the estimation of the DLI used to obtain the backscattered signal. From the interference-cleared signal, the estimate of the backscatter CIR is obtained and visualized in Figure 4.7.

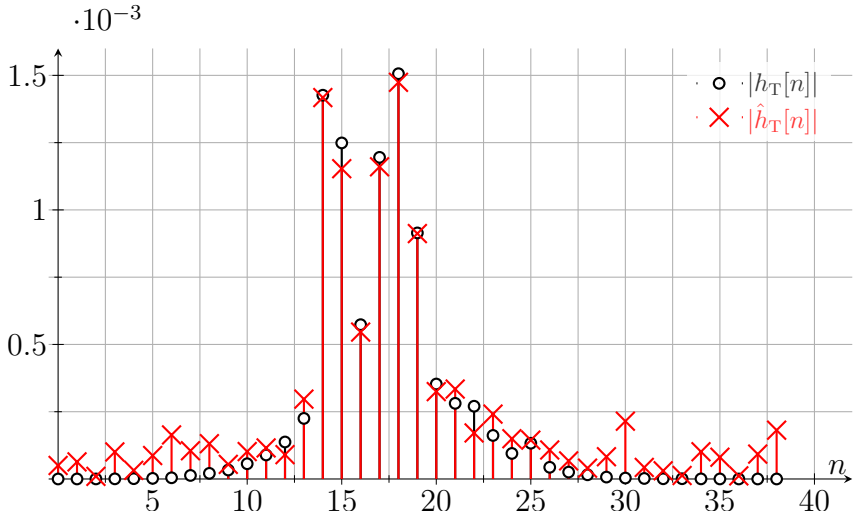

Figure 4.7: Scenario specific estimate of the backscatter channel CIR.

In order to quantify the estimation accuracy, we define the SNR of the CIR

$$\mathrm{SNR}_{\mathrm{T}} = 10 \cdot \log\left(\frac{\|\mathbf{h}_{\mathrm{T}}\|^2}{\frac{1}{M_{\mathrm{T}}}\|\mathbf{h}_{\mathrm{T}} - \hat{\mathbf{h}}_{\mathrm{T}}\|^2}\right) \tag{4.13}$$

where $M_{\mathrm{T}} = M_{\mathrm{DL}} + M_{\mathrm{UL}} - 1$ is the model order of the backscatter channel CIR $\mathbf{h}_{\mathrm{T}}$, which represents the convolution of $\mathbf{h}_{\mathrm{DL}}$ with $\mathbf{h}_{\mathrm{UL}}$. In the specified scenario, we get a good $\mathrm{SNR}_{\mathrm{T}} \approx 28\,\mathrm{dB}$, suggesting a high processing gain as the backscattered signal is way below the noise floor.

In conclusion, we established a time-domain model for a SISO bistatic backscatter communication system using wide-band OFDM signals. From the time-domain model, an algorithm is derived to estimate the unknown parameters of the backscatter modulation signal which includes inherent DLI cancellation. The parameters of the backscatter modulation signal are required to separate the strong DLI from the weak backscattered signal to get separated CSI, but without separated CSI, we may not be able to get these parameters, since they are strongly interfered. However, by exploiting the masking property of the backscatter modulation signal, a solution was found to estimate the parameters without prior knowledge of the channels.

Potential applications of the obtained CSI include:

- Adaption to MIMO and single-input multiple-output (SIMO) setups to perform reciprocity-based beamforming to enhance WPT to an END
- Enhance communication (data-rates, robustness) between END and CSP
- Localization and tracking of ENDs using the wide-band CSI

Chapter 5

Optimal hardware design

The optimal hardware design for energy harvesting systems is one that maximizes energy conversion efficiency while meeting the specific requirements and constraints of the application. This requires a careful balance between the energy harvesting source, the energy storage, and the power management subsystems. The design should also consider the physical form factor and size constraints, as well as the expected operating environment and conditions.

5.1 Device performance evaluation

This section provides concluding information about general physical and regulatory limits of harvesting in the 2.4 GHz Wi-Fi industrial, scientific and medical (ISM)-band. The harvesting performance of the NXP test-integrated circuit (IC) with integrated charge-pump is also outlined here. Furthermore, results on the expected maximum reachable harvesting distance are provided with the current hardware device described in deliverable D4.2 [12]. It must be noted that the sSUF Test-IC with integrated charge pump was designed for UHF ($860 \ldots 960$ MHz) and the results show the performance in a different frequency range (2.4 GHz ISM) the design was not intended for. An optimized design and layout for 2.4 GHz would therefore significantly improve the conversion efficiency and effective harvested power.

5.1.1 Physical and regulatory limitations

The maximum possible transmit power for an RF transmitter in the 2.4 GHz ISM band is limited to 20 dBm (=100 mW) equivalent isotropically radiated power (EIRP). The EIRP is here defined as:

$$\mathrm{EIRP} = P_{\mathrm{t}} - L_{\mathrm{app}} + G_{\mathrm{t}}\,, \tag{5.1}$$

with P_{t} as the RF power provided by the transmitter (output stage, amplifier, etc.), L_{app} for the application loss due to various losses (e.g., matching, cable loss, etc.), and G_{t} for the transmitter antenna gain. A higher antenna gain therefore does not increase the maximum possible distance between transmitter and receiver (RF harvesting device), since the EIRP must stay below 20 dBm and the transmit power must therefore be adjusted accordingly.

The maximum RF power provided by the transmitter can be determined like following:

$$P_{\mathrm{TX,max}} = \mathrm{EIRP}_{\mathrm{max}} + L_{\mathrm{app}} - G_{\mathrm{t}}\,, \tag{5.2}$$

for a given system with known application loss and transmitter antenna gain. The received RF power can be determined with the Free-Space-Path-Loss or Friis-Equation:

$$P_{\mathrm{r}} = P_{\mathrm{t}}\, G_{\mathrm{t}}\, G_{\mathrm{r}} \left(\frac{\lambda}{4\pi R}\right)^2 , \tag{5.3}$$

where G_{r} is defined as the receiver antenna gain, λ for the wavelength and R for the distance between transmitter and receiver, or in this case the harvesting device. For a normalized distance of $1\,\mathrm{m}$, a free space path loss of $40\,\mathrm{dB}$ (at $2.4\,\mathrm{GHz}$)/m up to $40.4\,\mathrm{dB}$ (at $2.5\,\mathrm{GHz}$)/m can be determined. These two factors, the maximum allowed transmit power and the power loss per meter therefore limit and highly affect the RF harvesting as physical and regulatory limitation.

5.1.2 Limitations of current setup

The current μPP (microPowerProfiler) harvesting device is equipped with a unidirectional dipole antenna with an antenna gain of $G_{\mathrm{r}} = 1.765\,\mathrm{dBi}$ (at $2.4\,\mathrm{GHz}$) down to $G_{\mathrm{r}} = 1.675\,\mathrm{dBi}$ (at $2.5\,\mathrm{GHz}$). These values are the simulation results of the antenna design process and were not calculated by measuring the antenna characteristics since the antenna was directly matched to the RF port impedance. This allowed omitting the matching network for a default $50\,\Omega$ antenna to the chip impedance and therefore reduces any additional losses. As seen in Fig. 5.1, the performance of the entire harvesting device was then characterized in an anechoic chamber by sweeping the transmit power on the transmitter side and measuring the effective maximum harvested power tuned with the variable load (with a variable load from $0\,\Omega$ to $1\,\mathrm{M}\Omega$ and tracked by an maximum power point tracker (MPPT) for ideal load behavior) for different frequencies within the $2.4\,\mathrm{GHz}$ ISM band. Looking at the frequency range this leads to a maximum power conversion efficiency

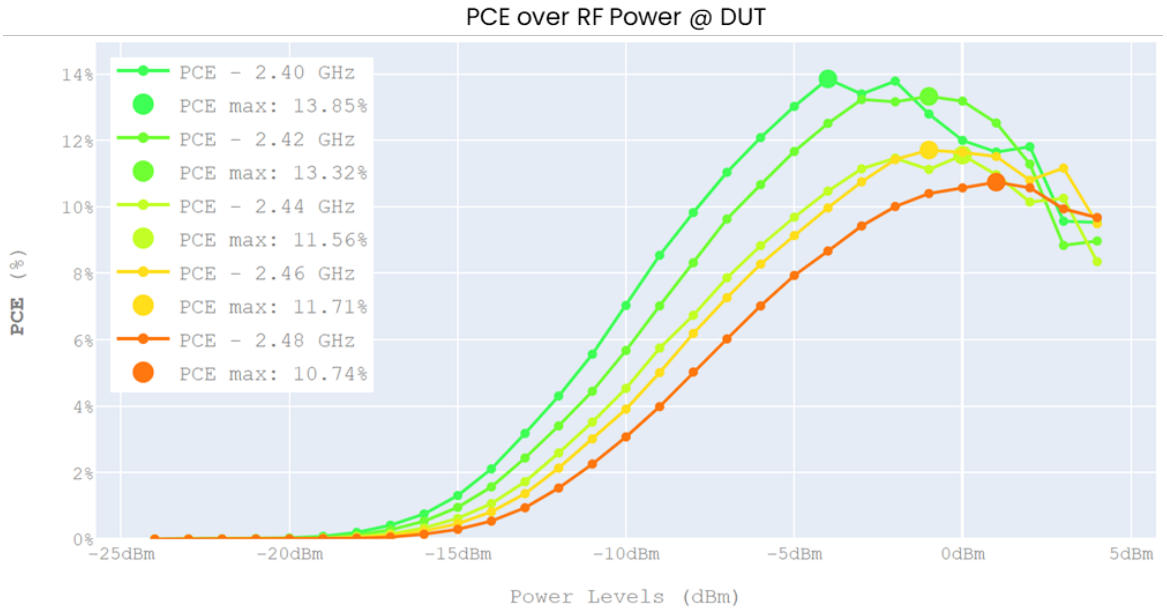

Figure 5.1: Power conversion efficiency (PCE) of the harvesting device versus available power versus frequency.

(PCE) of $13.85\,\%$ (at $2.40\,\mathrm{GHz}$) down to $10.74\,\%$ (at $2.48\,\mathrm{GHz}$) as seen in Fig. 5.2.

A minimum power of $-19\,\mathrm{dBm}$ must be available at the RF harvesting device, i.e., the device under test (DUT), to get the *charge pump voltage above* $100\,\mathrm{mV}$. A minimum transmit power of

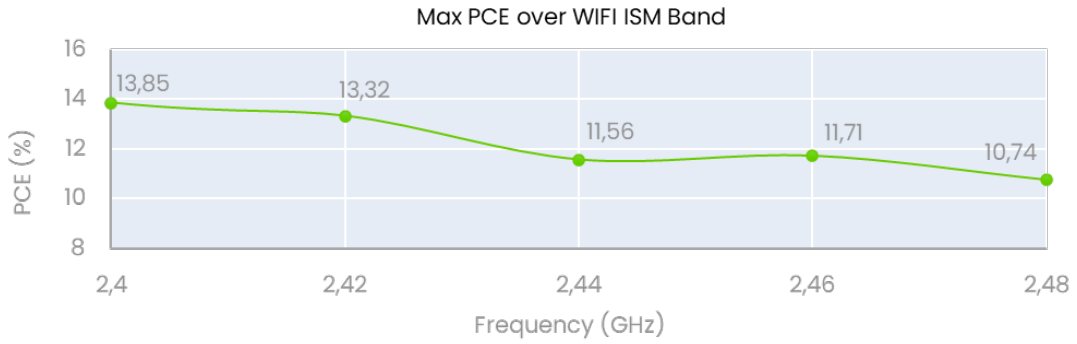

Figure 5.2: Maximum PCE over the WIFI ISM Band.

$-17\,\mathrm{dBm}$ must be available to get *over* $1\,\%$ *of conversion efficiency* and $> -14\,\mathrm{dBm}$ must be available to get *more than* $1\,\mu\mathrm{W}$ *output power* for a RF harvesting powered load connected to the charge pump.

It must be noted that the *antenna efficiency of the receiver antenna was not considered for these measurements, only the simulated antenna gain* was included in the PCE calculations. An antenna design with high efficiency could therefore also improve the PCE significantly.

5.1.3 Office-environment SISO measurement

The measurement setup is given in Fig. 5.3. To get realistic and close to "real life" RF harvesting results, measurements were performed in the office in a standard work environment with furniture surrounding the measurement setup and active Wi-Fi access points in the office building. The RF transmitter was simulated with a continuous wave (CW) transmitter operating at $2.4\,\mathrm{GHz}$ and output power of $16\,\mathrm{dBm}$ (maximum transmit power of this device). The application loss was estimated with around $2\,\mathrm{dB}$ for connection and cable losses and the antenna gain of the unidirectional dipole antenna is $2\,\mathrm{dBi}$. This leads to an EIRP of approximately $16\,\mathrm{dBm}$. By measuring

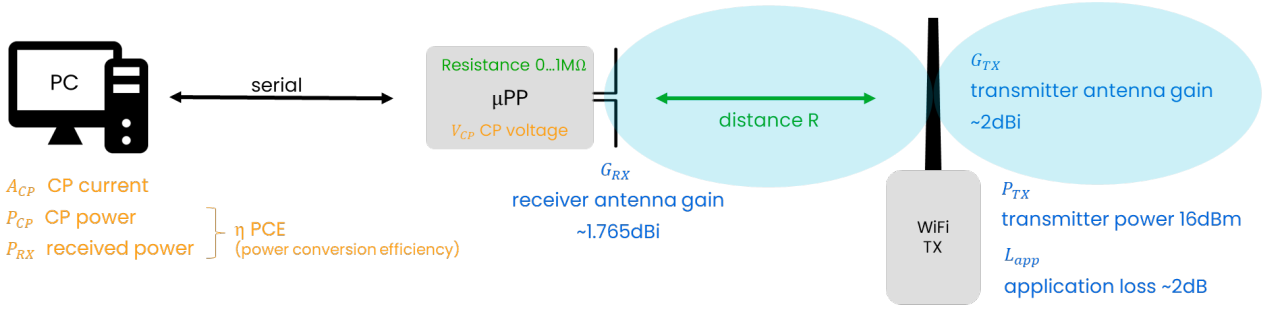

Figure 5.3: The measurement setup.

the effective harvested power (with a variable load from $0\,\Omega$ to $1\,\mathrm{M}\Omega$ and tracked by an MPPT for ideal load behavior) over various distances from $10\,\mathrm{cm}$ up to $1\,\mathrm{m}$ following graph in Fig. 5.4 to determine the maximum harvestable power at each distance was determined (current status). All further distances from $60\,\mathrm{cm}$ to $1\,\mathrm{m}$ were not included since the effective harvested power was neglectable. The maximum harvested power at $50\,\mathrm{cm}$ was $0.355\,\mu\mathrm{W}$ while at $60\,\mathrm{cm}$ there was close to no power available at the charge pump output ($0.006\,\mu\mathrm{W}$). The unidirectional dipole antennas were always perfectly aligned parallel to each other, the polarization on the receiving and

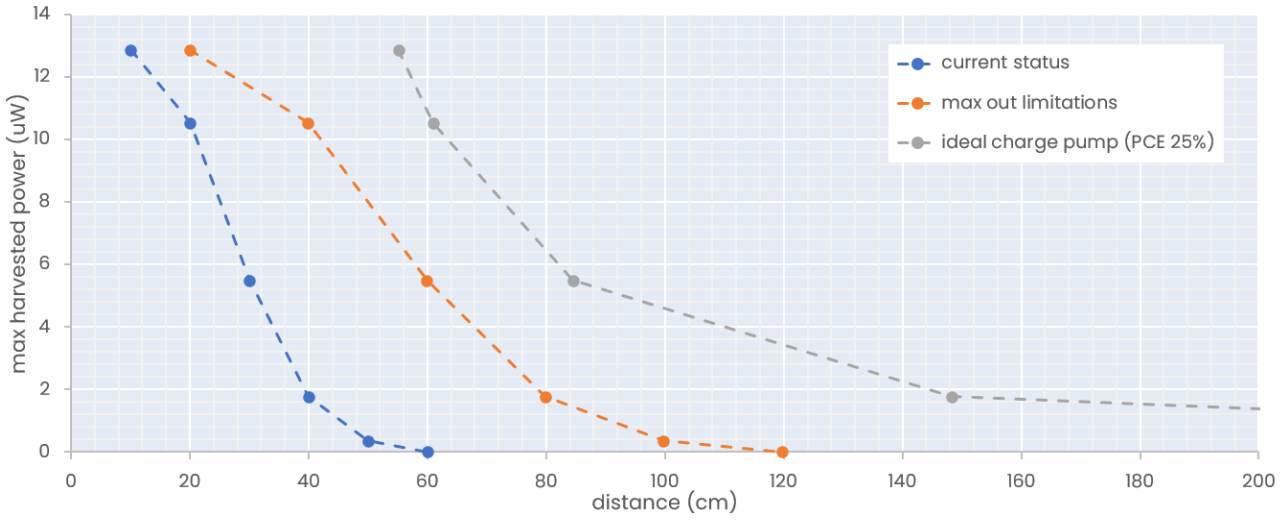

Figure 5.4: Maximum harvested power over various distances.

transmitting side was the same – therefore this measurement still resembles an optimal environment without the harvesting device placed randomly with various angles next to the transmitter and maybe even obstacles in the line of sight between transmitter and receiver/RF-harvester.

5.1.4 Conclusion

The measurement results clearly show that RF energy harvesting with current state of the art RF-charge-pumps is possible – but with restrictions, meaning close distance operation at very low output power level in the uWatts region. Maxing out these limitations, a slightly higher harvesting distance can be achieved as seen in the plot (max out limitations). Since the maximum transmit power is strictly regulated and the free space path loss is rather high with around $40\,\mathrm{dB}$ after $1\,\mathrm{m}$ in the $2.4\,\mathrm{GHz}$ ISM band, the PCE performance of the harvesting device is crucial. Further, the exact use case of the harvesting device/product must be known to increase the overall performance. This can be achieved by decreasing any additional losses (matching, ideal point of operation – MPPT) and by choosing a high receiving antenna gain for stationary harvesting devices to further condense the maximum possible RF energy at the harvesting location. Improved RF-charge-pumps with PCEs of $25\,\%$ *down to* $-24\,\mathrm{dBm}$ (approx. $4\,\mu\mathrm{W}$) would already lead to an *effective harvestable power* of $1\,\mu\mathrm{W}$ which is mostly enough to power today's low-power sensor-nodes in sleep mode and therefore could increase the battery lifetime significantly. The plot above (ideal charge pump) should provide an outlook about which distances can be achieved if the internal charge pump would have such a high PCE of $25\,\%$ over the utilized power range.

5.2 Design considerations in specific use cases

5.2.1 Wireless power transfer: A service in 6G

The sustainability benefits of using EN devices become particularly significant for massive device deployments. Some 6G use cases, such as electronic labeling, asset tracking, and real-time inventory, will involve a large number of distributed devices [2]. While EN devices can be designed with low complexity and manufactured at very low cost, the most demanding functional requirements will be offloaded to the infrastructure side. To ultimately serve these use cases with EN

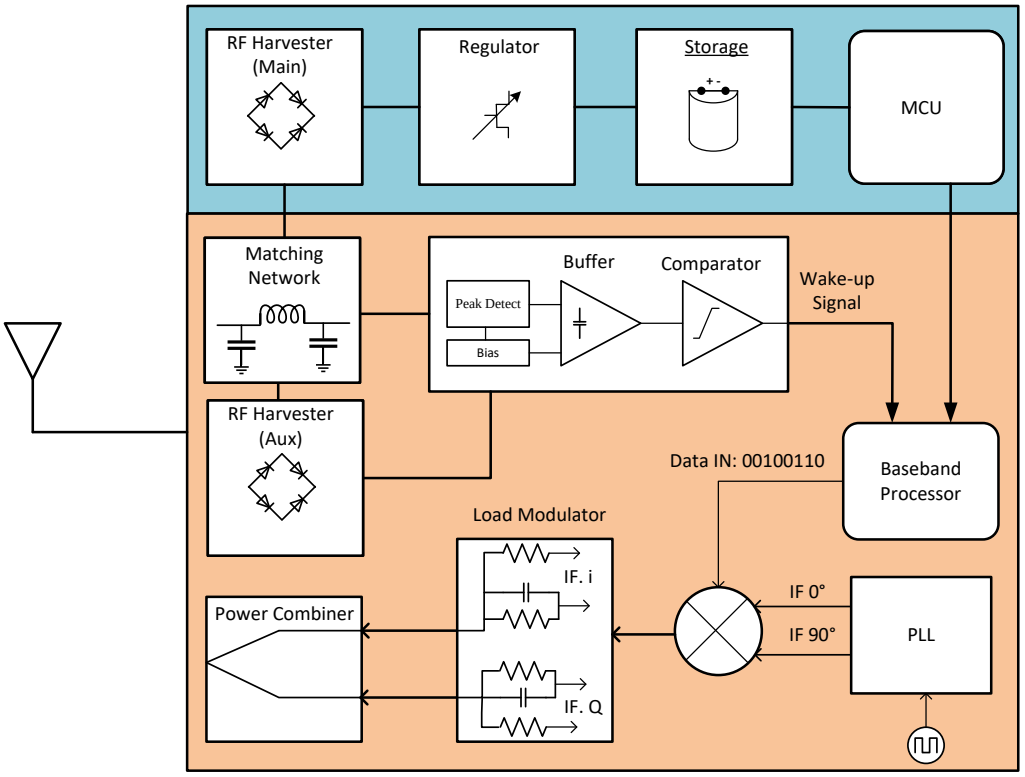

Figure 5.5: EN device architecture operating in the RadioWeaves infrastructure: Unprecedented power budgets at the device-side demand novel a front-end design with one branch providing a high sensitivity during the initial access phase and another branch providing optimum efficiencies at high input powers.

devices requires a radio infrastructure capable of providing WPT as a service.

5.2.2 RadioWeaves: A distributed 6G radio infrastructure

As an example of a 6G radio infrastructure, RadioWeaves consists of distributed antenna arrays that cooperatively provide hyper-diverse connectivity, computational resources, positioning, and WPT to connected devices. In this document, we illustrate the benefits of such an infrastructure for WPT based on the measurements obtained with a single, physically large URA mounted in a hallway (see Fig. 2.1). An actual RadioWeaves deployment would involve many such arrays, which would yield an even larger “combined” aperture of the infrastructure **techtile**.

5.2.3 Energy neutral devices

Battery-less EN devices hold the potential to advance IoT deployments, offering cost-effective and sustainable solutions on a massive scale. In the REINDEER deliverables D4.1 and D4.2 [12], [48], we demonstrate that physically large apertures operating at sub-10 GHz frequencies result in unprecedented milliwatt-level power budgets. Advancing future radio infrastructures that provide these WPT capabilities will require novel device designs that can accommodate these substantial power budgets.

A state-of-the-art strategy involves designing EN devices to operate with maximum efficiency at their device sensitivity, which is the minimum input power required for wake-up, thus maximizing

their initial access distance. Traditionally, the power harvesting efficiency of the front-end degrades at higher input powers, posing a challenge for simultaneous efficient operation at both the device sensitivity and the maximum power budget. We propose a front-end design with two branches to address this challenge, as illustrated in Fig. 5.5. The lower branch is dedicated to solving the initial access problem, while the upper one is responsible for harvesting the maximum power from the focal region once it is established. These branches have different requirements, leading to the development of two distinct harvesting strategies named main RF harvester (MRFH) and auxiliary RF harvester (ARFH), respectively. The ARFH must operate at very low sensitivities (e.g., down to $-25\,\mathrm{dBm}$, typical for RFID tags) with high conversion efficiency to provide sufficient energy for driving the wake-up signal processing, the baseband processor, and the modulator. Conversely, the MRFH must operate at high voltages (above $5\,\mathrm{V}$) to be able to properly deliver power levels in the range of $100\,\mathrm{mW}$ to the storage device in order to efficiently drive power-consuming functions on the MCU. As a consequence, the ARFH is composed of stages of concatenated charge pumps [49], and the MRFH is fabricated as a single bridge rectifier using Schottky diodes to provide minimal forward voltage drop. These contradicting requirements prohibit the integration of both types of harvesters on a single die in a cost-effective way. The main contributing factors are the electrostatic discharge (ESD) protection, the maximum tolerable semiconductor process voltage (usually below $5\,\mathrm{V}$), and the utilization of specific transistor types w.r.t. efficiency versus operational voltage tolerance. Hence, the low-power branch is built as an integrated solution, while the high-power branch is located off-chip. Both branches are connected through a dedicated matching network and ESD protection to the antenna.

Chapter 6

Summary

In Chapter 2, we demonstrated how a RadioWeaves infrastructure enables functional features such as efficiency, mobility support, robustness, and reliability through learning characteristic parameters from the environment such as device positions and amplitude models. The RadioWeaves infrastructure benefits from massive deployments of antennas leveraging beamforming and diversity. In Section 2.1, we show that even a simple geometry-based spherical wavefront LoS beamformer can outperform a reciprocity beamformer in the linear SNR regime if accurate position information is available, hence we demonstrate that environment-awareness can increase the beamforming *efficiency*. We achieve *robustness* by introducing a channel fusion method to combine measured CSI and predicted CSI by incorporating the uncertainty of the individual type of CSI available. Our method successfully selects (actually a combination) the most reliable type of CSI, i.e., measured and predicted CSI. Thereby, channel fusion can achieve *efficiency* in low-SNR scenarios where a geometry-based beamformer may outperform a reciprocity-based beamformer, and it achieves *robustness* by relying on measured CSI if the geometry-based channel model breaks down. In the initial results presented, we addressed the *reliability* aspect only in terms of a successful "handover" through *measured CSI* from RWs with less favorable channel conditions to RWs with more favorable channel conditions. We will fully develop our positioning and tracking algorithm which will allow us to demonstrate the potential of mobility support in a RadioWeaves infrastructure. In future deliverables, we will show how a state-space model will allow tracking and prediction of EN device positions at arbitrary time steps. Combined with our geometry-based channel model, we will be able to predict CSI even for devices with high mobility and achieve robustness by proactively beamforming to their next anticipated positions.

In Section 2.2, we have shown that it is possible to extract the LoS and MPCs amplitudes when floor plan knowledge is given. The environment has a great influence on the measured channel, meaning that obstructions, different building materials and diffuse scattering surfaces all introduce very complex effects into the signal amplitudes. Using the extracted amplitudes, a regression model for prediction of the channel in the environment was built. For this environment model, it was necessary to employ data compression algorithms due to the high amount of available data in massive MIMO systems. We proposed a Fourier-based algorithm to compress these extracted amplitudes in order to highly reduce the necessary amount of data to be stored in the environment model. It was possible to achieve low reconstruction errors while keeping the burden on data storage very low, which would not be the case for other evaluated methods. The Fourier-based compression strategy also allowed for accurate prediction of CSI. However, continuous adaption of the environment model was necessary, since the model is only valid in regions where

measurements are available. Additionally, large parts of the channel were not described by the SMC and present due to diffuse scatterers in the room. In the context of WPT algorithms, we used the predicted weights for MRT to show the usefulness of an environment model in other algorithms.

We proposed a novel transmission scheme to be used in a BiBC setup with multiple reader and CE antennas in Chapter 3. The transmission scheme first estimates the channel between the CE (CSP A) and the reader (CSP B), and then uses this estimated channel to beamform the transmission from CSP A. In this beamforming, we propose to apply a specially designed projection matrix whose effect is to mitigate the DLI and decrease the required dynamic range of the reader circuitry. We showed that the dynamic range is significantly decreased by the introduction of the projection matrix in the beamforming, which in turn enables the use of low-resolution ADCs which are low-cost and energy-efficient. Furthermore, we derive a detection algorithm based on a GLRT to detect the symbol/presence of the END at the reader. Joint usage of the proposed transmission scheme and detection algorithm results in a BiBC system with improved detection performance. This can be seen as a baseline approach to operate BiBC systems where both the CE and the reader are equipped with multiple antennas.

In Chapter 4, we established a time-domain model for a SISO bistatic backsactter communication system using wide-band OFDM signals. From the time-domain model, an algorithm to estimate the unknown parameters of the backscatter modulation signal was derived which includes inherent DLI cancellation. The parameters of the backscatter modulation were used to obtain the separated wide band CSI of the system using a masked ML approach. The obtained CSI can be potentially used for enhancement of WPT to a END in a SIMO or MIMO setup, to improve robustness and data-rates for the backscatter communication with a END or for localization and tracking of ENDs.

In Chapter 5, we investigate hardware design of the energy harvesting system and focus on critical aspects such as energy conversion efficiency, harvesting performance, and regulatory constraints. Despite the challenge posed by degradation in power harvesting efficiency at higher input powers, our proposed front-end design with two branches presents a promising solution. By leveraging low sensitivity and high conversion efficiency in one branch, while employing high voltage operation in the other, we aim to ensure efficient energy provision for initial access and drive microcontroller units (MCUs).

Appendix A

Channel prediction and fusion

This appendix contains derivations for Section 2.1.

A.1 Jacobian: Channel prediction uncertainty

To compute the Jacobian $\boldsymbol{J}_k = \frac{\partial \widetilde{\boldsymbol{h}}_k}{\partial \boldsymbol{\eta}_{\mathsf{p}}^{\mathsf{T}}}$ from (2.23) on page 14, we make the Assumption A3 (i.e., an approximation) that the *sensitivities* $\partial\sqrt{G}/\partial\boldsymbol{p}_k \approx \boldsymbol{0}$, since the phase-term (complex exponential) in the channel $[\widetilde{\boldsymbol{h}}_k]_m$ is most sensitive about the position $\boldsymbol{p}_k$ (see below for an explanation). Futhermore, since our PF does not cover a distribution of $\gamma_{k,m}$, we compute the Jacobian $[\boldsymbol{J}_k]_m$ solely through the position $\boldsymbol{p}_k$, hence its number of rows reduces to $\mathcal{D}_{\mathsf{p}} = 3$.

We apply the chain rule to expand

$$
\begin{aligned}
[\boldsymbol{J}_k]_{:,m} &= \frac{\partial[\widetilde{\boldsymbol{h}}_k]_m}{\partial \boldsymbol{p}_k^{\mathsf{T}}} \quad \in \mathbb{C}^{1\times\mathcal{D}_{\mathsf{p}}} \quad \text{into} \\
&= \Bigg[\underbrace{\frac{\partial r_{k,m}^{(x)}}{\partial \boldsymbol{p}_k}}_{\text{III}} \underbrace{\frac{\partial d_{k,m}}{\partial r_{k,m}^{(x)}}}_{\text{II}} + \underbrace{\frac{\partial r_{k,m}^{(y)}}{\partial \boldsymbol{p}_k}}_{\text{III}} \underbrace{\frac{\partial d_{k,m}}{\partial r_{k,m}^{(y)}}}_{\text{II}} + \underbrace{\frac{\partial r_{k,m}^{(z)}}{\partial \boldsymbol{p}_k}}_{\text{III}} \underbrace{\frac{\partial d_{k,m}}{\partial r_{k,m}^{(z)}}}_{\text{II}} \Bigg] \underbrace{\frac{\partial[\widetilde{\boldsymbol{h}}_k]_m}{\partial d_{k,m}}}_{:=\text{I}} ,
\end{aligned}
\tag{A.1}
$$

where, for the forward problem (i.e., channel prediction), we use $\boldsymbol{r}_{k,m} = \boldsymbol{p}_m^{\mathsf{g}} - \boldsymbol{p}_k = [r_{k,m}^{(x)},\ r_{k,m}^{(y)},\ r_{k,m}^{(z)}]^{\mathsf{T}}$ to define the vectorial distance from the mirror EN device at position $\boldsymbol{p}_k$ (the dependence on time step n omitted for notational brevity) to an antenna m at a position $\boldsymbol{p}_m^{\mathsf{g}} = \boldsymbol{p}_m^{\mathsf{a}} + \boldsymbol{p}_{n_{\mathsf{s}}}^{\mathsf{RW}}$ in global coordinates (the dependence on n_{s} omitted for notational brevity). We have the scalar distance $d_{k,m} = \|\boldsymbol{r}_{k,m}\|$ and $\boldsymbol{p}_k = [p_x^{(k)},\ p_y^{(k)},\ p_z^{(k)}]^{\mathsf{T}}$.

Using the channel model in (2.2) expressed for a particular frequency f of interest, we get

$$
[\widetilde{\boldsymbol{h}}_k]_m = \sqrt{G_{\mathrm{r}}}\,\sqrt{G_{\mathrm{t}}}\,\frac{\lambda}{4\pi d_{k,m}}\,\gamma_{k,m}\,g_{k,m}^{\mathsf{pol}}\,e^{-j\frac{2\pi}{c}f\,d_{k,m}} .
\tag{A.2}
$$

Under Assumption A3, we have

$$\text{I} = \frac{\partial[\widetilde{\boldsymbol{h}}_k]_m}{\partial d_{k,m}} \tag{A.3}$$

$$\overset{\text{A3}}{\approx} -\left(\underbrace{\frac{1}{d_{k,m}}}_{:=t_1} + j\underbrace{\frac{2\pi}{c}f}_{:=t_2}\right)[\widetilde{\boldsymbol{h}}_k]_m\,, \tag{A.4}$$

where we can readily observe that the term $t_2 \approx 115/\text{m}$ (at $f = 5.5\,\text{GHz}$), proportional to the sensitivity of the channel phase w.r.t. the position, is usually much larger than the sensitivity term $t_2 < 1/\text{m}$ of the path loss w.r.t. the position. The same would hold for the transmit and receive gain pattern G_t and G_r, as well as the reflection coefficients $\gamma_{k,m}$.

Given that

$$d_{k,m} = f(\boldsymbol{r}_{k,m}) = \|\boldsymbol{r}_{k,m}\| = \left(r_{k,m}^{(x)\,2}, r_{k,m}^{(y)\,2}, r_{k,m}^{(z)\,2}\right)^{\frac{1}{2}}\,, \tag{A.5}$$

and using $i, j \in \{x,\, y,\, z\}$ we compute

$$\text{II}: \quad \frac{\partial d_{k,m}}{\partial r_{k,m}^{(i)}} = \frac{r_{k,m}^{(i)}}{\|\boldsymbol{r}_{k,m}\|}\,, \tag{A.6}$$

which, for all components i, amounts to a unit vector in the direction of $\boldsymbol{r}_{k,m}$.

When dealing with mirror device positions (i.e., $k > 1$), for computing III, the vectorial distance $\boldsymbol{r}_{k,m}$ could be decomposed into terms depending on the physical device position and into terms independent of the physical device position. Using (2.5), any point in global Cartesian coordinates can be mirrored across an infinite planar surface defined through an *arbitrary* point on the surface $\boldsymbol{p}_k^\text{w}$ and a unit-vector $\boldsymbol{n}_k^\text{w}$ normal to its surface. Hence, *mirror device* positions $\{\boldsymbol{p}_k | k > 1\}$ can be computed from the *physical device* position $\boldsymbol{p}_1$ using

$$\boldsymbol{p}_k = \boldsymbol{p}_1 - 2\underbrace{\left((\boldsymbol{p}_1 - \boldsymbol{p}_k^\text{w})^\mathsf{T}\boldsymbol{n}_k^\text{w}\right)}_{=l}\boldsymbol{n}_k^\text{w}\,, \tag{A.7}$$

and further we have

$$\boldsymbol{r}_{k,m} = \boldsymbol{p}_m^\text{g} - \boldsymbol{p}_k \tag{A.8}$$

$$= \boldsymbol{p}_m^\text{g} - \boldsymbol{p}_1 + 2\left((\boldsymbol{p}_1 - \boldsymbol{p}_k^\text{w})^\mathsf{T}\boldsymbol{n}_k^\text{w}\right)\boldsymbol{n}_k^\text{w}\,. \tag{A.9}$$

Interestingly, if we were to compute the sensitivity of the channel on the physical device position $\boldsymbol{p}_1$ using (A.9), it turns out that the Jacobian involves the Householder matrix from (2.6) which would mirror the uncertainty about the "virtual device" position (in corresponding virtual coordinates) back into global coordinates. In this work, however, we are interested in propagating the position uncertainty of a virtual *mirror device* to the channel-domain using (A.8) which is simply

$$\text{III}: \quad \frac{\partial r_{k,m}^{(i)}}{\partial p_k^{(j)}} = \begin{cases} -1 & i = j \\ 0 & \text{else.} \end{cases} \tag{A.10}$$

We compute the $(3 \times M)$ Jacobian from (A.1) by inserting (A.4), (A.6), and (A.10) and hence compute the sensitivity of the channel elements m on the position $\boldsymbol{p}_k$ as

$$[\boldsymbol{J}_k]_{:,m} = \begin{bmatrix} \frac{\partial r_{k,m}^{(x)}}{\partial p_k^{(x)}} & \frac{\partial d_{k,m}}{\partial r_{k,m}^{(x)}} \\ \frac{\partial r_{k,m}^{(y)}}{\partial p_k^{(y)}} & \frac{\partial d_{k,m}}{\partial r_{k,m}^{(y)}} \\ \frac{\partial r_{k,m}^{(z)}}{\partial p_k^{(z)}} & \frac{\partial d_{k,m}}{\partial r_{k,m}^{(z)}} \end{bmatrix} \frac{\partial [\widetilde{\boldsymbol{h}}_k]_m}{\partial d_{k,m}} \quad \in \mathbb{C}^{1\times 3} \tag{A.11}$$

$$= \left[\underbrace{-1}_{\text{III}} \underbrace{\frac{\boldsymbol{r}_{k,m}}{\|\boldsymbol{r}_{k,m}\|}}_{\text{II}} \right] \underbrace{\frac{\partial [\widetilde{\boldsymbol{h}}_k]_m}{\partial d_{k,m}}}_{\text{I}} \tag{A.12}$$

$$\overset{\text{A}_3}{\approx} \frac{\boldsymbol{r}_{k,m}}{\|\boldsymbol{r}_{k,m}\|} \left(\frac{1}{d_{k,m}} + j \underbrace{\frac{2\pi}{c} f}_{=\frac{2\pi}{\lambda}} \right) [\widetilde{\boldsymbol{h}}_k]_m \,, \tag{A.13}$$

which is used in (2.23) to compute the Jacobian $\boldsymbol{J}_k$ that allows to propagate the uncertainty $\hat{\boldsymbol{C}}_{\boldsymbol{\eta}_\mathsf{p}}^{(k)}$ from the *position domain* to the uncertainty $\hat{\boldsymbol{C}}_\mathsf{p}^{(k)}$ in the *channel domain*.

Appendix B

BiBC

B.1 Proof of Proposition 1

Since $\mathbf{\Psi}\mathbf{\Psi}^H = \alpha_d \mathbf{I}_M$, the following two minimization problems are equivalent:

$$\arg\min_{\mathbf{G}_{AB}} ||\mathbf{Y}_j - \mathbf{G}_{AB}\mathbf{P}_s\mathbf{\Psi}||^2 = \arg\min_{\mathbf{G}_{AB}} ||\mathbf{Y}_{2,j} - \sqrt{\alpha_d}\mathbf{G}_{AB}\mathbf{P}_s||^2. \tag{B.1}$$

To prove that, we first express

$$||\mathbf{Y}_j - \mathbf{G}_{AB}\mathbf{P}_s\mathbf{\Psi}||^2 = ||\mathbf{Y}_j||^2 + ||\mathbf{G}_{AB}\mathbf{P}_s\mathbf{\Psi}||^2 - 2\,\mathrm{Re}\{\mathrm{Tr}\{\mathbf{Y}_j\mathbf{\Psi}^H\mathbf{P}_s\mathbf{G}_{AB}^H\}\}, \tag{B.2a}$$

$$\begin{aligned} ||\mathbf{Y}_{2,j} - \sqrt{\alpha_d}\mathbf{G}_{AB}\mathbf{P}_s||^2 &= ||\mathbf{Y}_j\mathbf{\Psi}^H/\sqrt{\alpha_d} - \sqrt{\alpha_d}\mathbf{G}_{AB}\mathbf{P}_s||^2 \\ &= \frac{||\mathbf{Y}_j\mathbf{\Psi}^H||^2}{\alpha_d} + \alpha_d||\mathbf{G}_{AB}\mathbf{P}_s||^2 - 2\,\mathrm{Re}\{\mathrm{Tr}\{\mathbf{Y}_j\mathbf{\Psi}^H\mathbf{P}_s\mathbf{G}_{AB}^H\}\}. \end{aligned} \tag{B.2b}$$

Therefore,

$$||\mathbf{Y}_j - \mathbf{G}_{AB}\mathbf{P}_s\mathbf{\Psi}||^2 = ||\mathbf{Y}_{2,j} - \sqrt{\alpha_d}\mathbf{G}_{AB}\mathbf{P}_s||^2 + c, \tag{B.3}$$

where $c = ||\mathbf{Y}_j||^2 - ||\mathbf{Y}_j\mathbf{\Psi}^H||^2/\alpha_d$ depends on $\mathbf{Y}_j$ and $\mathbf{\Psi}^H$, but not on $\mathbf{G}_{AB}$, and hence does not effect the minimizer in Eq. (B.1). We can also apply the same calculation to $||\mathbf{Y}_j^p - \mathbf{G}_{BA}\mathbf{\Phi}||^2$ and $||\mathbf{Y}_{1,j} - \sqrt{\alpha_p}\mathbf{G}_{AB}||^2$ since $\mathbf{\Phi}\mathbf{\Phi}^H = \alpha_p\mathbf{I}_N$.

In addition, one can show that the elements of $\mathbf{\Phi}^*(\mathbf{W}_j^p)^T/\sqrt{\alpha_p}$ and $\mathbf{W}_j\mathbf{\Psi}^H/\sqrt{\alpha_d}$ matrices are i.i.d. $\mathcal{CN}(0,1)$. Therefore, the problems in Eqs. (3.19b) and (3.19c) are equivalent.

B.2 Estimation of unknown parameters

When PanB does not know the received signal in P1, the hypothesis test becomes

$$\begin{aligned} \mathcal{H}_0 &: \mathbf{Y}_j = \mathbf{G}_{AB}\mathbf{P}_s\mathbf{\Psi} + \mathbf{W}_j \\ \mathcal{H}_1 &: \mathbf{Y}_j = \mathbf{G}_{AB}\mathbf{P}_s\mathbf{\Psi} + \gamma_j\mathbf{g}_{CB}\mathbf{g}_{AC}^T\mathbf{P}_s\mathbf{\Psi} + \mathbf{W}_j, \end{aligned} \tag{B.4}$$

where $j \in \mathcal{S}_d$.

The GLRT to detect the symbol/presence of the BD is as follows:

$$\frac{\max_{\mathbf{H}_{DL},\mathbf{H}_{BL}} \prod_{j\in\mathcal{S}_d} p\left(\mathbf{Y}_j \mid \mathcal{H}_1, \mathbf{H}_{DL}, \mathbf{H}_{BL}, \gamma_j\right)}{\max_{\mathbf{H}_{DL}} \prod_{j\in\mathcal{S}_d} p\left(\mathbf{Y}_j \mid \mathcal{H}_0, \mathbf{H}_{DL}\right)} \underset{\mathcal{H}_0}{\overset{\mathcal{H}_1}{\gtrless}} \eta, \tag{B.5}$$

where

$$\mathbf{H}_{DL} = \mathbf{G}_{AB}\mathbf{P}_s \tag{B.6}$$

is an $N \times M$ matrix.

Under $\mathcal{H}_0$, $\mathbf{G}_{AB}$ is the unknown parameter, but the estimate of $\mathbf{G}_{AB}$ is not unique because $\mathbf{P}_s$ is not a full-rank matrix. We require, however, only an estimate of $\mathbf{H}_{DL} = \mathbf{G}_{AB}\mathbf{P}_s$, rather than of $\mathbf{G}_{AB}$, to find the maximum of the denominator in Eq. (B.5).

We express the scaled projection matrix as

$$\mathbf{P}_s = \Lambda\mathbf{P} = \Lambda\mathbf{Q}\mathbf{Q}^H. \tag{B.7}$$

To estimate $\mathbf{H}_{DL}$, we first estimate $\mathbf{G}_{AB}\mathbf{Q}$ as follows:

$$\widehat{\mathbf{G}_{AB}\mathbf{Q}} = \arg\max_{\mathbf{G}_{AB}\mathbf{Q}} \prod_{j\in\mathcal{S}_d} p\left(\mathbf{Y}_j \mid \mathcal{H}_0, \mathbf{H}_{DL}\right) \tag{B.8a}$$

$$= \arg\min_{\mathbf{G}_{AB}\mathbf{Q}} \sum_{j\in\mathcal{S}_d} ||\mathbf{Y}_j - \Lambda\mathbf{G}_{AB}\mathbf{Q}\mathbf{Q}^H\Psi||^2 \tag{B.8b}$$

$$= \arg\min_{\mathbf{G}_{AB}\mathbf{Q}} \sum_{j\in\mathcal{S}_d} \left(||\mathbf{Y}_j||^2 + ||\Lambda\mathbf{G}_{AB}\mathbf{Q}\mathbf{Q}^H\Psi||^2 - 2\,\mathrm{Re}\{\mathrm{Tr}\{\Lambda\Psi^H\mathbf{Q}\mathbf{Q}^H\mathbf{G}_{AB}^H\mathbf{Y}_j\}\}\right) \tag{B.8c}$$

$$= \arg\min_{\mathbf{G}_{AB}\mathbf{Q}} \sum_{j\in\mathcal{S}_d} \left(\,\mathrm{Tr}\{\Lambda^2\mathbf{G}_{AB}\mathbf{Q}\mathbf{Q}^H\Psi\Psi^H\mathbf{Q}\mathbf{Q}^H\mathbf{G}_{AB}^H\} - 2\,\mathrm{Re}\{\mathrm{Tr}\{\Lambda\mathbf{Y}_j\Psi^H\mathbf{Q}\mathbf{Q}^H\mathbf{G}_{AB}^H\}\}\right) \tag{B.8d}$$

$$= \arg\min_{\mathbf{G}_{AB}\mathbf{Q}} \sum_{j\in\mathcal{S}_d} \left(\Lambda^2\alpha_d||\mathbf{G}_{AB}\mathbf{Q}||^2 - 2\,\mathrm{Re}\{\mathrm{Tr}\{\Lambda\mathbf{Y}_j\Psi^H\mathbf{Q}\mathbf{Q}^H\mathbf{G}_{AB}^H\}\}\right) \tag{B.8e}$$

$$= \arg\min_{\mathbf{G}_{AB}\mathbf{Q}} \left\{ J_d||\mathbf{G}_{AB}\mathbf{Q}||^2 - 2\sum_{j\in\mathcal{S}_d} \frac{\mathrm{Re}\{\mathrm{Tr}\{\Lambda\mathbf{Y}_j\Psi^H\mathbf{Q}\mathbf{Q}^H\mathbf{G}_{AB}^H\}\}}{\Lambda^2\alpha_d} \right\} \tag{B.8f}$$

$$= \arg\min_{\mathbf{G}_{AB}\mathbf{Q}} \left\| \mathbf{G}_{AB}\mathbf{Q} - \frac{\sum_{j\in\mathcal{S}_d}\mathbf{Y}_j\Psi^H\mathbf{Q}}{J_d\Lambda\alpha_d} \right\|^2 \tag{B.8g}$$

$$= \frac{1}{J_d\Lambda\alpha_d}\sum_{j\in\mathcal{S}_d}\mathbf{Y}_j\Psi^H\mathbf{Q}. \tag{B.8h}$$

We need to estimate $\mathbf{H}_{DL} = \mathbf{G}_{AB}\mathbf{P}_s = \Lambda\mathbf{G}_{AB}\mathbf{Q}\mathbf{Q}^H$ subject to $\mathbf{H}_{DL}^H \in \mathrm{C}(\mathbf{P})$ under $\mathcal{H}_0$. Using Eq. (B.8h), the estimate of $\mathbf{H}_{DL}$ that maximizes the denominator in the GLRT is given by

$$\hat{\mathbf{H}}_{DL}^{\mathcal{H}_0} = \widehat{\mathbf{G}_{AB}\mathbf{P}_s} = \Lambda\widehat{\mathbf{G}_{AB}\mathbf{Q}}\mathbf{Q}^H = \frac{1}{J_d\alpha_d}\sum_{j\in\mathcal{S}_d}\mathbf{Y}_j\Psi^H\mathbf{P}, \tag{B.9}$$

where $(\hat{\mathbf{H}}_{DL}^{\mathcal{H}_0})^H$ lies in $\mathrm{C}(\mathbf{P})$.

The estimate of $\mathbf{H}_{DL}$ under $\mathcal{H}_1$ needs to be calculated similar to Eqs. (B.8) and (B.9) with small modifications. The estimation algorithm for $\mathbf{H}_{BL}$ in Section 3.4.2.2 can be directly used.

Bibliography

[1] B. J. B. Deutschmann, T. Wilding, M. Graber, and K. Witrisal, "XL-MIMO channel modeling and prediction for wireless power transfer," in *WS10 IEEE ICC 2023 Workshop on Near-Field Localization and Communication for 6G*, Rome, Italy, May 2023.

[2] J. F. Esteban, M. Truskaller, L. Fabrete, A. Stanek, D. Delabie, L. V. der Perre, E. G. Larsson, S. Rimalapudi, E. Fitzgerald, F. Tufvesson, O. Edfors, A. Reial, B. Deutschmann, K. Witrisal, T. Wilding, I. Vandeweerd, M. Borrmann, U. Mühlmann, and J. F. Esteban, "Use case-driven specifications and technical requirements and initial channel model," REINDEER project, Deliverable ICT-52-2020 / D1.1, Sep. 2021. DOI: 10.5281/zenodo.5561844.

[3] T. L. Hansen, M. A. Badiu, B. H. Fleury, and B. D. Rao, "A sparse Bayesian learning algorithm with dictionary parameter estimation," in *2014 IEEE 8th Sensor Array and Multichannel Signal Processing Workshop (SAM)*, 2014, pp. 385–388. DOI: 10.1109/SAM.2014.6882422.

[4] REINDEER Project, "Propagation characteristics and channel models for RadioWeaves including reflectarrays," Deliverable ICT-52-2020 / D1.2, 2023 (unpublished).

[5] C. Nelson, X. Li, A. Fedorov, B. Deutschmann, and F. Tufvesson, "Distributed MIMO measurements for integrated communication and sensing in an industrial environment," *Sensors*, vol. 24, no. 5, 2024, ISSN: 1424-8220. DOI: 10.3390/s24051385.

[6] J. Kulmer, F. Wen, N. Garcia, H. Wymeersch, and K. Witrisal, "Impact of Rough Surface Scattering on Stochastic Multipath Component Models," in *2018 IEEE 29th Annual International Symposium on Personal, Indoor and Mobile Radio Communications (PIMRC)*, 2018, pp. 1410–1416. DOI: 10.1109/PIMRC.2018.8580964.

[7] B. J. B. Deutschmann, T. Wilding, E. G. Larsson, and K. Witrisal, "Location-based Initial Access for Wireless Power Transfer with Physically Large Arrays," in *WS08 IEEE ICC 2022 Workshop on Synergies of communication, localization, and sensing towards 6G (WS08 ICC'22 Workshop - ComLS-6G)*, Seoul, Korea (South), May 2022.

[8] A. Richter, "Estimation of Radio Channel Parameters: Models and Algorithms," Ph.D. dissertation, Ilmenau University of Technology, 2005.

[9] Y. Bar-Shalom, X.-R. Li, and T. Kirubarajan, *Estimation with Applications to Tracking and Navigation*. Wiley, Jan. 2002, ISBN: 9780471416555. DOI: 10.1002/0471221279.

[10] S. Kay, *Fundamentals of Statistical Signal Processing: Estimation Theory*. Prentice-Hall PTR, 1993, ISBN: 9788131728994.

[11] R. Project, "Validation of concepts and experimental assessment of key technologies," REINDEER project, Deliverable ICT-52-2020 / D5.3, Dec. 2024.

[12] REINDEER project, "Signal processing for WPT and uplink signalling, exploiting environment awareness," Deliverable ICT-52-2020 / D4.2, unpublished (March 2023).

[13] J. Kulmer, S. Hinteregger, B. Großwindhager, M. Rath, M. S. Bakr, E. Leitinger, and K. Witrisal, "Using DecaWave UWB transceivers for high-accuracy multipath-assisted indoor positioning," in *2017 IEEE International Conference on Communications Workshops (ICC Workshops)*, May 2017, pp. 1239–1245. DOI: 10.1109/ICCW.2017.7962828. (visited on 02/28/2024).

[14] M. Rath, J. Kulmer, M. S. Bakr, B. Großwindhager, and K. Witrisal, "Multipath-assisted indoor positioning enabled by directional UWB sector antennas," in *2017 IEEE 18th International Workshop on Signal Processing Advances in Wireless Communications (SPAWC)*, IEEE, 2017, pp. 1–5. (visited on 02/28/2024).

[15] J. R. Costa, C. R. Medeiros, and C. A. Fernandes, "Performance of a Crossed Exponentially Tapered Slot Antenna for UWB Systems," *IEEE Transactions on Antennas and Propagation*, vol. 57, no. 5, pp. 1345–1352, May 2009, ISSN: 0018-926X. DOI: 10.1109/TAP.2009.2016727.

[16] H. Krim and M. Viberg, "Two Decades of Array Signal Processing Research: The Parametric Approach," *Signal Processing Magazine, IEEE*, vol. 13, pp. 67–94, Aug. 1996. DOI: 10.1109/79.526899.

[17] S. M. Kay, *Fundamentals of Statistical Signal Processing*. Prentice-Hall PTR, 2013, ISBN: 978-0-13-487840-9.
[18] H. Friis, "A Note on a Simple Transmission Formula," *Proceedings of the IRE*, vol. 34, no. 5, pp. 254–256, May 1946, ISSN: 2162-6634. DOI: 10.1109/JRPROC.1946.234568. (visited on 02/08/2024).
[19] H. Lobensommer, *Handbuch der modernen Funktechnik: Prinzipien, Technik, Systeme und praktische Anwendungen ; mit 11 Tabellen*. Franzis, 1995, ISBN: 978-3-7723-4262-2.
[20] C. M. Bishop, *Pattern Recognition and Machine Learning* (Information Science and Statistics). New York: Springer, 2006, ISBN: 978-0-387-31073-2.
[21] G. Wallace, "The JPEG still picture compression standard," *IEEE Transactions on Consumer Electronics*, vol. 38, no. 1, pp. xviii–xxxiv, Feb. 1992, ISSN: 1558-4127. DOI: 10.1109/30.125072. (visited on 02/28/2024).
[22] J. Kimionis, A. Bletsas, and J. N. Sahalos, "Increased range bistatic scatter radio," *IEEE Trans. Commun.*, vol. 62, no. 3, pp. 1091–1104, Mar. 2014.
[23] R. Biswas, M. U. Sheikh, H. Yiğitler, J. Lempiäinen, and R. Jäntti, "Direct path interference suppression requirements for bistatic backscatter communication system," in *Proc. IEEE 93rd Veh. Technol. Conf. (VTC-Spring)*, Apr. 2021.
[24] C. Mollen, J. Choi, E. G. Larsson, and R. W. Heath, "Uplink performance of wideband massive MIMO with one-bit ADCs," *IEEE Trans. Wireless Commun.*, vol. 16, no. 1, pp. 87–100, Oct. 2016.
[25] D. P. Villame and J. S. Marciano, "Carrier suppression locked loop mechanism for UHF RFID readers," in *Proc. IEEE RFID Technol. Appl. Conf. (RFID-TA)*, Apr. 2010, pp. 141–145.
[26] T. Brauner and X. Zhao, "A novel carrier suppression method for RFID," *IEEE Microwave Wireless Comp. Lett.*, vol. 19, no. 3, pp. 128–130, Mar. 2009.
[27] D. Bharadia, K. R. Joshi, M. Kotaru, and S. Katti, "BackFi: High throughput WiFi backscatter," in *Proc. ACM Conf. Special Interest Group Data Commun.*, London, U.K., Aug. 2015, pp. 283–296.
[28] Q. Tao, Y. Li, C. Zhong, S. Shao, and Z. Zhang, "A novel interference cancellation scheme for bistatic backscatter communication systems," *IEEE Commun. Lett.*, vol. 25, no. 6, pp. 2014–2018, Jun. 2021.
[29] R. Duan, E. Menta, H. Yigitler, R. Jantti, and Z. Han, "Hybrid beamformer design for high dynamic range ambient backscatter receivers," in *Proc. IEEE Int. Conf. Commun. Workshops (ICC Workshops)*, May 2019.
[30] H. Guo, Q. Zhang, S. Xiao, and Y.-C. Liang, "Exploiting multiple antennas for cognitive ambient backscatter communication," *IEEE Internet Things J.*, vol. 6, no. 1, pp. 765–775, Feb. 2019.
[31] A. N. Parks, A. Liu, S. Gollakota, and J. R. Smith, "Turbocharging ambient backscatter communication," in *Proc. ACM SIGCOMM*, Chicago, IL, USA, Aug. 2014, pp. 619–630.
[32] V. Iyer, V. Talla, B. Kellogg, S. Gollakota, and J. Smith, "Inter-technology backscatter: Towards internet connectivity for implanted devices," in *Proc. ACM SIGCOMM Conf.*, Florianópolis, Brazil, Aug. 2016, pp. 356–369.
[33] P. Zhang, M. Rostami, P. Hu, and D. Ganesan, "Enabling practical backscatter communication for on-body sensors," in *Proc. ACM SIGCOMM Conf.*, Florianópolis, Brazil, Aug. 2016, pp. 370–383.
[34] M. A. ElMossallamy, M. Pan, R. Jäntti, K. G. Seddik, G. Y. Li, and Z. Han, "Noncoherent backscatter communications over ambient OFDM signals," *IEEE Trans. Commun.*, vol. 67, no. 5, pp. 3597–3611, Feb. 2019.
[35] G. Yang, Y.-C. Liang, R. Zhang, and Y. Pei, "Modulation in the air: Backscatter communication over ambient OFDM carrier," *IEEE Trans. Commun.*, vol. 66, no. 3, pp. 1219–1233, Mar. 2018.
[36] A. Varshney, O. Harms, C. Pérez-Penichet, C. Rohner, F. Hermans, and T. Voigt, "Lorea: A backscatter architecture that achieves a long communication range," in *Proc. ACM Conf. Embedded Netw. Sensor Syst.*, Nov. 2017.
[37] D. Li, "Capacity of backscatter communication with frequency shift in Rician fading channels," *IEEE Wireless Commun. Lett.*, vol. 8, no. 6, pp. 1639–1643, Dec. 2019.
[38] L. Van der Perre, E. G. Larsson, F. Tufvesson, L. De Strycker, E. Björnson, and O. Edfors, "RadioWeaves for efficient connectivity: Analysis and impact of constraints in actual deployments," in *Proc. 53st Asilomar Conf. Signals, Syst., Comput.*, Nov. 2019, pp. 15–22.
[39] H. Q. Ngo, A. Ashikhmin, H. Yang, E. G. Larsson, and T. L. Marzetta, "Cell-free massive MIMO versus small cells," *IEEE Trans. Wireless Commun.*, vol. 16, no. 3, pp. 1834–1850, Jan. 2017.
[40] Z. B. Zawawi, Y. Huang, and B. Clerckx, "Multiuser wirelessly powered backscatter communications: Nonlinearity, waveform design, and SINR-energy tradeoff," *IEEE Trans. Wireless Commun.*, vol. 18, no. 1, pp. 241–253, Nov. 2018.
[41] M. Hua, L. Yang, C. Li, Z. Zhu, and I. Lee, "Bistatic backscatter communication: Shunt network design," *IEEE Internet Things J.*, vol. 8, no. 9, pp. 7691–7705, Nov. 2020.
[42] R. J. Baker, *CMOS: Mixed-Signal Circuit Design*. Hoboken, NJ, USA:Wiley, 2008.
[43] B. Lizon, "Fundamentals of precision ADC noise analysis," Texas Instruments: Dallas, TX, USA, 2020. [Online]. Available: https://www.ti.com/lit/eb/slyy192/slyy192.pdf.

[44] J. Lietzen, A. Liljemark, R. Duan, R. Jäntti, and V. Viikari, "Polarization conversion-based ambient backscatter system," *IEEE Access*, vol. 8, pp. 216 793–216 804, Dec. 2020.

[45] M. Boldi, O. Bulakci, J. Cosmas, M. Ericson, A. Gavras, M. Ghoraishi, and M. Gramaglia, "6G Architecture Landscape – European perspective," 5G Architecture Working Group, 5G PPP, White Paper, Dec. 2022. [Online]. Available: https://5g-ppp.eu/wp-content/uploads/2022/12/6G-Arch-Whitepaper_v1.0-final.pdf.

[46] R. A. Horn and C. R. Johnson, *Matrix Analysis*. Cambridge, U.K.: Cambridge Univ. Press, 2012.

[47] J. Vieira and E. G. Larsson, "Reciprocity calibration of distributed massive MIMO access points for coherent operation," in *Proc. IEEE 32nd Annu. Int. Symp. Pers., Indoor Mobile Radio Commun. (PIMRC)*, Sep. 2021, pp. 783–787.

[48] C. Buyle, B. Cox, D. Delabie, B. Deutschmann, T. Wilding, M. Graber, K. Witrisal, and U. Mühlmann, "System design study for energy-neutral devices interacting with the RadioWeaves infrastructure," REINDEER project, Deliverable ICT-52-2020 / D4.1, Oct. 2022.

[49] L. Zöscher, P. Herkess, J. Grosinger, U. Muehlmann, D. Amschl, and W. Bösch, "Passive differential UHF RFID front-ends in a 40 nm CMOS technology," in *2017 47th European Microwave Conference (EuMC)*, 2017, pp. 105–108. DOI: 10.23919/EuMC.2017.8230810.